List of contents

Word count: 37500

Abstract

The Improvement of Thermal and Mechanical Properties of $La_2Zr_2O_7$-based Pyrochlores as High Temperature Thermal Barrier Coatings

Yanfei Wang

The University of Manchester for the degree of Doctor of Philosophy in the Faculty of Engineering and Physical Sciences

2013

To fully exploit the strengths of $La_2Zr_2O_7$ pyroclores and promote them as a next-generation thermal barrier coating (TBC), the improvements of their thermally insulating property and fracture toughness are studied in this thesis.

A strong phonon scattering source, rattlers, is found in Y^{3+}-doped $La_2Zr_2O_7$ pyrochlores. Rattlers dramatically flatten *k* (thermal conductivity)-T curves, or even make *k* approach the amorphous limit. The presence of rattlers is strongly dependent on (1) oversized atomic cages that are formed in pyrochlores; and (2) the occupation of smaller guest ions in those oversized cages.

To maximize the rattling effect, In^{3+}/Sc^{3+} ions that are much smaller than Y^{3+} are introduced to the $La_2Zr_2O_7$ lattice. As envisaged, the smaller ions in the oversized lattice voids make *k* glass-like at a much lower doping content. Nevertheless, they are still not effective in reducing the high temperature plateau $k_{\min}$. Instead, oxygen vacancies are very effective in reducing $k_{\min}$, because they generate an electrostatic repulsion force among cations surrounding them, resulting in stronger lattice anharmonicity and weaker bonds.

The plateau $k_{\min}$ is reduced dramatically by the filling of the B-sites in $La_2Zr_2O_7$ with a 21% larger (and 50% heavier) Ce^{4+} guest ion rather than a 96% heavier (but similar-sized) Hf^{4+} ion, suggesting that a large absolute size of substitutional atoms is more effective in reducing $k_{\min}$ than a heavy absolute mass. This is because: (1) $k_{\min}$ is proportional to $\sqrt{E/\overline{M}}$ (where E is the elastic modulus and $\overline{M}$ is the average atomic mass); (2) a larger size of guest ions tends to produce a weaker ionic bond and consequently, a lower E; and (3) the changing extent of E by introducing larger guest ions is much greater than that of $\overline{M}$ induced by adding heavier ones.

Lastly, the fracture toughness (K_{Ic}) has been increased by dispersing the tetragonal 3 mol% Y_2O_3-stabilized zirconia (*t*-3YSZ) particulates in the $La_2Zr_2O_7$ (LZ) matrix. The tendency of the dispersive *t*-3YSZ second phases transforming to monoclinic (*m*) phases strongly depends on the volume fraction introduced. For samples made from equilibrium route, they are toughened by phase transformations within the dispersive *t*-3YSZ second phases and a crack shielding effect arising from the residual compressive stress within the LZ matrix. An anticipated increase of K_{Ic} from ferroelastic toughening together with the residual compressive stress toughening highlights a potential to improve coating durability by depositing *t*'-3YSZ/LZ composite TBCs by the non-equilibrium route.

Declaration

No portion of the work referred to in this thesis, "**The improvement of thermal and mechanical properties of $La_2Zr_2O_7$-based pyrochlores as high temperature thermal barrier coatings**", has been submitted in support of an application for another degree or qualification of this or any other university or other institute of learning.

Copyright Statement

(i) The author of this thesis (including any appendices and/or schedules to this thesis) owns certain copyright or related rights in it (the "Copyright") and he has given The University of Manchester certain rights to use such Copyright, including for administrative purposes.

(ii) Copies of this thesis, either in full or in extracts and whether in hard or electronic copy, may be made **only** in accordance with the Copyright, Designs and Patents Act 1988 (as amended) and regulations issued under it or, where appropriate, in accordance with licensing agreements which the University has from time to time. This page must form part of any such copies made.

(iii) The ownership of certain Copyright, patents, designs, trademarks and other intellectual property (the "Intellectual Property") and any reproductions of copyright works in the thesis, for example graphs and tables ("Reproductions"), which may be described in this thesis, may not be owned by the author and may be owned by third parties. Such Intellectual Property and Reproductions cannot and must not be made available for use without the prior written permission of the owner(s) of relevant Intellectual Property and/or Reproductions.

(iv) Further information on the conditions under which disclosure, publication and commercialization of this thesis, the Copyright and any Intellectual Property and/or Reproduction described in it may take place is available in the University IP Policy (See http://www.campus.manchester.ac.uk/medialibrary/poilcies/intellectual-property.pdf), in any relevant Thesis restriction declarations deposited in the University Library, The University Library's regulations (see http://www.manchester.ac.uk/library/aboutus/regulations) and in The University's policy on presentation of Theses.

Acknowledgement

Firstly, I would like to express my sincere gratitude and appreciation to my supervisor Prof. Ping Xiao for his enthusiastic supervision and constant encouragement and inspiration throughout this PhD project. From him, I learned what research is and how to be a good researcher. Also, I would like to thank him for the financial support for the covering of tuition fees during my study.

Secondly, special thanks are going to my senior colleagues Dr. Fan Yang and Dr. Xiaofeng Zhao for their constructive suggestions and discussions. Without their help, this project cannot go as smoothly as it is. They also set me a real model of what a good researcher is. In addition, many thanks are given to the other members in the ceramic coating group for their help and support in this project.

Thirdly, I would like to thank all the technicians in Materials Science Centre for their valuable help in this project, to list a few names: Mr. Andrew Wallwalk (Laser flash); Ms. Judith Shackleton and Mr. Gary Harrison (XRD); Mr. Michael Faulkner (SEM); Mr. Andy Zadoroshnyj (Raman spectroscopy); Mr. Andy Forrest (TG and DSC); Mr. Kenneth Gyves (Optical microscope and micro-indentation), etc. Sincere appreciations are given to all the people both inside and outside this department for the offering of their help to me. Furthermore, I would like to thank China Scholarship Council (CSC) for the provision of my living expense during my study in UK.

Last but not least, I would like to thank my parents, my parents-in-law, my wife (Ms. Yanhong Ma) and my baby son (Siyuan Wang) for their endless support and everlasting love. The baby son, the new arrival of my life, gives me fresh motives of keeping moving forward.

List of figures

Chapter 1

Chapter 2

Chapter 3

Chapter 4

Chapter 5

Chapter 6

List of tables

Chapter 3

Chapter 4

Chapter 5

List of publications

Y. Wang, F. Yang and P. Xiao. *Glass-like thermal conductivities in* $(La_{1-x_1}Y_{x_1})_2(Zr_{1-x_2}Y_{x_2})_2O_{7-x_2}$ *($x = x_1 + x_2$, $0 \leq x \leq 1$) solid solutions*. Acta Mater **60** (2012) 7024-7033.

Y. Wang, F. Yang and P. Xiao. *Rattlers or oxygen vacancies: Determinant of high temperature plateau thermal conductivity in doped pyrochlores*. Appl Phys Lett **102** (2013) 141902 1-5.

Y. Wang, F. Yang and P. Xiao. *Role of substitutional defects on thermal conductivity: A study on* $La_2(Zr_{1-x}B_x)_2O_7$ *(B = Hf, Ce, $0 \leq x \leq 0.5$) pyrochlore solid solutions*. Submitted to Acta Mater, under review.

Y. Wang and P. Xiao. *The phase stability and toughening effect of 3Y-TZP dispersed in the lanthanum zirconate ceramics*. Submitted to J Am Ceram Soc, under review.

Chapter 1 Introduction

1.1 Thermal barrier coating and its material challenges

High-pressure turbine blades and vanes of aero-engines are among those engineering parts which must endure the most extreme and adverse service environment such as a large thermal and mechanical load, a highly oxidative and corrosive hot environment, and a high velocity collision of foreign objects [1]. Over the past five decades, the gas turbine operating temperature has been greatly improved thanks to three principal advances of materials technology [2]: remarkable achievements in alloy design to produce alloy compositions that are more creep and oxidation resistant; dramatic developments in casting technology to manufacture not only the large single-crystal superalloy blades and vanes but also sophisticated internal holes and channels in the blades to facilitate both internal and external cooling; and the deposition of thermal barrier coatings (TBCs) on turbine components. Among all these advances, the use of TBCs in the last two decades has enabled a dramatic increase of gas turbine operating temperature, far greater than that enabled by the switch from cast alloy blades to single crystal blades [2]. While the room for improvements of either the substrate superalloy or the sophisticated cooling technology has been almost fully exploited, a further increase of the gas turbine service temperature should instead depend on the advance of TBCs technology [3].

The primary function of TBCs, as initially envisaged, is to provide a thermally insulating barrier to heat transfer from the hot gas to the metallic components so as to increase the operating temperature, thereby increasing the engine efficiency or extending the life of alloy components [3]. Typically TBCs have a multilayer structure, consisting of a ceramic topcoat, an intermetallic bond coat, a superalloy substrate and a thermally-grown oxide (TGO) layer formed at the topcoat/ bond coat interface due to the oxidation of bond coat. Fig.1.1 shows the schematic illustration of a typical four-layer TBCs system and the requirements of each layer.

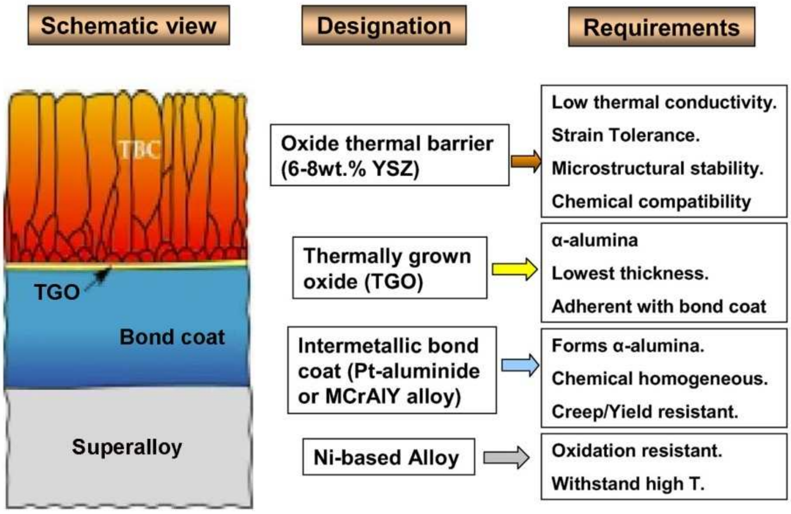

Fig.1.1 The schematic drawing of a four-layer thermal barrier coating system (left) and the material choice and requirements of each layer, after [4,5].

While the advance of the TBC system depends on the collective improvements of individual layers, the relentless demand of raising the service temperature of a gas turbine, which is driven by the economic and environmental motives, is severely challenging the materials employed in the state-of-art TBC system, especially the topcoat material. Since its direct exposure to the extremely hot gases, as a prerequisite, the topcoat ceramic should possess excellent high-temperature stability and an outstanding thermally insulating capacity. The material choice for the topcoats of the state-of-art TBCs is the 6-8 wt. % (3.5-4.5 mol %) yttria-stabilized zirconia (3.5-4.5 YSZ)[*] [2,6]. This composition renders the TBCs the best performance due to a combination of desirable properties, such as a low and temperature-independent thermal conductivity, a high thermal expansion coefficient (TEC) that well matches the underlying metal layer [5], a good thermochemical stability with TGO, and high fracture resistance that is provided by the anti-phase boundaries and twins in the tetragonal-prime (*t*') phase of YSZ TBC fabricated from the high-rate non-equilibrium coating deposition routes [4]. However, the most remarkable drawback of the YSZ topcoat is its phase stability, particularly at elevated temperatures. As a supersaturated phase, the *t*' phase would ultimately transform to a yttria-rich cubic phase and a yttria-lean tetragonal phase, the latter of which inclines to transform to monoclinic phase upon cooling and brings in a catastrophic consequence to TBCs [7]. Therefore, 1473 K is generally regarded as the upper limit of service temperature for a conventional YSZ thermal barrier coating [7-9].

---

[*] If not specified, **xxYSZ** in this thesis represents **xx mol % Y_2O_3 stabilized ZrO_2** where x represents a number

1.2 Lanthanum zirconate: the next-generation topcoat material

To develop the next-generation TBC system which can operate at temperatures well above 1473 K, an alternative high-temperature TBC topcoat material has to be developed. One promising candidate, lanthanum zirconate ($La_2Zr_2O_7$), has attracted a huge attention since its initial proposition by Maloney and coworkers in 2000 [10], attributed to its following superior properties. Firstly, the overriding advantage of $La_2Zr_2O_7$ over its conventional counterpart is its excellent high temperature stability. As the binary phase diagram of La_2O_3-ZrO_2 shown in Fig.1.2, the interphase $La_2Zr_2O_7$ can keep its cubic pyrochlore phase from room temperature until its melting point (around 2573 K). Secondly, the high temperature *k* of $La_2Zr_2O_7$ is about 20% lower than that of YSZ, suggestive of a better insulating capacity at enhanced temperatures, although its *k* is temperature-dependent and is different from that exhibited by the YSZ. Thirdly, $La_2Zr_2O_7$ possesses a combination of good properties, such as the better microstructure stability [9], a lower stiffness [9] and a lower oxygen transparency [11], which correspondingly produces a more sintering resistant, strain compliant and oxygen resistant coating. Last but not least, the cubic pyrochlore, with a generalized form $A_2B_2O_7$, is a network structure of corner linked BO_6 octahedra with the A ions filling the interstices, forming an open-structured crystal lattice with both the A-sites and B-sites substitutable for impurity atoms [12]. The openness of the pyrochlore structure provides the possibility of tailoring its thermophysical properties, such as further reducing thermal conductivity, adjusting the TEC, etc, so as to fully satisfy the requirements set by a TBC system.

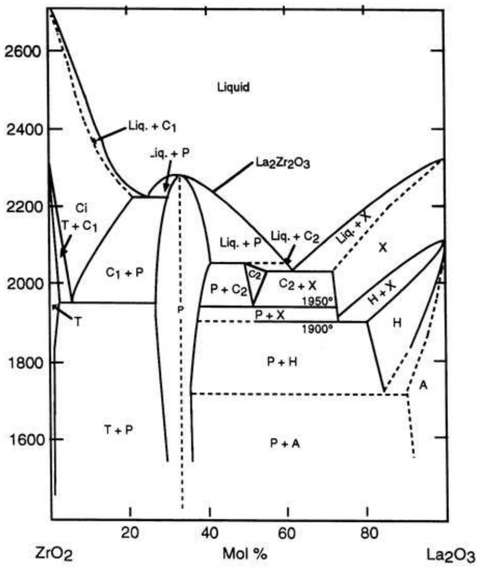

Fig.1.2 ZrO_2-La_2O_3 binary phase diagram [10]

On the other hand, the major disadvantage of $La_2Zr_2O_7$ as a TBC topcoat is its reactivity at high temperatures with the underlying TGO layer to form a porous $LaAlO_3$ interphase [8, 13], which has been solved by inserting a diffusion barrier layer, typically YSZ transition layer, to physically separate these two thermochemically reactive layers [14, 15]. The other deficiency of $La_2Zr_2O_7$ is its poor fracture toughness (about 1.2 $MPa\cdot m^{0.5}$) [16], less than a half of that of YSZ ceramics (about 3 $MPa\cdot m^{0.5}$) [6]. The poor fracture toughness suggests the poor resistance to crack propagation which inevitably results in a poor durability of the corresponding TBCs.

1.3 The goals of this dissertation

The major goal of this dissertation is to develop the next-generation TBC topcoat that can operate at a higher temperature with a longer cyclic life on the basis of $La_2Zr_2O_7$

pyrochlores. To achieve this, we concentrate on the following two aspects: (1) reducing thermal conductivity of $La_2Zr_2O_7$-based ceramics, particularly at high temperatures; and (2) increasing their fracture toughness to improve the durability. The structure of this thesis is organized as follows.

In Chapter 2, the fundamental mechanism of thermal conduction and toughening in ceramics is reviewed, which provides a basic understanding and is helpful to the future discussions of the reducing of thermal conductivity and the toughening of $La_2Zr_2O_7$-based ceramics.

In Chapter 3, an additional strong phonon scattering source, so-called rattlers, is found in yttrium-doped $La_2Zr_2O_7$ pyrochlore solid solutions. Rattlers strongly scatter phonons and make the thermal conductivity (k) - temperature (T) curves rather flat or even glass-like. The presence of rattlers in pyrochlore solid solutions is strongly correlated with (1) the oversized AO_8 atomic cages originated from the specific pyrochlore structure; and (2) the substitution of smaller guest ions for the host ions residing in those cages.

Following the clue to attain the maximized rattling effect as indicated in Chapter 3, Chapter 4 employs much smaller ions, Sc^{3+} and In^{3+}, to occupy the oversized atomic cages, i.e. the A-sites in $A_2B_2O_7$ pyrochlores. As envisaged, the rattling effect becomes more striking, but rattlers appear to be not effective in reducing the high temperature plateau $k_{\min}$. Instead, oxygen vacancies in the lattice seem very effective in reducing $k_{\min}$.

Subsequently, from the study of the B-site doping of $La_2Zr_2O_7$ pyrochlores by Hf^{4+} and Ce^{4+}, in addition to a heavy guest ion as suggested by Winter et al [17], Chapter 5 reveals that the plateau $k_{\min}$ can be markedly reduced by doping a large substitutional atom, because the large impurity atom is prone to reduce the elastic modulus of the ionic crystals (i.e. to soften the lattice).

Chapter 6 seeks the improvement of fracture toughness (K_{Ic}) of $La_2Zr_2O_7$-type ceramics to prolong the life span of $La_2Zr_2O_7$ (LZ) TBCs. The K_{Ic} of $La_2Zr_2O_7$ has been greatly improved by dispersing tetragonal 3 mol % yttria-stabilized zirconia (3YSZ) in the LZ matrix. Although the toughening mechanisms are residual compressive stress toughening and phase transformation toughening for samples made from the equilibrium route in this work, the estimated increase of K_{Ic} from ferroelastic domain switching together with residual compressive stress toughening highlights the great potentials to improve the durability by depositing tetragonal-prime 3YSZ/LZ composite TBCs from the non-equilibrium industrial routes.

Finally in Chapter 7, the main results and conclusions are summarized, along with the inspirations obtained in current studies and the outlook for future research.

References

[1] K.Fritscher, M.Peters, H.J.Ratzer-Scheibe and H.Buhl. *Superalloys and coatings*. In: H. Buhl (Ed.), *Advanced aerospace materials*, Berlin, Springer-Verlag, 1992.

[2] D.R. Clarke DR and C.G. Levi. *Materials design for the next generation thermal barrier coatings*. Annu Rev Mater Res **33** (2003) 383-417.

[3] N.P. Padture, M. Gell and E.H. Jordon. *Thermal barrier coatings for gas-turbine engine applications*. Science **296** (2002) 280-284.

[4] X. Zhao, P. Xiao. *Thermal barrier coatings on nickel superalloy substrates*. Mater Sci Forum **606** (2009) 1-26.

[5] A.G. Evans, D.R. Mumm, J.W. Hutchinson, G.H. Meier and F.S. Pettit. *Mechanisms controlling the durability of thermal barrier coatings*. Prog Mater Sci **46** (2001) 505-553.

[6] A.G. Evans, D.R. Clarke and C.G. Levi. *The influence of oxides on the performance of advanced gas turbines*. J Eur Ceram Soc **28** (2008) 1405-1419.

[7] R.L. Jones and D. Mess. *Improved tetragonal phase stability at 1400 ^oC with scandia, yttria-stabilized zirconia*. Surf Coat Tech **86** (1996) 94-101.

[8] C.G. Levi. *Emerging materials and processes for thermal barrier systems*. Curr Opin Solid St M **8** (2004) 77-91.

[9] R.Vassen, X.Q. Cao, F.Tietz, D.Basu and D.Stover. *Zirconates as new materials for thermal barrier coatings*. J Am Ceram Soc **83** (2000) 2023-2028.

[10] M.J. Maloney. *Thermal barrier coating systems and materials*. US Patent 6117560. United States: United Technologies Corporation, 2000.

[11] X.Q. Cao, R. Vassen, W. Jungen, S. Schwartz, F. Tietz and D. Stover. *Thermal stability of lanthanum zirconate plasma-sprayed coating*. J Am Ceram Soc **84** (2001) 2086-2090.

[12] M.A. Subramanian, G. Aravamudan, G.V.S. Rao. *Oxide pyrochlores - a review*. Prog Solid State Ch **15** (1983) 55-143.

[13] R.M. Leckie, S. Kramer, M. Ruhle and C.G. Levi. *Thermochemical compatibility between alumina and* ZrO_2-$GdO_{3/2}$ *thermal barrier coatings*. Acta Mater **53** (2005) 3281-3292.

[14] R. Vassen, A. Stuke and D. Stover. *Recent developments in the field of thermal barrier coatings*. J Therm Spray Technol **18** (2009) 181-186.

[15] R. Vassen, E. Traeger and D. Stover. *New thermal barrier coatings based on pyrochlore/YSZ double-layer systems*. Int J Appl Ceram Tec **1** (2004) 351-361.

[16] H. Dai, X.H. Zhong, H.Y. Li, Y.F. Zhang, J. Meng and X.Q. Cao. *Thermal stability of double-ceramic-layer thermal barrier coatings with various coating thickness*. Mat Sci Eng A Struct **433** (2006) 1-7.

[17] M.R. Winter and D.R. Clarke. *Thermal conductivity of yttria-stabilized zirconia-hafnia solid solutions*. Acta Mater **54** (2006) 5051-5059.

Chapter 2 Literature review

Part I Thermal conduction mechanisms in ceramics

2.1 Fundamentals of heat conduction in ceramics

The thermal conductivity of a material, k (W/m·K), according to the Fourier's law proposed by Joseph Fourier in 1811, is a measure of heat flux density (q: W/m^2) along a directional temperature gradient (∇T: K/m), as depicted in Eq.(2.1) [1]:

$$q = -k \cdot \nabla T \tag{2.1}$$

While the Fourier's law establishes the foundation for the analysis of thermal conduction, it does not provide a means for the prediction of thermal conductivity. Later, Debye suggested the applicability of the elementary kinetic theory of a dilute gas to dielectric solids by treating lattice vibrations as phonon gases, as shown in Eq.(2.2) [2]:

$$k = \frac{1}{3} C_V \cdot v \cdot \Lambda \tag{2.2}$$

where C_V is the specific heat capacity per unit volume, v is the sound velocity, and Λ is the phonon mean free path. Thus, the thermal conductivity is the product of the amount of energy that can be carried by a particle, the speed at which it moves, and the average distance it travels before scattering. In addition, by considering the frequency-dependence of the above three parameters across the whole phonon spectrum, Eq.(2.2) can be re-written as [3-5]:

$$k = \frac{1}{3}\int_0^{\omega_D} C_V(\omega,T)\cdot v(\omega)\cdot \Lambda(\omega,T)d\omega \tag{2.3}$$

in which ω_D is the Debye frequency, and $C_V(\omega)d\omega$ is the contribution to specific heat of vibration modes in the frequency interval $d\omega$ about ω.

To influence thermal conductivity, according to Eq.(2.3), various mechanisms are employed to change the prior three parameters, among which the phonon mean free path Λ is the most widely-used one. In a polycrystalline ceramic material, the phonon mean free path usually includes the contributions from phonon-phonon scattering, phonon-point defects scattering, phonon-grain boundary scattering [5], and the phonon-rattler interaction (also known as resonant phonon scattering) that was recently found in thermoelectric materials [6-8]. Although the presence of rattlers is strongly dependent on the a specific crystalline structure such as oversized atomic cages, the rattlers can scatter phonons so strongly to induce a glass-like thermal conductivity, thereby attracting a huge research interest [6-7]. In the subsequent parts, these four phonon scattering mechanisms are to be generally reviewed.

2.1.1 Phonon-phonon Umklapp scattering

Since its dominance over the intrinsic thermal conductivity of a ceramic material, the phonon-phonon Umklapp scattering is the most significant mechanism. When the temperature exceeds the Debye temperature Θ_D, the specific heat capacity per unit volume $C_V(\omega,T)$ in Eq.(2.3) is independent of T and has the following form:[3]

$$C_V(\omega,T) = B\cdot\omega^2 \tag{2.4}$$

in which B is a constant. The phonon mean free path due to phonon-phonon Umklapp scattering Λ_U is temperature dependent and can be described as:[9]

$$\Lambda_U(\omega,T) = \frac{D_U}{\omega^2 T} \tag{2.5}$$

where D_U is a constant independent of temperature and frequency, having the following expression:[10,11]

$$D_U = \frac{\sqrt{2}}{4\pi}\left(\frac{v^2}{a}\right)\left(\frac{\overline{M}v^2}{\gamma^2 k_B}\right) \tag{2.6}$$

in which a^3 and $\overline{M}$ are the average atomic volume and mass respectively, γ is the Grüneisen parameter, and k_B is the Boltzmann constant.

By combining Eqs.(2.3-2.6) and employing $B = 9k_B/(a^3\cdot\omega_D^3)$ [3] and $v = a\omega_D(6\pi^2)^{-1/3}$ [2], we can obtain the intrinsic thermal conductivity of a ceramic material as follows:

$$k_U^0 = \frac{BvD_U\omega_D}{3T} = \frac{\overline{M}v^3}{45a^2\gamma^2}\cdot\frac{1}{T} = \frac{A}{T} \tag{2.7}$$

Eq.(2.5) suggests phonon mean free path Λ decreases indefinitely with increasing temperature. However, Λ can not be smaller than the inter-atomic spacing [12]. Therefore, there is a minimum phonon mean free path $\Lambda_{\min}$ such that:

$$\Lambda_U(\omega,T) = \frac{D_U}{\omega^2 T} \quad \text{if} \quad \frac{D_U}{\omega^2 T} > \Lambda_{\min}, \tag{2.8a}$$

$$\Lambda_U(\omega,T) = \Lambda_{\min} \text{ if } \frac{D_U}{\omega^2 T} < \Lambda_{\min}. \qquad (2.8b)$$

The integration of Eq.(2.3) with $\Lambda_U(\omega,T)$ expression from Eq.(2.8) yields:

$$k_U = \frac{1}{3}\left(\int_0^{\omega'} B\omega^2 v \frac{D_U}{\omega^2 T} d\omega + \int_{\omega'}^{\omega_D} B\omega^2 v \Lambda_{\min} d\omega\right) = \frac{2}{3} A \frac{\sqrt{T_1}}{T^{1.5}} + \frac{A}{3T_1} \qquad (2.9)$$

where $\omega' = \sqrt{\frac{D_U}{\Lambda_{\min} T}} = \sqrt{\frac{T_1}{T}}\omega_D$, and $T_1 = \frac{D_U}{\Lambda_{\min}\omega_D^2}$. By substituting of the expression for D_U (Eq.(2.6)) and the relationship $v = a\omega_D(6\pi^2)^{-1/3}$ [2], the characteristic temperature T_1, below which the phonon mean free path never reaches its minimal value, can be expressed as:

$$T_1 = 0.0074 \frac{\overline{M} v a^2}{k_B \Lambda_{\min} \gamma^2} \qquad (2.10).$$

Eq.(2.9) suggests that, in reality, the thermal conductivity k can decrease neither indefinitely with increasing T nor as steeply as Eq.(2.7) predicts (i.e. the famous $k \sim \frac{1}{T}$ law). Instead, the thermal conductivity k is prone to decrease less steeply and reach a plateau $\frac{A}{3T_1}$ above a certain temperature. By combining the expressions of A (Eq.(2.7)) and T_1 (Eq.(2.10)), the plateau thermal conductivity ($k_{\min}$) has the following form:

$$\frac{A}{3T_1} = \frac{1}{3}\frac{3k_B}{a^3} \cdot v \cdot \Lambda_{\min} \qquad (2.11),$$

in which ($3k_B/a^3$) is the asymptotic value of the heat capacity at high temperatures per atom. Obviously, the high temperature plateau $k_{\min}$ (Eq.(2.11)) conforms to the general expression of k (Eq.(2.2)), in which C_V and Λ approaches their respective asymptotic values ($3k_B/a^3$ for the former and inter-atomic spacing $\Lambda_{\min}$ for the latter [12]), thereby yielding an almost constant plateau $k_{\min}$. Regarding the similar value of a and $\Lambda_{\min}$, the plateau $k_{\min}$ is of the order of $k_B \cdot v/a^2$, which is consistent with the conclusion reached by G. Grimvall [13].

2.1.2 Phonon-point defects scattering

Point defects (substitutional atoms, vacancies, and interstitials) are very common in a lattice. Point defects can interact with the phonons and thus contribute to a thermal resistance. To account for this contribution, a phonon mean free path due to point defects Λ_P is introduced, as shown in Eq.(2.12):

$$\frac{1}{\Lambda_{U+P}(\omega,T)} = \frac{1}{\Lambda_U(\omega,T)} + \frac{1}{\Lambda_P(\omega)} \tag{2.12}$$

According to [9], Λ_P is inversely proportional to point defect concentration c_P but independent of temperature, as described by Eq.(2.13):

$$\Lambda_P(\omega) = \frac{D_P}{c_P \omega^4} \tag{2.13}$$

where D_P is a constant and has an expression of: [14]

$$D_P = \frac{4\pi v^4}{\Gamma \Omega_0} \tag{2.14}$$

in which Γ is the scattering coefficient of point defects and Ω_0 is the volume of unit cell.

If neglecting the premise that the phonon mean free path cannot be smaller than the inter-atomic spacing, the thermal conductivity of a ceramic material with point defects can be expressed as:

$$k_{U+P}^{0}=\frac{1}{3}\int_{0}^{\omega_D} B\omega^2 v\left(\frac{1}{\frac{c_P\omega^4}{D_P}+\frac{\omega^2 T}{D_U}}\right)d\omega=\frac{1}{3}Bv\sqrt{\frac{D_U D_P}{Tc_P}}\arctan\left(\omega_D\sqrt{\frac{D_U c_P}{TD_P}}\right) \tag{2.15}$$

Obviously, the minimum phonon mean free path $\Lambda_{\min}$ is still applicable to a lattice with point defects. Accordingly, Λ has the following various values:

$$\frac{1}{\Lambda_{U+P}}=\frac{c_P\omega^4}{D_P}+\frac{\omega^2 T}{D_U}\quad \text{if}\quad \frac{1}{\Lambda_{\min}}>\frac{c_P\omega^4}{D_P}+\frac{\omega^2 T}{D_U}, \tag{2.16a}$$

$$\frac{1}{\Lambda_{U+P}}=\frac{1}{\Lambda_{\min}}\ \text{if}\quad \frac{1}{\Lambda_{\min}}<\frac{c_P\omega^4}{D_P}+\frac{\omega^2 T}{D_U}. \tag{2.16b}$$

After substituting Eq.(2.16) for the Λ in Eq.(2.3), the integration then becomes:

$$\begin{aligned}k_{U+P}&=\frac{1}{3}\left(\int_{0}^{\omega_1} B\omega^2 v\frac{1}{\frac{c_P\omega^4}{D_P}+\frac{\omega^2 T}{D_U}}d\omega+\int_{\omega_1}^{\omega_D} B\omega^2 v\Lambda_{\min}d\omega\right), \\ &=\frac{A}{T}\frac{\omega_0}{\omega_D}\arctan\left(\frac{\omega_1}{\omega_0}\right)+\frac{A}{3T}\frac{1}{1+\left(\frac{\omega_1}{\omega_0}\right)^2}\left[\left(\frac{\omega_D}{\omega_1}\right)^2-\frac{\omega_1}{\omega_D}\right]\end{aligned} \tag{2.17a}$$

in which $\omega_0=\sqrt{\frac{D_P T}{D_U c_P}}$, deduced from Λ_U (ω_0) = Λ_P (ω_0); and

$\omega_1=\omega_0\sqrt{-\frac{1}{2}+\sqrt{\frac{1}{4}+\left(\frac{\omega'}{\omega_0}\right)^2}}$. The frequency ω_1 is defined as $\Lambda_{U+P}(\omega_1)=\Lambda_{\min}$.

By incorporating expressions of ω_0, ω_1, and ω' ($\omega' = \sqrt{\frac{D_U}{\Lambda_{\min} T}}$, Eq.(2.9)), the Eq.(2.17a) can be re-written with only three variables (A, T_1 and α) as:

$$k_{U+P} = \frac{A}{3T_1} + \frac{A}{T^{0.5}}\frac{2}{\sqrt{\alpha}}\arctan\sqrt{-\frac{1}{2}+\frac{1}{2}\sqrt{1+\alpha\frac{T_1}{T^2}}} - \frac{2\sqrt{2}}{3}\frac{A\sqrt{T_1}}{T^{1.5}}\frac{1}{(1+\sqrt{1+\alpha\frac{T_1}{T^2}})^{1.5}} \quad (2.17b),$$

$$\text{in which } \alpha = \frac{4c_P\omega_D^2 D_U}{D_P} = \frac{\sqrt{2}}{4\pi^2}\frac{c_P\Omega_0\overline{M}\omega_D^2\Gamma}{k_B a\gamma^2} = 0.544\frac{c_P N\overline{M}v^2\Gamma}{k_B\gamma^2} \quad (2.17c).$$

In the above expressions, c_P is the point defect concentration, which is defined as the ratio of the total number of point defects to total number of atomic sites; Γ is the scattering coefficient of point defects, reflecting the strength of phonon-point defect interaction; and N is the number of atoms per unit cell ($\Omega_0 = N \cdot a^3$).

2.1.3 Phonon-grain boundary scattering

The grain boundary is another extrinsic phonon scattering mechanism. In contrary to point defects, which favourably scatter high-frequency phonons [3], grain boundaries tend to scatter low-frequency phonons [5]. The attenuation length of phonons due to grain boundaries (Λ_{GB}) is independent of phonon frequency and temperature and relies on a characteristic length (L) of grains in dielectric materials: [3,15]

$$\Lambda_{GB} = L \quad (2.18)$$

Therefore, in a polycrystalline dielectric material without any point defects, the Umklapp phonon-phonon scattering and phonon-grain boundary scattering contribute to the thermal resistance, and the attenuation length of phonons has the following form:

$$\frac{1}{\Lambda_{U+GB}(\omega,T)}=\frac{1}{\Lambda_U(\omega,T)}+\frac{1}{\Lambda_{GB}(\omega)}=\frac{\omega^2 T}{D_U}+\frac{1}{L} \tag{2.19}$$

Thus, integration of Eq.(2.3) gives:

$$\begin{aligned} k^0_{U+GB} &= \frac{1}{3}\int_0^{\omega_D} B\omega^2 v\left(\frac{1}{\frac{1}{L}+\frac{\omega^2 T}{D_U}}\right)d\omega \\ &= \frac{BvD_U\omega_D}{3T}\left(1-\frac{\omega_B}{\omega_D}\arctan\frac{\omega_D}{\omega_B}\right)=k^0_U\left(1-\frac{\omega_B}{\omega_D}\arctan\frac{\omega_D}{\omega_B}\right) \end{aligned}\quad , \tag{2.20}$$

and the thermal conductivity reduction corresponding to grain boundary scattering (Δk_{GB}) can then be expressed as:

$$\Delta k_{GB}=k^0_U\frac{\omega_B}{\omega_D}\arctan\frac{\omega_D}{\omega_B}\ . \tag{2.21}$$

In the above expressions, ω_B is the frequency at which $\Lambda_U(\omega_B) = L$. From Eq.(2.5), $\omega_B=\sqrt{\frac{D_U}{LT}}$.

According to Eq.(2.21), the contribution from grain boundary scattering is significant provided dielectric polycrystalline materials have a low characteristic length *L*, which, in reality, can be treated as the average grain size. To be specific, the grain boundary scattering is effective only when the grain size is comparable or even smaller than the phonon mean free path. In addition, this mechanism is more evident at lower temperatures (far lower than the Debye temperature Θ_D) [5].

2.1.4 The resonant phonon scattering

In comparison with the prior three universal mechanisms, the resonant phonon scattering is less common and emerges under a certain circumstance. The first scenario relates to the substitution of radicals, such as NO_2^- [16] and CN^- [17], in the ionic crystals [18]. Apart from the collective motions of the comparatively stiff framework, the localized excitations due to translation and/or rotation of guest radicals exist at very low frequency [18]. The second scenario stems from a specific crystalline structure, which usually possesses oversized atomic cages, such as Si/Ge clathrates [19,20], filled skutterudites [6,7], as shown in Fig.2.1 [21]. Entrapped in these voids, a guest atom, so-called ‘rattler’, weakly bound to the cages, tends to oscillate locally and incoherently with a large excursion, which can strongly scatter the propagating phonons [21].

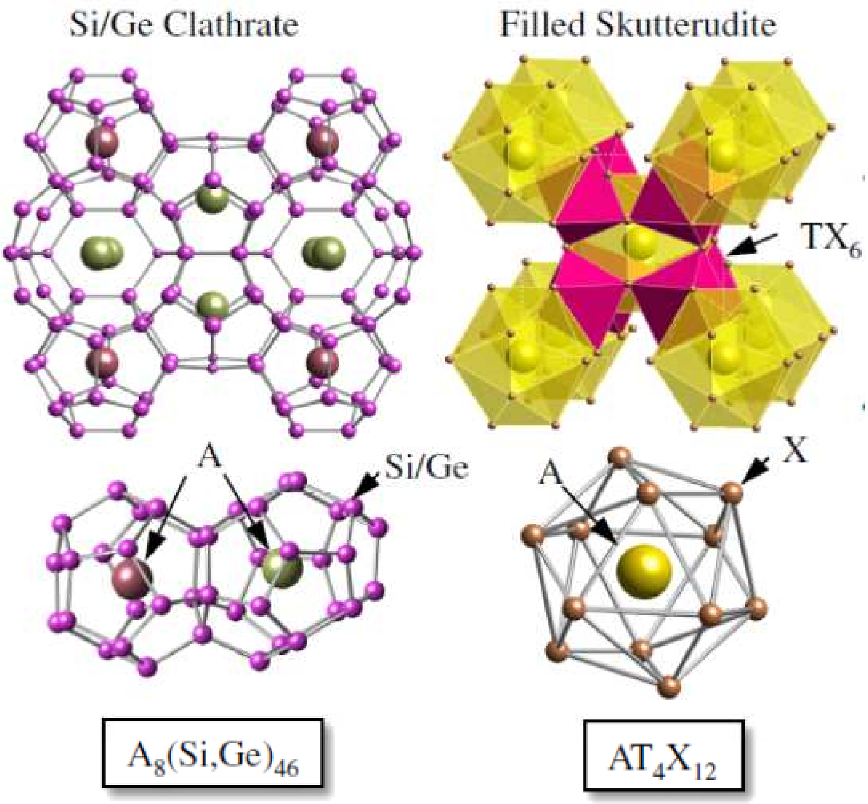

Fig.2.1 Crystal structures of typical cage compounds: Si/Ge clathrates and filled skutterudites, after Ref. [21]. An atomic cage containing an A atom at the centre is shown below.

There are two approaches to explain the dramatic suppressive effects of rattlers on heat conduction in the literature. On the one hand, researchers attribute the anomalously low thermal conductivity manifested by those crystals with oversized atomic cages to the resonant scattering of the low-frequency acoustic phonons by the localized and incoherent vibrations of rattlers in the cages [6,7,22,23]. In this prospective, to reduce thermal conductivity, rattlers predominantly decrease phonon mean free path Λ rather than specific heat capacitance C_V or phonon group velocity v in Eq.(2.2). Accordingly, the phonon mean free path Λ of a crystal with rattlers present can be expressed as:[22,24]

$$\frac{1}{\Lambda}=\frac{1}{\Lambda_U}+\frac{1}{\Lambda_{rattler}}=\frac{\omega^2 T}{D_U}+\sum_i \frac{C_i\omega^2}{(\omega_{Ri}^2-\omega^2)^2} \tag{2.22}$$

in which $\Lambda_{rattler}$ is the additional phonon attenuation length ascribed to the presence of rattlers; ω_{Ri} is the characteristic resonant frequency of rattlers; and C_i is a temperature-independent constant. The summation over i for $\frac{1}{\Lambda_{rattler}}$ in Eq.(2.22) stems from the usual multiple resonant frequencies that are present from the vibration of rattlers. In this consideration, rattlers mainly affect phonon mean free path and they are therefore only effective in reducing thermal conductivity within the intermediate and low temperature range, because rattlers are not effective in reducing the asymptotic value of Λ (i.e. $\Lambda_{\min}$, inter-atomic spacing) or the phonon group velocity v, both of which, according to Eq.(2.11), are the parameters determining the high temperature plateau $k_{\min}$.

While the transport models associated with resonant scattering have tended to assume a constant group velocity, which does not fully capture the details of the rattling interaction, the phonon group velocity is much lower than the speed of sound in the frequency regime near the avoided crossing [25,26], as schematically illustrated in Fig.2.2. We can approximate an empty framework as a monatomic chain of atoms with mass m_1 connected with springs k_1 (black curve, Fig.2.2 (a)). To simulate the inclusion of guest atoms, we include a second atom with mass m_2, coupled to the framework via springs k_2. When $k_2 >> k_1$, the material behaves as a simple two-atom solid. Decreasing the value of k_2 leads to the emergence of rattling behaviour, causing the frequency of the associated optical mode to drop into the acoustic frequency range. In the phonon dispersion, this interaction is seen as the avoided crossing between the optical and acoustic branches.[25] The strength of this interaction, or the extent of the avoided crossing, increases as k_2 stiffens. As depicted in Fig.2.2 (b), the avoided crossing has enabled a greatly reduced the group velocity and the consequent lower thermal conductivity, according to the following expression:

$$k = \frac{1}{3} C_V v^2 \tau \tag{2.23}$$

in which τ is phonon relaxation time and is related to phonon mean free path Λ through phonon velocity ($\tau = \Lambda / v$). In addition, unlike the framework atoms, which are harmonic oscillators and connected to each other by a “spring”, rattlers are instead loosely bound in the cages and vibrate with large amplitude, and therefore are suggested to be able to strengthen the lattice anharmonicity [21]. It is worth noting that, both the reduction of phonon velocity and the enhancement of lattice anharmonicity facilitate the suppression of k not only at low and intermediate temperatures but also at high temperatures, which is in a clear distinction with the prior discussion that only considers the effect of rattlers on phonon mean free path Λ.

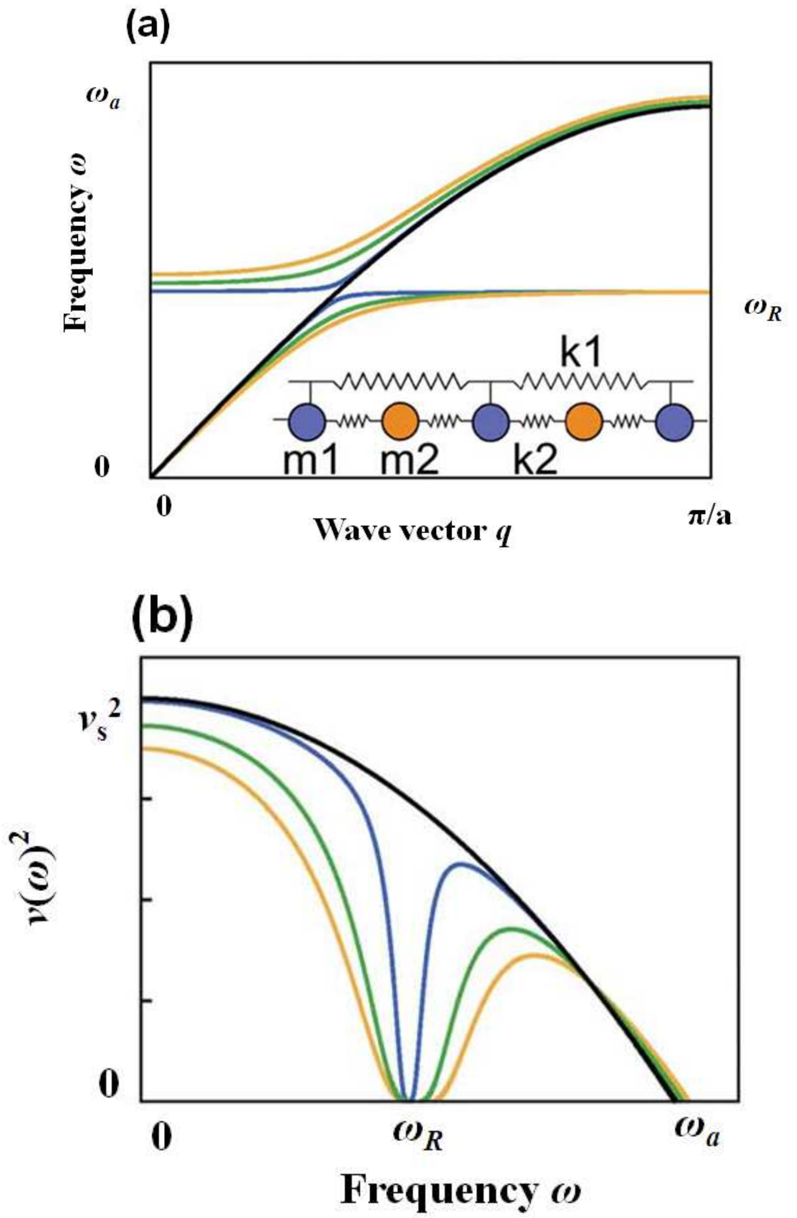

Fig.2.2 (a) the phonon dispersion curves of cage compounds with (colour curves) and without (black curves) guest species and (b) the effect of guest species on the square of the spectral phonon group velocity. The avoided crossing caused by rattlers flattens the phonon dispersion curves in (a) and results in a dramatic drop of v^2 close to resonant frequency ω_R in (b). The frequency of rattler mode ω_R is proportional to $\sqrt{k_2 / m_2}$, and the mode mixing increases with a stiffening k_2. After [25].

2.2 Strategies of reducing thermal conductivity in ceramics

According to the principal origins of thermal resistance from various phonon scattering processes as summarized in 2.1, the corresponding strategies can then be employed accordingly in order to achieve the superiorly insulating ceramics with the lowest possible thermal conductivity. Among the various phonon scattering processes discussed, the phonon-phonon Umklapp scattering is of the top significance, because it determines not only the intrinsic thermal conductivity of a material, but also its high temperature plateau thermal conductivity k_{min}, which is extremely important to components operating under high temperatures such as for thermal barrier coatings (TBCs). On the basis of intrinsic thermal conductivity, the point defects, grain boundaries and rattlers (whose presence is strongly dependent on the crystalline structures), are then introduced to further suppress thermal conductivity.

2.2.1 Reduce the intrinsic thermal conductivity

To search a material with intrinsically low thermal conductivity, we should focus on two aspects: one is the anharmonicity of the bonding, depicted by the Grüneisen parameter (γ), upon which the phonon-phonon Umklapp scattering is strongly dependent; and the other one is the phonon group velocity v. A larger γ together with a smaller v will give a smaller intrinsic thermal conductivity as well as a smaller plateau k_{min}.

On the enhancement of lattice anharmonicity, there are a few reports in the literature. Firstly, Morelli and co-workers [27, 28] and Nielsen and co-workers [29] reported the role of lone pair electrons on the improvement of the lattice anharmonicity in cubic I-V-VI_2 semiconductors such as $AgSbTe_2$, $AgBiTe_2$, $CuSbSe_2$, etc. Ref.[27] finds that, thermal conductivity of I-V-VI_2 ($AgSbTe_2$, $AgBiSe_2$) semiconductors exhibits glass-like behaviour, whereas that of I-III-VI_2 ($AgInTe_2$) semiconductors is apparently not glass-like. The difference might stem from nonbonding lone pair electrons in Sb or Bi (the VA group element), which are expected to form a shell of relatively large radius. During thermal vibrations atoms approach one another, leading to the overlapping of lone pair electron waves and hence the creation of a repulsive force, or an anharmonicity in the force. Secondly, Delaire et al [30] reported a giant anharmonic phonon scattering in PbTe from the strong anharmonic coupling between the ferroelectric transverse optic (TO) mode and the longitudinal acoustic (LA) modes. Their measurements reveal a strong, unprecedented coupling between TO and LA phonon branches, resulting in an avoided-crossing behaviour with a softening and damping of the LA branch and a repulsion of the TO branch. Thirdly, as already mentioned in the prior context, the introduction of rattlers to the lattice is believed to cause the increase of lattice anharmonicity.

To reduce the phonon group velocity v, there are two different methods. Firstly, the lattice that has a very weak and non-directional bonding is prone to have a low intrinsic thermal conductivity. The ideal crystals are those which have a very soft bonding for the purpose of heat conduction, while at the same time not being unduly soft from the perspective of stiffness or melting [30]. Secondly, in comparison with the direct softening of lattice, it is instead to keep the vast majority of heat trapped in flat, low velocity optical modes by introducing complex primitive cells or constituent atoms with a high mass contrast [25].

2.2.2 Improve phonon scattering by grain boundaries

To exploit grain boundaries as an extrinsic phonon scattering source so as to achieve superiorly low thermal conductivity, some researchers attempted to introduce as many as possible grain boundaries in the yttria-stabilized zirconia (i.e. fabricating YSZ nano-crystallines) and study their possible effects on heat transport. The results suggest that, the reduction effect of thermal conductivity from grain boundaries becomes significant only when the grain size becomes adequately small.

Raghavan and co-workers pointed out that, a variation of grain sizes from 400 nm down to 70 nm for the 3.2 YSZ was not significant enough to cause any thermal conductivity difference [31]. Similarly, Limarga and Clarke [32] observed thermal conductivity (*k*) - temperature (*T*) curves of tetragonal 3YSZ polycrystalline bulk samples (Fig.2.3), which are overlapping but still distinguishable especially at relatively low temperatures, suggesting a rather weak grain boundary effect. The weak dependence of thermal conductivity on grain sizes suggests that the grains sizes are well above the critical values in these two studies.

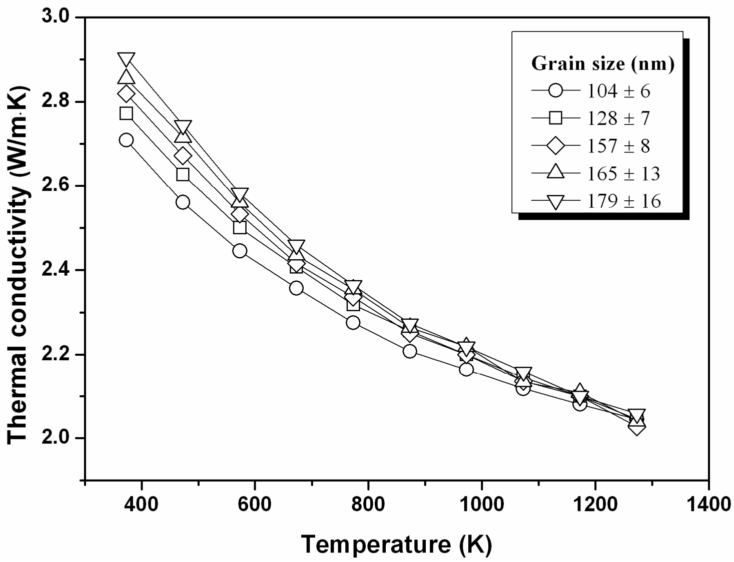

Fig.2.3 The measured thermal conductivity of 3 mol% yttria-stabilized zirconia (3YSZ) bulk samples with grain sizes ranging from 104 nm to 179 nm, re-plotted after [32].

By contrast, Soyez and co-workers [33] found a strong dependence of thermal conductivity on the grain size of YSZ thin films, as shown in Fig.2.4. The thermal conductivity of the YSZ thin films drops dramatically when the grain sizes are smaller than 15 nm. Another study by Yang and co-workers [34] reported a strong grain-size dependent thermal conductivity of nanocrystalline 8-15 YSZ thin films from 6-480 K, as shown in Fig.2.5. The thermal conductivity for a grain size of 10 nm is reduced to approximately half that of coarse-grained or single crystal materials. In addition, Dura and co-workers [35] found a clear decreasing trend of the thermal conductivity for 10YSZ pellets with grain sizes decreasing from 1000 nm down to 17 nm, as shown in Fig.2.6. Therefore, all these different observations suggest that the critical grain size for YSZ is about 15 nm.

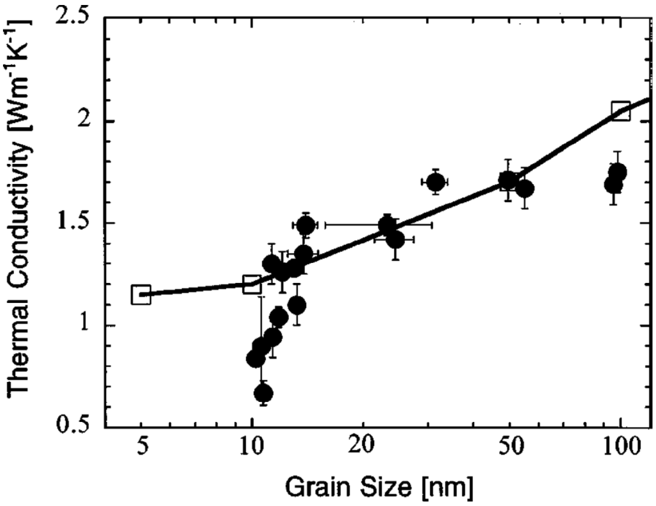

Fig.2.4 The measured thermal conductivity values of YSZ thin films as a function of grain size (closed circles) at room temperature. The predicted behaviour calculated by Klemens and Gell (open squares) [5] for 4YSZ is also included for comparison. After [33].

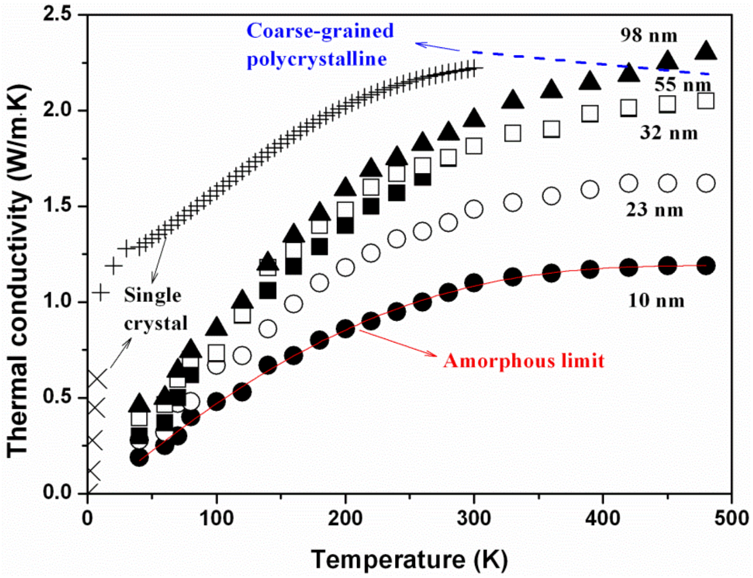

Fig.2.5 The measured thermal conductivity of nanocrystalline 8-15 YSZ with cubic phases from 6 - 480 K for several grain sizes, after [34]. Data are compared with literature values for single-crystal (×: data from [36]; +: data from [37]) and coarse-grained polycrystalline (dashed line: data from [38]) cubic YSZ. The amorphous limit of thermal conductivity (solid line, from [37]) for YSZ is also included.

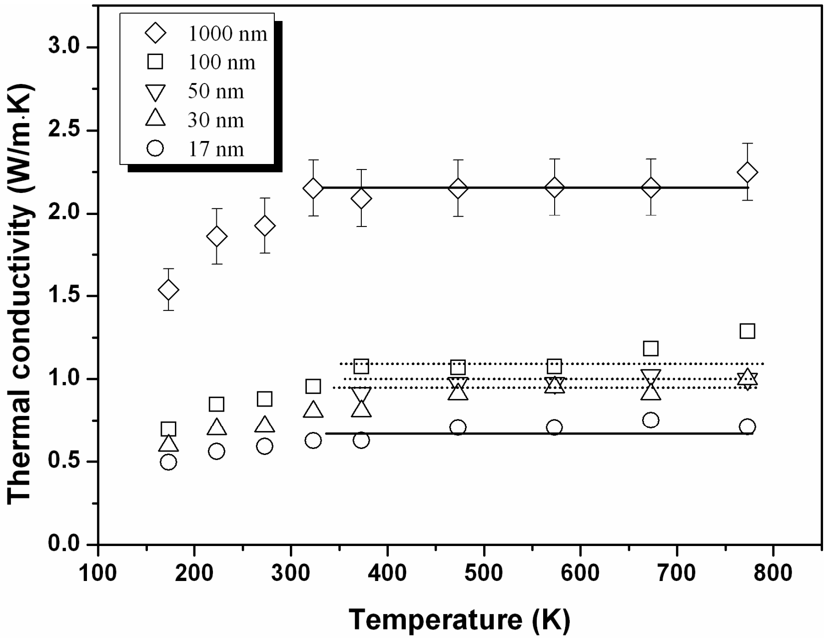

Fig.2.6 The measured thermal conductivity of 10 mol% yttria-stabilized zirconia (10YSZ) with grain sizes ranging from 17 nm to 1000 nm, re-plotted after [35].

On the critical grain size, it is generally believed that it should be smaller than, at least comparable with the phonon mean free path Λ of the corresponding material. Debye derived the following relationship to describe the temperature dependence of Λ:[33]

$$\Lambda = \frac{20T_m d}{\gamma^2 T} \tag{2.24}$$,

in which T_m is the melting temperature (in K); d is the lattice parameter; and γ is the Grüneisen parameter. Accordingly, the phonon mean free path Λ for single crystal YSZ is about 25 nm at 300 K [33]. In addition, according to Eq.(2.24), Λ is inversely proportional to T and hence, Λ decreases rapidly with an increase of temperature, for example, the Λ for YSZ is only several nanometres at 1500 K [33]. This undoubtedly raises the difficulty of exploiting grain boundaries as a phonon scattering source for TBC applications, because it requires ultrafine nano-crystalline grains of YSZ, ideally with several nanometres. Practically, it is not easy to produce such extremely small grains of TBC. Even if they are successfully manufactured, the nano-crystalline grains are unstable and susceptible to collapse when exposed to the elevated temperature during service.

Furthermore, the low-*k* materials usually have a small phonon mean free path and thus require an ultrafine nano-crystalline grain to induce a considerable grain boundary scattering. For $La_2Zr_2O_7$ ceramics, according to Eq.(2.24), the phonon mean free path at 300 K and 1500 K is about 41 nm and 8 nm respectively, which is at the similar level as that of YSZ. Therefore, for TBC materials with low thermal conductivity, it seems not feasible to exploit grain boundaries as an extrinsic phonon scattering source.

2.2.3 Improve phonon scattering by the point defects

The point defects, also known as the static structural imperfection, are another conventionally employed strategy to further reduce the thermal conductivity of a material. They mainly include the following three different forms: vacancies, interstitials and substitutional atoms. With reference to the ideal lattice, a point defect results in (1) mass fluctuation; (2) the local bonding strength difference (hence the elastic modulus variation); and (3) a compressive or tensile strain field. As depicted by Eq.(2.25), the above three aspects are all contributing to the scattering coefficient Γ, a parameter reflecting the strength of point defect-phonon scattering [14,39]:

$$\Gamma = \sum_i \Gamma_i = \sum_i x_i[(\frac{\Delta M_i}{M})^2 + 2(\frac{\Delta G_i}{G} - 6.4 \times \gamma \frac{\Delta \delta_i}{\delta})^2] \qquad (2.25)$$

in which x_i is the fraction of impurity atoms with mass M_i and size δ_i; G_i is the average stiffness of the nearest bond from the impurity atom to its neighbouring host atom while G is the corresponding value for the host lattice; $M = \sum_i x_i M_i$; $\delta = \sum_i x_i \delta_i^{'}$; $\Delta M_i = M_i - M$; $\Delta\delta_i = \delta_i - \delta$; and is $\delta_i^{'}$ the impurity radius in its own lattice.

Taken into the consideration of the ionic change when an impurity atom enters a different lattice [40] and bonding stiffness term ΔG_i/G being $-2\gamma\sqrt{6}(\Delta\delta_i / \delta)$ [14], we can obtain:

$$\Gamma_i = x_i[(\frac{\Delta M_i}{M})^2 + \varepsilon(\frac{\Delta\delta_i}{\delta})^2] \qquad (2.26),$$

in which ε is a constant, relating to the Grüneisen parameter γ and the Poisson's ratio ν, and has the following expression:

$$\varepsilon = 2(\frac{2\gamma}{\sqrt{6}} + \frac{6.4}{3}\gamma\frac{1+\nu}{1-\nu})^2 \qquad (2.27).$$

2.2.3.1 Oxygen vacancies

The oxygen vacancy is one of the most powerful phonon scattering sources, which can be reflected by a large scattering coefficient Γ due to the complete loss of the mass, the linkages in conjunction with an intensive elastic field caused by the maximized size mismatch between the host ion and the vacancy. The yttria-stabilized zirconia (YSZ) is a typical example of employing oxygen vacancies as a major phonon scattering source.

The trivalent Y^{3+} ions, substituting for the tetravalent Zr^{4+} in the zirconia lattice, create oxygen vacancies so as to maintain the charge balance. Obviously, more oxygen vacancies are generated with more yttria introduced in the zirconia lattice. As shown in Fig.2.7, with more yttria (or, correlatively, oxygen vacancies) introduced the *k*-*T* curves of YSZ become flatter and the plateaus of these curves become lower, which indicates oxygen vacancies can markedly reduce *k* not only at low and intermediate temperatures, but also at high temperatures.

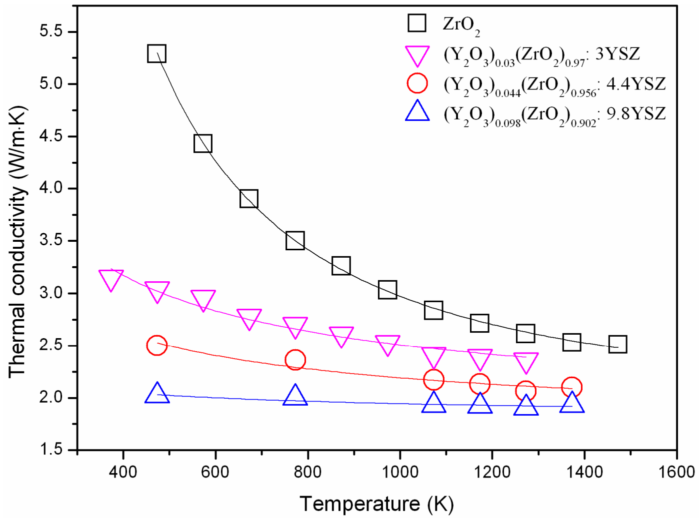

Fig.2.7 Thermal conductivities of ZrO_2 [9], 3YSZ [41], 4.4 YSZ [9] and 9.8 YSZ [9] at different temperatures. Data are extracted from references indicated and re-plotted.

While oxygen vacancies are so effective in scattering phonons and hence reducing *k* at such a wide temperature range, one tends to suggest introducing as many oxygen vacancies as possible to the lattice. Bisson et al [11] reported the thermal conductivity of YSZ with various yttria concentrations (or oxygen vacancy concentrations) at room temperature, as shown in Fig.2.8. With an increase of the $YO_{1.5}$ concentration, the *k* initially drops dramatically; it then continually decreases, but less markedly, until reaching its lowest value at the $YO_{1.5}$ content equalling 20% (i.e. 10 YSZ). Above this composition, the *k* however increases. The unexpected increase of *k* is caused by the short-range ordering of oxygen vacancies at high $YO_{1.5}$ concentrations. Specifically, as the $YO_{1.5}$ content increases, the vacancy pairs pack together in the <112> directions to form aggregates, with a short-range-order defect structure that resembles the long-range crystal structure of the ordered compound $Zr_3Y_4O_{12}$ [11]. Therefore, the more oxygen vacancies do not necessarily lead to a lower thermal conductivity, at least for the low temperature range. The randomness (order or disorder) of oxygen vacancies has an impact on phonon scattering and thus the *k* reduction.

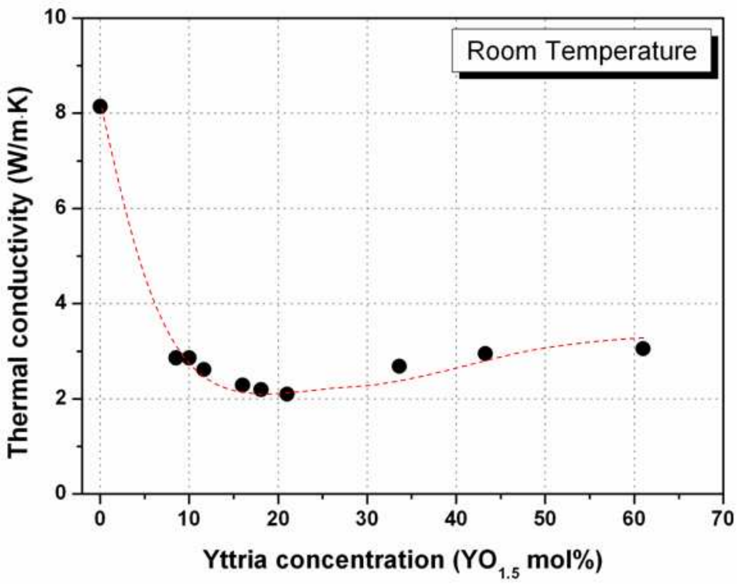

Fig.2.8 Thermal conductivity of various $Zr_{1-x}Y_xO_{2-x/2}$ samples at T = 300 K, as a function of yttria ($YO_{1.5}$) content, after [11].

2.2.3.2 Substitutional defects

Due to their easy introduction to the lattice, substitutional defects are the most widely-used method to further reduce thermal conductivity. In the literature, a wide variety of studies are dedicated to investigate the effect of substitutional atoms on reducing thermal conductivity, but there are still some issues that remain unclear. In this part, aiming at developing the most insulating TBC topcoat material, we focus on the doping of impurity atoms in two typical TBC materials: (1) the conventional tetragonal YSZ and (2) the next-generation $A_2B_2O_7$ pyrochlores.

(1) The doped tetragonal zirconia

For zirconia, the guest ions, also known as stabilizers, are added primarily to stabilize the tetragonal or cubic phase of zirconia. Their additional effect is to scatter phonons, which is strongly dependent on the valence of the stabilizer [42]. (1) When the dopants introduced to zirconia are subtetravalent oxides, e.g., yttria, calcia and magnesia, the most influential defects are the oxygen vacancies that are created for charge balance, while the cationic substitutional defects play a subsidiary role. (2) When the dopants are tetravalent oxides, such as ceria and hafnia, the cationic substitutional atoms are the ones dominating the phonon scattering. (3) When the dopants are supertetravalent oxide, such as tantala and niobia, it is difficult to introduce these pentavalent ions (Ta^{5+}, Nb^{5+}) only to the lattice, probably ascribed to the necessary creation of cationic vacancies to maintain the charge balance, which appears to be a difficult process. However, it is easier to introduce both trivalent oxides ($YO_{1.5}$, $YbO_{1.5}$) and pentavalent oxides ($TaO_{2.5}$, $NbO_{2.5}$) to the zirconia lattice, which are claimed to be without any oxygen vacancies [43]. In the following context, we are focusing on the latter two scenarios, which relate only to substitutional defects.

Winter and Clarke [44] reported the thermal conductivity of Hf doped YSZ, as shown in Fig.2.9. If ignoring the slightly increasing trend of k with temperature ascribed to the radiation contribution, all compositions of the fully dense materials essentially exhibit a temperature-independent k. More interestingly, the introduction of a heavier guest ion (Hf^{4+}) appears to be very effective in reducing the high temperature plateau thermal conductivity $k_{\min}$, which has been claimed as the first report of substitutional atoms lowering the high temperature plateau $k_{\min}$. The authors attributed this effect to the mass disorder on the cation sublattice of zirconia, in which Zr^{4+} ions were replaced and mixed with Hf^{4+} ions, as well as the anionic disorder created by oxygen vacancies introduced by the Y^{3+} stabilizer.

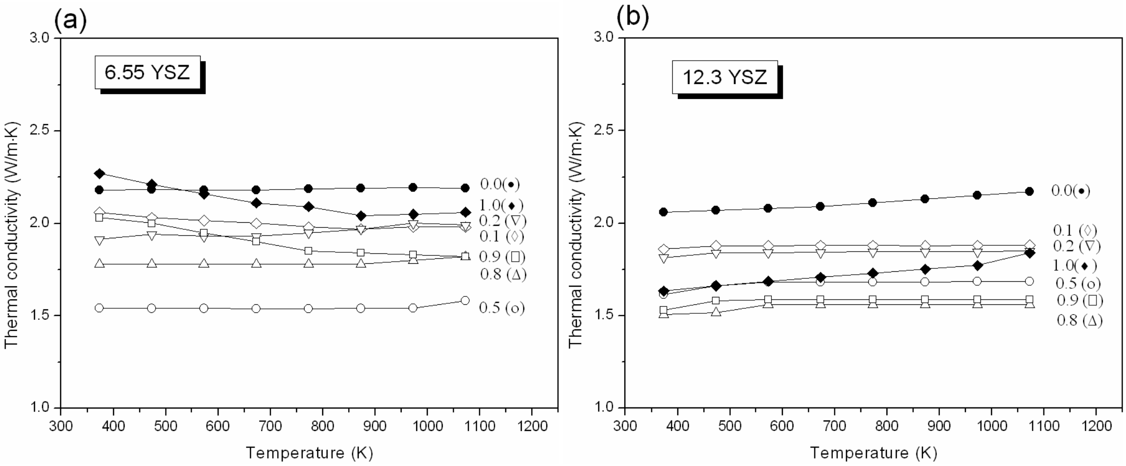

Fig.2.9 Thermal conductivity of Hf doped $(Y_2O_3)_{0.0655}(Zr_{1-x}Hf_xO_2)_{0.9345}$ (6.55 YSZ) (a) and $(Y_2O_3)_{0.123}(Zr_{1-x}Hf_xO_2)_{0.877}$ (12.3 YSZ) (b) at different temperatures, $x = 0.0, 0.1, 0.2, 0.5, 0.8, 0.9, 1.0$, after [44].

Raghavan et al [42] and Shen et al [43] reported zirconia co-doped by equimolar $YO_{1.5}$ and $Ta/NbO_{2.5}$, $Y/YbO_{1.5}$ and $TaO_{2.5}$, respectively. As envisaged, these samples are believed to be free of oxygen vacancies due to the substitution of the equimolar trivalent (Y^{3+}, Yb^{3+}) and pentavalent (Nb^{5+}, Ta^{5+}) cations for the Zr^{4+} hosts. Therefore, the phonon scattering is purely attributed to the substitutional defects. As shown in Fig.2.10, the thermal conductivities of equimolar co-doped zirconia unequivocally exhibit a temperature-independent, or even a slight increasing trend for some compositions, a typical sign of the existence of strong phonon scatterers. For example, as shown in Fig.2.10 (a), the 20 mol% $YNbO_4$ doped zirconia shows a temperature-independent k, very similar as that of the 19.6 mol% $YO_{1.5}$ stabilized zirconia (9.8 YSZ), which is however rendered by the oxygen vacancies. This indicates that, substitutional defects can be as strong phonon scatterers as vacancies, which is however inconsistent with the established understanding. According to Eq.(2.25), the scattering coefficient of substitutional defects is much less than that of vacancies, because both the mass and size differences of substitutional defects are much smaller than those of vacancies. In addition, from Fig.2.10 (b), the k of co-doped zirconia is steadily decreasing by adding heavier guest cations to the lattice.

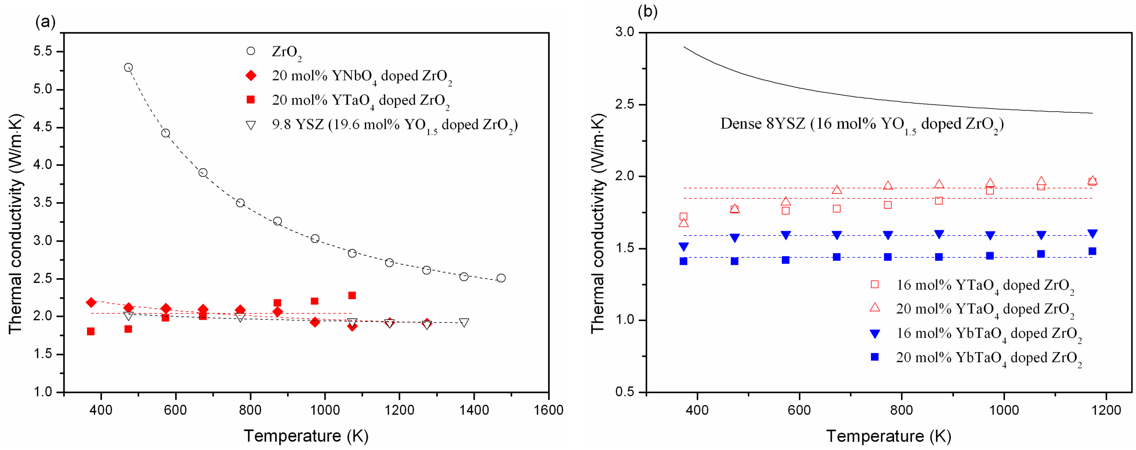

Fig.2.10 Temperature dependence of thermal conductivities of 20 mol% YNb/TaO$_4$ doped zirconia (a) and 16 mol% or 20 mol% Y/YbTaO$_4$ doped zirconia (b). Data are extracted from Ref. [42] and Ref. [43] respectively and re-plotted.

(2) The doped $A_2B_2O_7$ pyrochlores

Plenty of researches [39, 45-52] have been carried out to investigate the effect of doping substitutional atoms on heat conduction in $A_2B_2O_7$ pyrochlores. In general, due to the openness of the pyrochlore structure, there are two possible atomic sites (the A-sites and B-sites) that can accommodate impurity atoms. Firstly, Ref. [39, 45-50] reported the thermal conductivities of the $A_2B_2O_7$ pyrochlore solid solutions doped in the A-sites. Although different guest and host cations are involved in these studies, an interesting phenomenon can be found from all these different observations. As long as the pyrochlores are doped with a smaller cation on the A-site, their thermal conductivities tend to exhibit a temperature-independent or even a slightly increasing trend, a typical sign for the existence of strong phonon scatterers. However, if the A-site of pyrochlores is doped with a bigger cation, these strong phonon scatterers disappear and the influence of substitutional defects on heat transport returns to a normal level. Therefore, it is very likely that, there exists a strong phonon scattering source in the pyrochlore solid solutions doped with a smaller-sized guest ion on the A site of $A_2B_2O_7$ pyrochlores. Secondly, Ref. [51, 52] reported the B-site doping of $A_2B_2O_7$ pyrochlores. As already mentioned, because the backbone of the pyrochlore lattice is the corner-sharing BO_6 octahedra, the substitution of guest ions on the B-sites mainly affects the softness (or the elastic modulus) of the lattice, and therefore, according to Eq.(2.11), induces the possible reduction of the high temperature plateau k_{min}.

To sum up, on the influence of substitutional defects on heat conduction, the following questions still needs further investigation: (1) Can substitutional defects be as strong phonon scatterers as vacancies? (2) Can substitutional defects reduce the high temperature thermal conductivity? (3) Is there any strong phonon scattering source in the pyrochlore solid solutions doped by a smaller A-site guest ion? If any, what are those strong phonon scatterers?

2.2.4 Other strategies of reducing thermal conductivity

2.2.4.1 Disordering

The idea that the disordering helps to reduce thermal conductivity essentially stems from the fact that, the non-crystalline (i.e. amorphous) glass form of a compound, which lacks the long-range order, always possesses the lowest possible thermal conductivity, known as the amorphous limits [37]. As shown in Fig.2.8, the ordering of oxygen vacancies in the YSZ leads to a dramatic increase of thermal conductivity at relatively low temperatures. In other words, the randomization of atomic level features (i.e. vacancies, substitutional defects, etc.) tends to change the temperature dependence of the corresponding materials, which can be more clearly found in Fig.2.11 from Ref. [53]. Ref. [53] reported the thermal conductivity of Ce doped $(Y_2O_3)_{0.08}(ZrO_2)_{0.92}$ (8YSZ). As shown, while the ZrO_2-rich area ($x < 0.5$) shows a temperature-independent *k*, the CeO_2-rich area ($x > 0.5$) however exhibits a clear temperature-dependent *k*, which is quite distinctive from that (Fig.2.9) observed in Hf doped YSZ [44]. According to Ou and co-workers [54], the oxygen vacancies are ordered in yttria doped ceria (YDC). When Zr^{4+} is added to YDC, Zr^{4+} is prone to attract oxygen vacancies, which are normally associated with Y^{3+} ions. In other words, the adding of Zr^{4+} has redistributed and hence randomized the ordered oxygen vacancies. Therefore, it is the randomness of oxygen vacancies caused the distinctive temperature dependences in Ce doped 8YSZ.

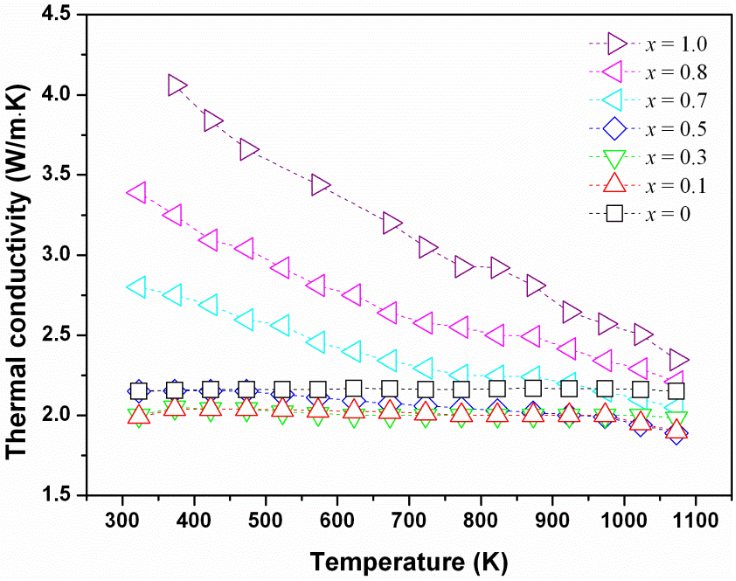

Fig.2.11 Thermal conductivities of the fully dense $(Zr_{1-x}Ce_xO_2)_{0.92}(Y_2O_3)_{0.08}$ ($0 \leq x \leq 1$) solid solutions at different temperatures, re-plotted after [53].

The change of temperature dependence of *k* can also be found in the process of pyrochlores transition to fluorites, which is accompanied by the increase of disordering of both oxygen vacancies and cations [55]. As mentioned in the preceding context, pyrochlores have ordered cations and oxygen vacancies (also known as structural defects) and their ordering extent strongly relies on the ratio of $r(A^{3+})/r(B^{4+})$ [55,56]. $A_2B_2O_7$ compounds with the largest $r(A^{3+})/r(B^{4+})$ ratio have the best ordered pyrochlores [56]. Consequently, the rare earth (RE) stannate pyrochlores in Fig.2.12 [57] are gradually becoming disordered with a decreasing radius of the RE elements from La to Yb. Accordingly, their *k*-*T* curves are gradually becoming flatter, or, more temperature-independent.

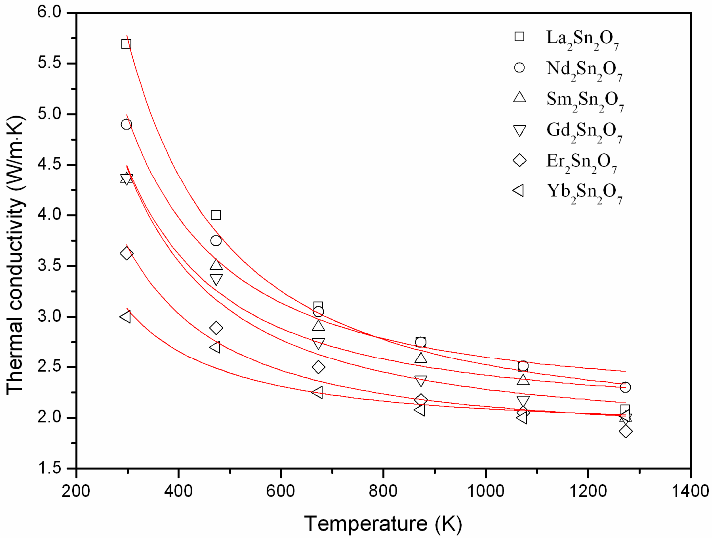

Fig.2.12 The temperature dependence of thermal conductivity of $RE_2Sn_2O_7$ series (RE = La, Nd, Sm, Gd, Er and Yb), re-plotted after Ref. [57]. The measurement uncertainty of the thermal conductivity is about ±0.1 $Wm^{-1}K^{-1}$ and the error bars are not shown for clarity. The solid lines are fitting curves according to Eq.(2.9).

2.2.4.2 Improve the interfacial thermal resistance

As discussed in Section 2.2.2, the grain boundaries are not very effective on scattering phonons, unless the grains are extremely small. The alternative approach is to improve the possibility of a phonon being scattered or reflected when crossing the boundary or interface, in other words, to improve the interfacial thermal resistance. While the possibility of a phonon being scattered or reflected is relatively small when crossing the boundaries with the same phase or structure at either side, it is then suggested to introduce a second phase with a highly dissimilar acoustic impedance Z ($Z = \rho \cdot v$, where ρ is the density and v is the phonon group velocity) [58]. The experimental work of Shen and co-workers [59] supports the existence of a strong interfacial thermal resistance arising from the alternating $(Bi_2Ti_3O_2)^{2-}$ and $(Bi_2O_2)^{2+}$ blocks, which have a thickness of 1.21 nm and 0.455 nm as well as a very dissimilar acoustic impedance ascribed to their very different densities but similar elastic modulus. By contrast, in another study, Yang et al [60] did not find an evident existence of the interfacial thermal resistance in $8YSZ/Al_2O_3$ composites and they attributed the following two reasons. Firstly, the grain sizes of the $8YSZ/Al_2O_3$ composites are not adequately small and they are still much bigger than the phonon mean free path in the composites; and secondly, the acoustic impedance is not adequately dissimilar between 8YSZ and Al_2O_3. Therefore, in order to exploit boundaries or interfaces as an effective phonon-scattering source, it is essential to create as many as possible interfaces between phases or nano-blocks that are highly dissimilar in terms of acoustic impedance.

2.3 Techniques of measuring thermal conductivity

2.3.1 Laser flash technique

The laser flash is a transient-state method of measuring the thermal diffusivity/ conductivity of a material. This technique is proposed by Parker [61] in 1961and now it becomes the most widely-used method to measure thermal conductivity, in particular for high temperatures.

Fig.2.13 schematically shows the basic setup of the laser flash system. During measurement, the front face of a planar sample is irradiated by a high-intensity short-duration (usually less than 1 ms) laser pulse. The temperature rise of the rear face of the sample is monitored by an infrared detector. The thermal diffusivity (α) can then be determined from the temperature versus time curve at the rear surface by [61]:

$$\alpha = \frac{1.38d^2}{\pi^2 t_{0.5}} = \frac{0.1388d^2}{t_{0.5}} \qquad (2.28),$$

in which d is the sample thickness and $t_{0.5}$ is the time required for the back surface to reach one half of the maximum temperature rise. Subsequently, thermal conductivity (k) can be calculated with the known density (ρ) and the specific heat capacity (C_p) according to the following relationship:

$$k = \alpha \cdot C_p \cdot \rho \qquad (2.29).$$

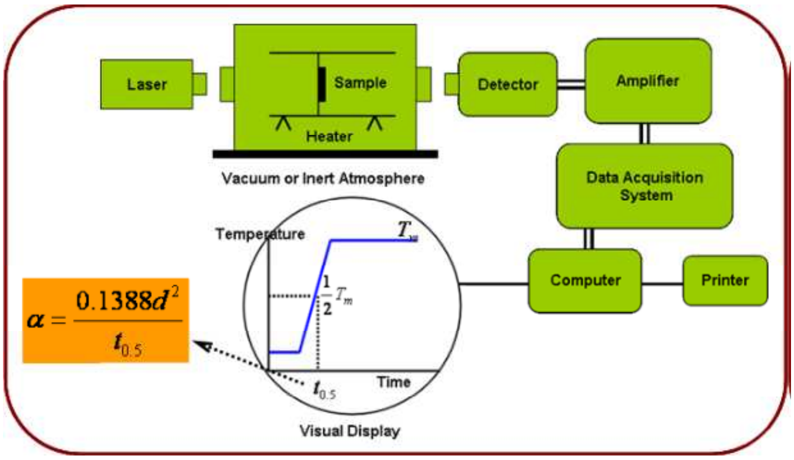

Fig.2.13 A schematic view of the laser flash system

Compared with the steady-state method, the flash method requires more sophisticated hardware but has easier sample preparation and, being noncontact, is much less sensitive to the issue of thermal contact resistance [62]. Only a small amount of material is needed for the measurement. However, a minimum thickness of the sample is usually required to guarantee that the heat diffusion time within the sample is much bigger than the duration of the laser pulse. For a low thermal conductivity material, a thickness of 1 mm is often adequate for the measurement.

2.3.2 Axial flow method [63]

As a steady-state conduction method, the principle of axial flow method is straightforward. According to Eq.(2.1), the thermal conductivity of a sample can be obtained by measuring a temperature difference across a sample in response to an applied amount of heating power. One of the most widely-used axial flow methods is the comparative cut bar method (ASTM E1225). The principle of the measurement is to pass the heat flux through a reference sample with a known thermal conductivity (k_R) and the test sample (k_S) and compare the temperature gradients inversely proportional to their thermal conductivities. The test sample is normally sandwiched between two reference samples so as to minimize the heat loss, as schematically shown in Fig.2.14. The thermal conductivity of the sample can be calculated by:

$$\frac{Q}{A} = k_S \frac{\Delta T_S}{L} = k_R \frac{\Delta T_1 + \Delta T_2}{2} \frac{1}{L}, \tag{2.30}$$

where Q is the heat input and A is the cross-section area.

The steady-state measurements have been long established. They are easy, direct and accurate at low temperatures. However, the issues like thermal contact and heat loss usually compromise the measuring accuracy. In addition, the measurement takes long time and requires a large specimen.

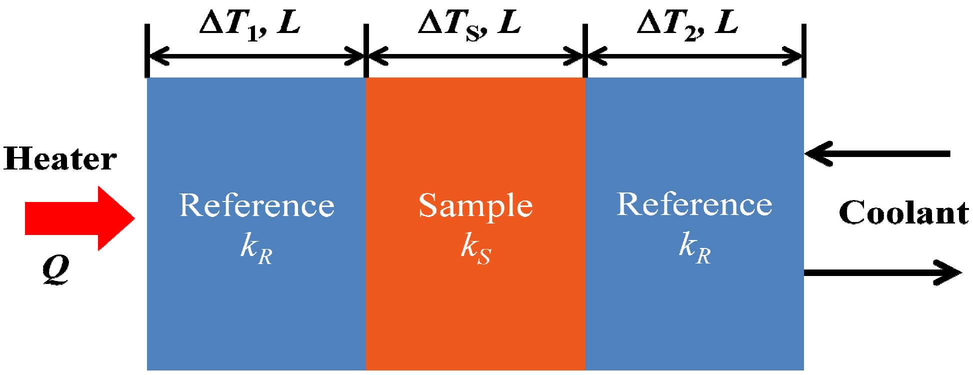

Fig.2.14 Schematic drawing of the comparative cut bar test: a steady-state measurement for thermal conductivity.

Other techniques, for example, 3ω technique [64], micro-Raman scattering [65], time-domain thermoreflectance (TDTF), the pulse-power method [67], thermography

[11], are all widely used to measure thermal conductivity, with some more appropriate to specific sample geometry, such as the 3ω technique for thin films. The details of these techniques can be found in the relevant references.

2.4 Summary of Part I

In the part I of this chapter, the fundamentals of heat conduction in ceramics have been reviewed. Accordingly, the corresponding strategies to reduce thermal conductivity in ceramics have been discussed in detail. The main points can be summarized as follows:

(1) To reduce the intrinsic thermal conductivity of a ceramic, or the thermal conductivity at high temperatures for the application such as thermal barrier coatings, we need to increase lattice anharmonicity as well as reduce phonon group velocity, both of which relate to the nature of bonds in a ceramic.

(2) It is not practically feasible to exploit grain boundaries to scatter phonons, because ultrafine grains (about 10~15 nm for both YSZ and $A_2B_2O_7$-type pyrochlores) are required to produce an evident phonon scattering effect by grain boundaries. Regardless of the difficulty in manufacturing nano-sized TBCs, these ultrafine nano-structures are susceptible to collapse after the high-temperature exposure.

(3) Although it is suggested to introduce a second phase that is highly dissimilar with the matrix in acoustic impedance to improve phonon scattering at interfaces/boundaries, it is yet to find such a second phase in the $La_2Zr_2O_7$ matrix.

(4) Oxygen vacancies and substitutional atoms, particularly the former, can effectively reduce k. Although plenty of studies have been carried out on the effect of substitutional defects on k, the following issues still remains unclear and is therefore worth further investigation. Can substitutional atoms be as strong phonon scatterers as vacancies? Can substitutional atoms reduce the high-temperature k? Is there any additional phonon scattering mechanism in $A_2B_2O_7$ pyrochlores doped with a smaller guest ion on the A-site?

(5) Laser flash technique is a reliable and convenient method to measure the thermal conductivity of a ceramic from the room temperature to high temperatures.

Part II Improvement of fracture toughness of the $La_2Zr_2O_7$-based pyrochlore ceramic

2.5 Toughening mechanisms in ceramics

The most remarkable shortcoming of ceramics is their nature of brittleness which severely undermines the basis of their wide application as engineering materials, because they are prone to fail suddenly without any signs. In particular for the TBC applications that require high durability and reliability, the brittleness (i.e. low resistance to fracture) of $La_2Zr_2O_7$ cubic pyrochlores has severely limited their applications as TBCs. Therefore, researchers are seeking the toughening of ceramics. Despite of various mechanisms proposed or already employed to toughen a ceramic, the essence of any toughening effect is the possible existence of a mechanism for absorption and subsequent dissipation of mechanical energy of applied forces in the immediate vicinity of a crack tip so that additional energy must be supplied to effect crack propagation [68]. This absorbed energy reflects as an increase in fracture toughness. The most effective and well-known dissipative mechanism is plastic deformation [68] in the vicinity of a crack tip, which is however not as pronounced in ceramics as in metals. Other mechanisms include frictional work in fibre-reinforced composites, microcracking, crack bridging, ferroelastic domain switching, etc. An increase in the apparent toughness can also be realized by creating a state of compression on crack surfaces (crack shielding) so that additional force must be applied to overcome this shielding effect. The toughening effects arising from the crack shielding include phase transformation toughening, residual compressive stress toughening, etc. In the following parts, some typical toughening mechanisms are reviewed for ceramic materials.

2.5.1 Phase transformation toughening [69-71]

The famous example of phase transformation toughening is the *t*-*m* phase transformation in zirconia, which can be used to improve the strength and fracture toughness of materials with appropriate composition through careful microstructure control. In phase transformation toughening, the source of the toughening effect is related to crack shielding which arises from the local expansion of the material upon *t*-*m* transition accompanied by a volume increase. This volume increase creates a zone of compression around the crack which essentially reduces the effect of the applied load. The net effect is that the applied load must be increased further to offset the surface compression. The primary fabrication objective for any transformation-toughened ceramic material is production and retention of a metastable t-ZrO_2 phase that transforms to m-ZrO_2 at/or near room temperature under the influence of any applied stress including a significant shear component. The effectiveness of toughness improvement by the *t*-*m* phase transformation is affected by the type and concentration of the stabilizer solute, the grain size, and the temperature etc. The strength and fracture toughness of a transformation-toughened ceramic decrease with an increase of temperature, because the stability of the *t* phase increases, and there is a decrease in the chemical driving force for the *t-m* transformation. Therefore, the phase transformation toughening is a low-temperature toughening mechanism and not effective at high temperatures.

2.5.2 Ferroelastic domain switching (FDS) toughening [68, 72, 73]

Ferroelastic domain switching (FDS) is another effective toughening mechanism, which exists in ferroelastic materials. A ferroelastic material is characterized by the existence of a strain in the absence of an applied stress, wherein the sense of the strain can be reversed by a suitably applied mechanical stress. The ferroelastic material usually has the tetragonal instead of cubic phase, as the cubic phase can not be a ferroelastic and thus cannot exhibit domain switching. Fig.2.15 schematically demonstrates the process of ferroelastic domain switching of tetragonal zirconia. In the vicinity (ahead) of a crack tip, there exists a ferroelastic domain with its c-axis in the plane of the crack. By applying an external load which attempts to extend a crack in a body, the stress is tensile immediately ahead of the crack tip and in a direction perpendicular to the crack plane. If the stress exceeds a critical value (the coercive stress), the a-axis will switch into the c-axis. This leads to the absorption and the eventual dissipation of mechanical energy as heat. Once the stress at the crack tip reaches the critical stress necessary for the occurrence of crack growth, the crack then propagates. Therefore, the energy required for crack propagation increases by an amount corresponding to that required for domain switching, leading to an increase of fracture toughness. On the other hand, the toughening effect by ferroelastic domain switching can be explained by the crack shielding, because the crack surface is under a compressive state as the domains switch. Different from the phase transformation toughening that is only applicable to the medium-to-low temperature range, the toughness associated with ferroelastic switching is insensitive to temperature, suggesting that this mechanism is still effective at high temperatures. Therefore, the ferroelastic domain switching is very attractive for the toughening of ceramics operating under high temperatures, such as those for TBC application.

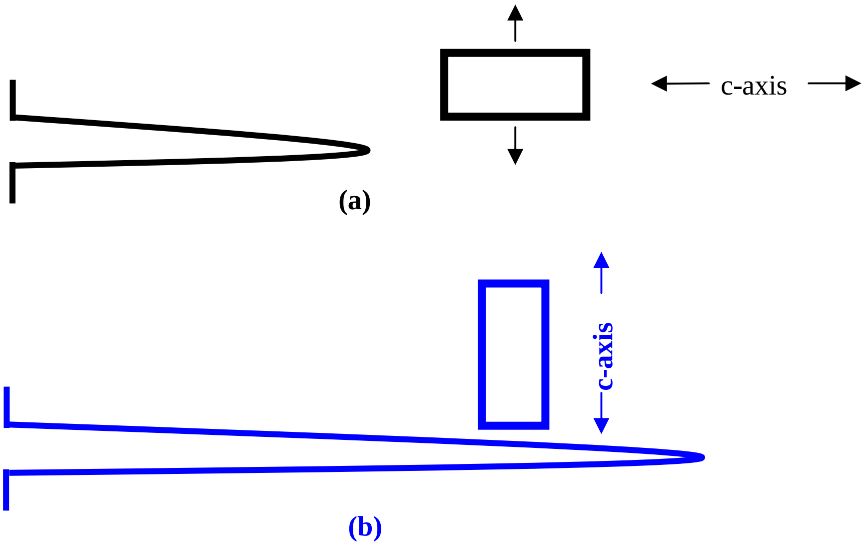

Fig.2.15 A schematic drawing shows the occurrence of domain switching in tetragonal zirconia during crack growth, after [68].

2.5.3 Residual compressive stress toughening [74]

The principle of compressive stress toughening, as suggested by its name, is to cause the compressive stress state in the ceramic matrix to shield crack extension by means of introducing a second phase in the form of particles, fibres, whiskers, etc. Upon cooling down from the fabrication temperature, a residual compressive or tensile stress is introduced in the ceramic matrix due to the thermal expansion coefficient (TEC) mismatch. To achieve the residual compressive stress in the matrix, it is essential to introduce a second phase with a lower TEC than its matrix. Fig.2.16 schematically demonstrates a crack propagating from matrix compressive region towards particulate tensile region in particulates reinforced ceramic composites. In this system, Taya and co-workers [74] proposed a model to account for the fracture toughness improvement purely due to the residual compressive stress (ΔK_{Ic}), as described by the following equation:

$$\Delta K_{Ic} = 2\sigma_m \sqrt{\frac{2D}{\pi}} \tag{2.31}$$,

in which *D* is the average particulate spacing; and σ_m is the local compressive stress in the matrix.

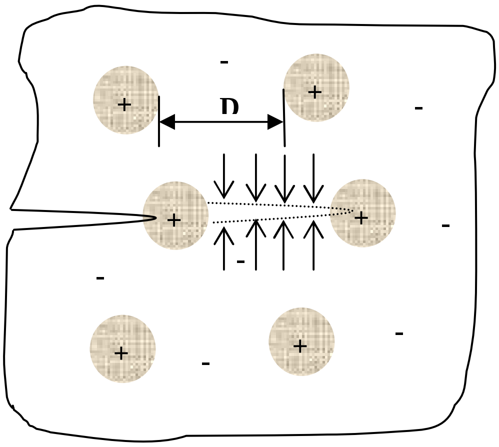

Fig.2.16 Semi-infinite crack advances through matrix compressive region toward particulate tensile region. '+' and '-' denote tensile and compressive stress respectively, after [74].

Except the above three toughening effects, there are many other mechanisms not discussed in detail here, such as frictional work in fibre-reinforced composites [75], crack depletion [76], micro-crack toughening [77], micro-crack bridging [76], etc. The details of these toughening mechanisms can be found in the relevant references indicated. It is worth pointing out that, although one or two mechanism(s) might be dominant in a specific material system, several mechanisms could act in concert adding up to the inherent toughness of a material.

2.6 Techniques measuring the fracture toughness of ceramics

The definition of fracture toughness from Munz and Fett [78] is: if a component or a test specimen with a crack is loaded, the stress intensity, K_I increases with increasing load until unstable crack propagation occurs at a critical value of K_I. This critical value is the fracture toughness (K_{Ic}). Therefore, the measurement of fracture toughness should be made on samples with a pre-existent crack. The standard test of fracture toughness is the bending test of a bulk specimen with a pre-existent crack (or notch), whilst the indentation technique is another widely used method to evaluate the fracture toughness of ceramics and coating systems because it is easy to perform, does not need special samples and causes only negligible surface damage.

2.6.1 The bending test

Generally, there are two typical bending tests: the three-point bending and the four-point bending test. Fig.2.17 exhibits the schematic drawing of the four-bending test on a bending beam with a pre-existent crack (for the three-point bending, the principle is similar but it employs another set of formulism). The fracture toughness can then be calculated by the following equation [79]:

$$K_{Ic} = \frac{P(d_1 - d_2)}{t \cdot w^{1.5}} \times \frac{3F(\alpha)\alpha^{0.5}}{2(1-\alpha)^{1.5}} \tag{2.32a),}$$

$$F(\alpha) = 1.9887 - 1.326\alpha - \frac{(3.49 - 0.68\alpha + 1.35\alpha^2)\alpha(1-\alpha)}{(1+\alpha)^2} \tag{2.32b),}$$

in which α = *l*/*w*; *P* is the fracture load; *w* and *t* are the width and thickness of the beam respectively; d_1 and d_2 are the outer span and inner span respectively; and *l* is the notch depth or pre-crack length. The major advantage of the bending test is its reliability. However, it usually requires precise sample geometry, adding the difficulty of sample preparations.

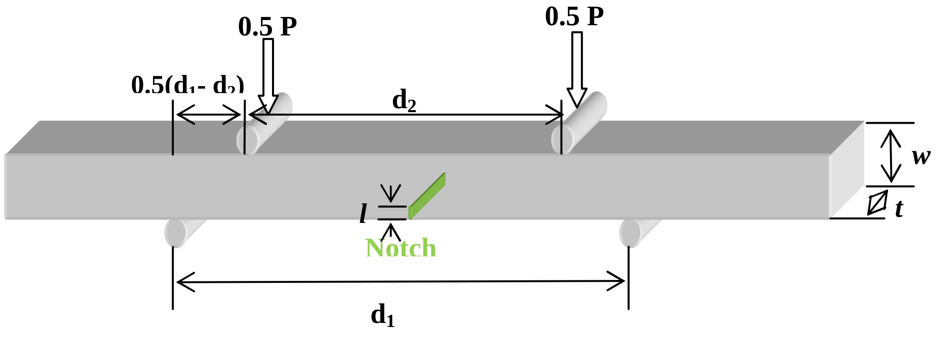

Fig.2.17 The schematic drawing of four-point bending test of a specimen with a pre-existent crack to determine its fracture toughness

2.6.2 The indentation technique

The indentation technique is an effective way to compare the fracture behaviour of materials and provides information of crack initiation and propagation. Fig.2.18 is the typical characterization of the crack system generated by Vickers indentation [80]. This crack system is termed as median-radial cracking and consists of approximately semi-circular cracks. According to Chiang et al [81], radial cracks are the first to initiate, triggered by a combination of the highly tensile surface stress filed and the availability of surface flaws. These cracks grow on unloading, and can either propagate into the plastic zone (half penny cracks), or terminate in the elastic zone (Palmqvist cracks), depending on the microstructure of the material.

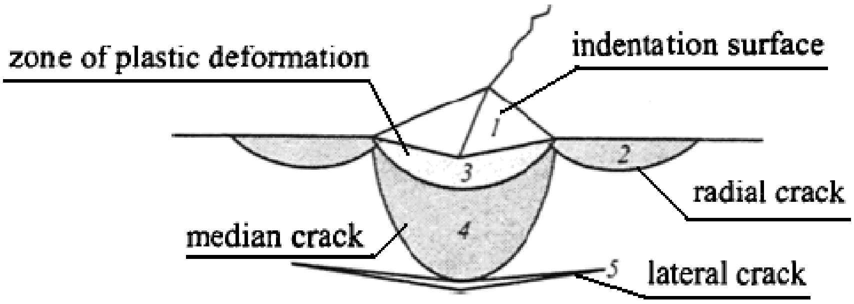

Fig.2.18 A schematic drawing of a plastic indentation and cracks formed under an indenter [80].

For different types of crack modes such as half-penny and Palmqvist cracks, different equations were developed, based on theoretical analysis of stress field and empirically calibration, to calculate the fracture toughness under indentation. For example, in the half penny crack model, the Vickers indentation fracture toughness was determined using the relationship proposed by Antis et al [82]:

$$K_{IC} = \chi\sqrt{\frac{E}{H}}\frac{P}{c^{1.5}} \quad (2.33),$$

in which P is the applied load; E and H are the Young's modulus and hardness of the material; c is the radical crack length from indentation centre to crack tip; and χ is a geometrical constant and independent of the material. This equation was developed on the basis of half penny cracking in homogeneous brittle materials under high loads, for example in glasses.

Recently, Quinn et al [83] raised a strong criticism on the Vickers indentation fracture toughness test. They suggested the indentation fracture toughness test is fundamentally different than standard fracture toughness tests. The indentation technique has a complex three-dimensional crack system with substantial deformation residual stresses and damage around cracks. Despite of these considerations, the indentation method is an effective way to compare the fracture behaviour of materials and is particularly useful for the comparative measurements of homogeneous ceramics to rank the performance of crack resistance in brittle materials [84].

2.7 Summary of Part II

In part II of this chapter, the toughening mechanisms in ceramics have been reviewed and the typical techniques of measuring fracture toughness have been briefly introduced. We can summarize as follows:

(1) While phase transformation toughening appears to be a very effective toughening mechanism, it is only valid at relatively low temperatures and thus not attractive for the toughening of TBC topcoat that operates at high temperatures.

(2) The ferroelastic domain switching, despite of its less effect than the phase transformation toughening, is effective at high temperatures and hence a high-temperature toughening mechanism. Therefore, it is an ideal toughening mechanism for TBC topcoat.

(3) Although doubts have been raised on the validity of the indentation technique measuring the fracture toughness, it is suitable for the comparative measurements to rank the order of performance in fracture resistance among different samples.

References

[1] S. R. Phillpot and A.J.H. McGaughey. *Introduction to thermal transport*. Materials Today **8** (2005) 18-20.

[2] C.Kittel. *Introduction to solid state physics*. New York, John Wiley & Sons, 2005.

[3] P.G. Klemens. *Theory of thermal conduction in thin ceramic films*. Int J Thermophys **22** (2001) 265-275.

[4] C.T. Walker and R.O. Pohl. *Phonon Scattering by Point Defects*. Phys Rev **131** (1963) 1433-1442.

[5] P.G. Klemens and M. Gell. *Thermal conductivity of thermal barrier coatings*. Mat Sci Eng A-Struct 245 (1998) 143-149.

[6] B.C. Sales, D. Mandrus and R.K. Williams. *Filled skutterudite antimonides: a new class of thermoelectric materials*. Science **272** (1996) 1325-1328.

[7] V. Keppens, D. Mandrus, B.C. Sales, B.C. Chakoumakos, P. Dai, R. Coldea, M.B.Maple, D.A.Gajewski, E.J. Freeman and S.Bennington. *Localized vibrational modes in metallic solids*. Nature **395** (1998) 876-878.

[8] V. Keppens, B.C. Sales, D. Mandrus, B.C. Chakoumakos and C. Laermans. *When does a crystal conduct heat like a glass?* Phil Mag Lett **80** (2000) 807-812.

[9] R. Mevrel, J.-C. Laizet, A. Azzopardi, B. Leclercq, M. Poulain, O.Lavigne and D. Demange. *Thermal diffusivity and conductivity of* $Zr_{1-x}Y_xO_{2-x/2}$ *(x = 0, 0.084 and 0.179) single crystals*. J Eur Ceram Soc **24** (2004) 3081-3089.

[10] M. Roufosse and P.G. Klemens. *Thermal conductivity of complex dielectric crystals*. Phys Rev B **7** (1973) 5379-5386.

[11] J.F. Bisson, D. Fournier, M. Poulain, O. Lavigne and R. Mevrel. *Thermal conductivity of yttria-zirconia single crystals, determined with spatially resolved infrared thermography*. J Am Ceram Soc **83** (2000) 1993-1998.

[12] D.R. Clarke. *Materials selection guidelines for low thermal conductivity thermal barrier coatings*. Surf Coat Technol **163-164** (2003) 67-74.

[13] G. Grimvall. *Thermophysical properties of materials*. North-Holland, Elsvier, 1999.

[14] P.G. Klemens. *The scattering of low-frequency lattice waves by static imperfections*. Proc Phys Soc Lond A **68** (1955) 1113-1128.

[15] P.G. Klemens. *Phonon scattering and thermal resistance due to grain boundaries*. Int J Thermophys **15** (1994) 1345-1351.

[16] R.O. Pohl. *Thermal conductivity and phonon resonance scattering*. Phys Rev Lett **8** (1962) 481-483.

[17] W.D. Seward and V. Narayanamurti. *Rotational degrees of freedom of molecules in solids: 1 Cyanide ion in alkali halides*. Phys Rev **148** (1966) 463-481.

[18] J.S. Tse and M.A.White. *Origin of glassy crystalline behavior in the thermal properties of clathrate hydrates - a thermal conductivity study of tetrahydrofuran hydrate*. J Phys Chem **92** (1988) 5006-5011.

[19] G.S. Nolas, J.L. Cohn, G.A. Slack and S.B. Schujman. *Semiconducting Ge clathrates: promising candidates for thermoelectric applications*. Appl Phys Lett **73** (1998) 178-180.

[20] J.S. Tse, V.P. Shpakov, V.R. Belosludov, F. Trouw, Y.P. Handa and W. Press. *Coupling of localized guest vibrations with the lattice modes in clathrate hydrates*. Europhys Lett **54** (2001) 354-360.

[21] Z. Hiroi, J. Yamaura and K. Hattori. *Rattling good superconductor: β-pyrochlore Oxides AOs_2O_6*. J Phys Soc Jpn **81** (2012) 011012 1-24.

[22] Y.G. Wang, X.F. Xu and J.H. Yang. *Resonant oscillation of misch-metal atoms in filled skutterudites*. Phys Rev Lett **102** (2009) 175508 1-4.

[23] A.D. Caplin, G. Gruner and J.B. Dunlop. *$Al_{10}V$- Einstein solid*. Phys Rev Lett **30** (1973) 1138-1140.

[24] J.L. Cohn, G.S. Nolas, V. Fessatidis, T.H. Metcalf and G.A. Slack. *Glasslike heat conduction in high-mobility crystalline semiconductors*. Phys Rev Lett **82** (1999) 779-782.

[25] E.S. Toberer, A. Zevalkink and G.J. Snyder. *Phonon engineering through crystal chemistry*. J Mater Chem **21** (2011) 15843-15852.

[26] M. Christensen, A. B. Abrahamsen, N. B. Christensen, F. Juranyi, N. H. Andersen, K. Lefmann, J. Andreasson, C. R. H. Bahl and B. B. Iversen. *Avoided crossing of rattler modes in the thermoelectric materials*. Nat Mater **7** (2008) 811-815.

[27] D. T. Morelli, V. Jovovic and J. P. Heremans. *Intrinsically minimal thermal conductivity in cubic I-V-VI_2 semiconductors*. Phys Rev Lett **101** (2008) 035901 1-4.

[28] E. J. Skoug and D. T. Morelli. *Role of lone-pair electrons in producign minimum thermal conductivity in nitrogen-group chalcogenide compounds*. Phys Rev Lett **107**, (2011) 235901 1-4.

[29] M.D. Nielsen, V. Ozolins and J.P. Heremans. *Lone pair electrons minimize lattice thermal conductivity*. Energ Environ Sci **6** (2013) 570-578.

[30] O. Delaire, J. Ma, K. Marty, A. F. May, M. A. McGuire, M. H. Du, D. J. Singh, A. Podlesnyak, G. Ehlers, M. D. Lumsden and B. C. Sales. *Giant anharmonic phonon scattering in PbTe*. Nat Mater **10** (2011) 614-619.

[31] S. Raghavan, H. Wang, R.B. Dinwiddie, W.D. Porter and M.J. Mayo. *The effect of grain size, porosity and yttria content on the thermal conductivity of nanocrystalline zirconia*. Scripta Mater **39** (1998) 1119-1125.

[32] A.M. Limarga and D.R. Clarke. *The grain size and temperature dependence of the thermal conductivity of polycrystalline, tetragonal yttria-stabilized zirconia*. Appl Phys Lett **98** (2011) 211906 1-3.

[33] G. Soyez G, J.A. Eastman, L.J. Thompson, G.R. Bai, P.M. Baldo, A.W. McCormick, R.J. DiMelfi, A.A. Elmustafa, M.F. Tambwe and D.S. Stone. *Grain-size-dependent thermal conductivity of nanocrystalline yttria-stabilized zirconia films grown by metal-organic chemical vapor deposition*. Appl Phys Lett **77** (2000) 1155-1157.

[34] H.S. Yang, G.R. Bai, L.J. Thompson and J.A. Eastman. *Interfacial thermal resistance in nanocrystalline yttria-stabilized zirconia*. Acta Mater **50** (2002) 2309-2317.

[35] O.J. Dura, E. Bauer, L. Vazquez and M.A.L. de la Torre. *Depressed thermal conductivity of mechanically alloyed nanocrystalline 10 mol% yttria-stabilized zirconia*. J Phys D Appl Phys **43** (2010) 105407 1-6.

[36] F.J. Walker and A.C. Anderson. *Low-energy excitations in yttria-stabilized zirconia*. Phys Rev B **29** (1984) 5881-5890.

[37] D.G. Cahill, S.K. Watson and R.O. Pohl. *Lower limit to the thermal conductivity of disordered crystals*. Phys Rev B Condens Matter **46** (1992) 6131-6140.

[38] D.P.H. Hasselman, L.F. Johnson, L.D. Bentsen, R. Syed, H.L. Lee and M.V. Swain. *Thermal diffusivity and conductivity of dense polycrystalline* ZrO_2 *ceramics - a survey*. Am Ceram Soc Bull **66** (1987) 799-806.

[39] C.L.Wan, W. Pan, Q. Xu, Y.X. Qin, J.D. Wang, Z.X. Qu and M.H. Fang. *Effect of point defects on the thermal transport properties of* $(La_xGd_{1-x})_2Zr_2O_7$*: experiment and theoretical model*. Phys Rev B **74** (2006) 144109 1-9.

[40] J.D. Eshelby. *The continuum Theory of Lattice Defects*, in: F. Seitz, D. Turnbull (Eds.). *Solid State Physics*, Vol.3. New York, Academic Press Inc., 1956.

[41] K.W. Schlichting, N.P. Padture and P.G. Klemens. *Thermal conductivity of dense and porous yttria-stabilized zirconia*. J Mater Sci **36** (2001) 3003-3010.

[42] S. Raghavan, H. Wang, W.D. Porter, R.B. Dinwiddie and M.J. Mayo. *Thermal properties of zirconia co-doped with trivalent and pentavalent oxides*. Acta Mater **49** (2001) 169-179.

[43] Y. Shen, R.M. Leckie, C.G. Levi and D.R. Clarke. *Low thermal conductivity without oxygen vacancies in equimolar* $YO_{1.5}$ + $TaO_{2.5}$ *and* $YbO_{1.5}$ + $TaO_{2.5}$*-stabilized tetragonal zirconia ceramics*. Acta Mater **58** (2010) 4424-4431.

[44] M.R. Winter and D.R. Clarke. *Thermal conductivity of yttria-stabilized zirconia-hafnia solid solutions*. Acta Mater **54** (2006) 5051-5059.

[45] P.K. Schelling. *Thermal conductivity of A-site doped pyrochlore oxides studied by molecular-dynamics simulation*. Comp Mater Sci **48** (2010) 336-342.

[46] H. Lehmann, D. Pitzer, G. Pracht, R. Vassen and D. Stover. *Thermal conductivity and thermal expansion coefficients of the lanthanum rare-earth-element zirconate system*. J Am Ceram Soc **86** (2003):1338-1344.

[47] C. Bryan, C.A. Whitman, M.B. Johnson, J.F. Niven, P. Murray, A. Bourque, H.A. Dabkowska, B.D. Gaulin and M.A. White. *Thermal conductivity of* $(Er_{1-x}Y_x)_2Ti_2O_7$ *pyrochlore oxide solid solutions*. Phys Rev B **86** (2012) 054303 1-7.

[48] C.L. Wan, Z.X. Qu, A.B. Du and W. Pan. *Order-disorder transition and unconventional thermal conductivities of the* $(Sm_{1-x}Yb_x)_2Zr_2O_7$ *series*. J Am Ceram Soc **94** (2011) 592-596.

[49] Z.X. Qu, C.L. Wan and W. Pan. *Thermal expansion and defect chemistry of MgO-Doped* $Sm_2Zr_2O_7$. Chem Mater **19** (2007) 4913-4918.

[50] J. Feng, B. Xiao, C.L. Wan, Z.X. Qu, Z.C. Huang, J.C. Chen, R. Zhou and W. Pan. *Electronic structure, mechanical properties and thermal conductivity of* $Ln_2Zr_2O_7$ *(Ln = La, Pr, Nd, Sm, Eu and Gd) pyrochlore*. Acta Mater **59** (2011) 1742-1760.

[51] C.L. Wan, Z.X. Qu, A.B. Du and W. Pan. *Influence of B site substituent Ti on the structure and thermophysical properties of* $A_2B_2O_7$*-type pyrochlore* $Gd_2Zr_2O_7$. Acta Mater **57** (2009) 4782-4789.

[52] B. Liu, J.Y. Wang, F.Z. Li and Y.C. Zhou. *Theoretical elastic stiffness, structural stability and thermal conductivity of* $La_2T_2O_7$ *(T = Ge, Ti, Sn, Zr, Hf) pyrochlore*. Acta Mater **58** (2010) 4369-4377.

[53] F. Yang, X. F. Zhao and P. Xiao. *The effects of temperature and composition on the thermal conductivities of* $[(ZrO_2)_{1-x}(CeO_2)_x]_{0.92}(Y_2O_3)_{0.08}$ $(0 \leq x \leq 1)$ *solid solutions*. Acta Mater **60** (2012) 914-922.

[54] D.R. Ou, T. Mori, F. Ye, T. Kobayashi, J. Zou, G. Auchterlonie and J. Drennan. *Oxygen vacancy ordering in heavily rare-earth-doped ceria*. Appl Phys Lett **89** (2006) 171911 1-3.

[55] L. Minervini, R.W. Grimes and K.E. Sickafus. *Disorder in pyrochlore oxides*. J Am Ceram Soc **83** (2000) 1873-1878.

[56] B.J. Wuensch and K.W. Eberman. *Order-disorder phenomena in* $A_2B_2O_7$ *pyrochlore oxides*. Jom-J Min Met Mat S **52** (2000) 19-21.

[57] Z.X. Qu, C.L. Wan and W. Pan. *Thermophysical properties of rare-earth stannates: Effect of pyrochlore structure*. Acta Mater **60** (2012) 2939-2949.

[58] E.T. Swartz and R.O. Pohl. *Thermal-boundary resistance*. Rev Mod Phys **61** (1989) 605-668.

[59] Y. Shen, D.R. Clarke and P.A. Fuierer. *Anisotropic thermal conductivity of the Aurivillus phase, bismuth titanate, ($Bi_4Ti_3O_{12}$): A natural nanostructured superlattice*. Appl Phys Lett **93** (2008) 102907 1-3.

[60] F. Yang, X.F. Zhao and P. Xiao. *Thermal conductivities of YSZ/Al_2O_3 composites*. J Eur Ceram Soc **30** (2010) 3111-3116.

[61] W.J. Parker, R.J. Jenkins, G.L. Abbott and C.P. Butler. *Flash method of determining thermal diffusivity, heat capacity, and thermal conductivity*. J Appl Phys **32** (1961) 1679-1684.

[62] E.S. Toberer, L.L. Baranowski and C. Dames. *Advances in thermal conductivity*. Annu Rev Mater Res **42** (2012) 179-209.

[63] E1225-09. *Standard test method for thermal conductivity of solids by means of the guarded-comparative-longitudinal heat flow technique*. West Conshohocken, PA: ASTM International, (2009).

[64] D.G. Cahill. *Thermal conductivity measurement from 30 K to 750 K: the 3 ω method*. Rev Sci Instrum **61** (1990) 802-808.

[65] S. Perichon, V. Lysenko, B. Remaki, D. Barbier and B. Champagnon. *Measurement of porous silicon thermal conductivity by micro-Raman scattering*. J Appl Phys **86** (1999) 4700-4702.

[66] D.G. Cahill. *Analysis of heat flow in layered structures for time-domain thermoreflectance*. Rev Sci Instrum **75** (2004) 5119-5122.

[67] T.M. Tritt. *Thermal conductivity theory, properties, and applications*. Springer, (2004).

[68] A.V. Virkar. *Role of ferroelasticity in toughening of zirconia ceramics*. Key Eng Mat **153-154** (1998) 183-210.

[69] R.H.J. Hannink, P.M. Kelly and B.C. Muddle. *Transformation toughening in zirconia-containing ceramics*. J Am Ceram Soc **83** (2000) 461-487.

[70] I. Nettleship and R. Stevens. *Tetragonal zirconia polycrystal (TZP)- a review*. Int J High Technol Ceram **3** (1987) 1-32.

[71] J. Chevalier, L. Gremillard, A.V. Virkar and D.R. Clarke. *The tetragonal-monoclinic transformation in zirconia: lessons learned and future trends*. J Am Ceram Soc **92** (2009) 1901-1920.

[72] C. Mercer, J.R. Williams, D.R. Clarke and A.G. Evans. *On a ferroelastic mechanism governing the toughness of metastable tetragonal-prime (t') yttria-stabilized zirconia*. Proc R Soc A-Math Phy **463** (2007) 1393-1408.

[73] A.V. Virkar and R.L.K. Matsumoto. *Ferroelastic domain switching as a toughening mechanism in tetragonal zirconia*. J Am Ceram Soc **69** (1986) C224-C226.

[74] M. Taya, S. Hayashi, A.S. Kobayashi and H.S. Yoon. *Toughening of a particulate-reinforced ceramic-matrix composite by thermal residual stress*. J Am Ceram Soc **73** (1990) 1382-1391.

[75] A.G. Evans and F.W. Zok. *The physics and mechanics of fiber-reinforced brittle-matrix composites*. J Mater Sci **29** (1994) 3857-3896.

[76] J.W. Hutchinson. *Mechanisms of toughening in ceramics*. In: *Proceedings of the 17th international congress on theoretical and applied mechanics*. Grenoble, Elsevier (1988), p.139.

[77] M. Ruhle, N. Claussen and A.H. Heuer. *Transformation and microcrack toughening as complementary processes in ZrO_2-toughened Al_2O_3*. J Am Ceram Soc **69** (1986) 195-197.

[78] D.Munz and T. Fett. *Ceramics: Mechanical properties, failure properties, failure behavior, and materials selection*. New York, Springer Verlag, (1999).

[79] M. Mizuno and H. Okuda. *Vamas round-robin on fracture-toughness of silicon-nitride.* J Am Ceram Soc **78** (1995) 1793-1801.

[80] R.F. Cook and G.M. Pharr. *Direct observation and analysis of indentation cracking in glasses and ceramics*. J Am Ceram Soc **73** (1990) 787-817.

[81] S.S. Chiang, D.B. Marshall and A.G. Evans. *The response of solids to elastic plastic indentation :1. Stresses and residual stresses*. J Appl Phys **53** (1982) 298-311.

[82] G.R. Anstis, P. Chantikul, B.R. Lawn and D.B. Marshall. *A critical evaluation of indentation techniques for measuring fracture toughness: 1. Direct crack measurement*. J Am Ceram Soc **64** (1981) 533-538.

[83] G.D. Quinn and G.D. Bradt. *On the Vickers indentation fracture toughness test*. J Am Ceram Soc **90** (2007) 673-680.

[84] R. Morrell. *Fracture toughness testing for advanced technical ceramics: internationally agreed good practice*. Adv Appl Ceram **105** (2006) 88-98.

Chapter 3 Glass-like thermal conductivities in $(La_{1-x_1}Y_{x_1})_2(Zr_{1-x_2}Y_{x_2})_2O_{7-x_2}$ ($x = x_1+x_2$, $0 \leq x \leq 1.0$) Solid Solutions

3.1 Introduction

Lanthanum zirconate ($La_2Zr_2O_7$) with a pyrochlore structure has been proposed as a promising candidate material for the next generation thermal barrier coating (TBC) topcoats due to its low thermal conductivity and excellent high-temperature stability [1, 2]. Low thermal conductivity has a role in improving TBC durability [3], hence there is a great motivation to seek novel materials based on $La_2Zr_2O_7$ with the lowest possible thermal conductivity. To decrease the thermal conductivity of $La_2Zr_2O_7$, trivalent rare-earth cations are doped to occupy the La sites (A-site in the pyrochlore structure) to form $(La_{1-x}R_x)_2Zr_2O_7$ (R = Gd [4-7], Yb [4, 8], Nd [6], Eu [6], Dy [6]). The reduced thermal conductivity is mainly attributed to phonon-point defect scattering, which originates from the mass disorder and the ionic size difference between the dopant and the host ions [9]. Point defects are effective in scattering the high frequency phonons.

Recently, it has been proposed that the rare earth cations weakly bound in an oversized (usually clathrate-like) atomic cage ‘rattle’ and thus strongly scatter low-frequency phonons [10-13]. In the pyrochlore structure, the rattling effect has been reported by Wan et al [8] in $(Yb_{1/6}La_{5/6})_2Zr_2O_7$, in which a glasslike thermal conductivity is observed. The heavier and smaller Yb^{3+} ions rattle in the lattice, as indicated by anomalously large atomic displacement parameters (ADPs) obtained from the x-ray diffraction patterns. The rattling effect suggests a new mechanism that can be exploited to obtain lower thermal conductivity in the pyrochlore structure compared with the conventional phonon-point defect scattering mechanism.

Yttrium doped lanthanum zirconate (Y-$La_2Zr_2O_7$) is a material that attracts our interest due to the following reasons. Firstly, from the practical TBC application point of view, yttrium is a relatively light element, which is beneficial for the weight reduction of TBCs. It is also reported that yttrium can improve the chemical homogeneity of $La_2Zr_2O_7$ coatings deposited by the electron beam physical vapor deposition (EBPVD) technique[14]. Secondly, there are multiple sites that the yttrium ions (Y^{3+}) may occupy in $La_2Zr_2O_7$: Y^{3+} can replace La^{3+}[15, 16], or Zr^{4+} [17] or both [18]. These different occupation sites provide different possible sources of phonon scattering, for example, the mass and ionic size differences between Y^{3+} and La^{3+} and/or Zr^{4+}, the additional oxygen vacancies generated to balance the charge deficit caused by the possible substitution of Zr^{4+} by Y^{3+}, and the possible existence of the rattling effect due to the replacement of La^{3+} by the smaller Y^{3+}, etc. The mechanism(s) of the reduction of thermal conductivity of $La_2Zr_2O_7$ by yttrium doping is thus a topic of fundamental importance.

Therefore in this chapter, the thermal conductivities of Y-$La_2Zr_2O_7$ solid solutions have been investigated. A temperature-independent low thermal conductivity has been observed in Y-$La_2Zr_2O_7$ solid solutions within a certain composition range. The contributions from phonon-point defect scattering and resonant phonon scattering (rattling effect) have been separated using evidence about which sites the Y^{3+} ions occupy within the $La_2Zr_2O_7$ lattice. The results highlight the effectiveness of rattling effect in reducing the thermal conductivity of oxides with pyrochlore structure.

3.2 Experiments

The samples were synthesized by a coprecipitation-calcination method. Lanthanum nitrate hexahydrate (Sigma Aldrich, UK, 99.0%), zirconium oxynitrate hydrate (Sigma Aldrich, UK, 99.0%) and yttrium nitrate hexahydrate (Sigma Aldrich, UK, 99.8%) were used as starting materials. Appropriate amounts of each nitrate salt were weighed and dissolved in distilled water. The mixture was magnetically stirred for 24 hours to achieve a homogenous solution, which was added dropwise into a slight excess of aqueous ammonia solution (2 mol/L) to ensure complete precipitation of all the cations as hydroxides. The precipitate was filtered, washed with distilled water and ethanol and dried in air for 24 hours. The dried powder was calcined at 1473K for 12 hours. The obtained product was subsequently manually milled by mortar and pestle for half an hour, attrition milled (400 rpm) in distilled water for 12 hours and then subjected to freeze-drying to obtain the final powder with the designed composition. The final powder was cold-pressed into tablets under a uniaxial pressure of 100 MPa and then sintered at 1873K in air for 2 hours.

The phase compositions of the sintered pellets were identified by x-ray diffraction (XRD, Philips X'Pert) with Cu Kα radiation. The lattice parameters were calculated from fine scan XRD patterns (from 5^o to 120^o, 0.05^o per step, $0.003^o s^{-1}$) of the corresponding powders. The phases were further identified using a Raman optical microprobe system (Renishaw 1000, UK) .The spectra were excited with the 514 nm line of an argon laser, and collected across the wave numbers from 100 to 1000 cm^{-1}. Densities of the sintered specimens were measured by Achimedes' method. The speed of sound in each of the solid solutions, used for discussion of temperature dependence of *k*, was estimated from Young's moduli of the samples, which were measured by micro-indentation (MHTX CSM Inc. Switzerland).

The thermal diffusivities of the solid solutions were measured by a laser flash system (Built in-house, Manchester, UK) from room temperature up to 1173K in an argon atmosphere. The specimens were in the form of disks, 1.2 mm in thickness and 11 mm in diameter. Both surfaces were coated with a thin layer of carbon using colloidal graphite (Agar Scientific Ltd., UK) to ensure complete and uniform absorption of the laser pulse. During the measurements, the front face of samples was subjected to a short-duration heat pulse which was supplied by a neodymium-glass laser of 0.67 ms pulse duration. A liquid nitrogen cooled InSb infra-red detector was used to measure the temperature rise on the rear face of the samples. Measurements were made at various chosen temperatures during the heating procedure. For each temperature, fifteen measurements were made to obtain the mean value of the thermal diffusivity.

The specific heat capacitances of the solid solutions at various temperatures were calculated according to the Neumann-Kopp rule based on the reference specific heat values[19] of La_2O_3, ZrO_2 and Y_2O_3, as listed in Table 3.1. The calculated specific heat of $La_2Zr_2O_7$ is in agreement with the value reported in Ref.[20], indicating the validity of the Neumann-Kopp rule in the pyrochlores.

Thermal conductivities (k) of the solid solutions were obtained from the density (ρ), specific heat (C_p) and thermal diffusivity (D) using the relationship:

$$k = \rho \cdot C_p \cdot D \tag{3.1}$$

Table 3.1
The specific heat capacities for La_2O_3, Y_2O_3, ZrO_2 extracted from Ref.[19] and the calculated ones for Y-$La_2Zr_2O_7$ solid solutions based on Neumann-Kopp rule at various temperatures.

T (K)	Specific heat capacity ($J\ g^{-1}\ K^{-1}$)														
	La_2O_3	Y_2O_3	ZrO_2	x in $(La_{1-x_1}Y_{x_1})_2(Zr_{1-x_2}Y_{x_2})_2O_{7-x_2}$ ($x=x_1+x_2$)											
				0	0.05	0.1	0.15	0.2	0.25	0.3	0.4	0.5	0.7	0.9	1.0
463	0.366	0.515	0.539	0.440	0.444	0.448	0.451	0.454	0.456	0.457	0.459	0.467	0.491	0.517	0.528
553	0.377	0.532	0.563	0.457	0.461	0.465	0.469	0.471	0.474	0.475	0.476	0.485	0.511	0.538	0.548
653	0.387	0.543	0.580	0.470	0.474	0.478	0.482	0.484	0.487	0.488	0.489	0.498	0.524	0.552	0.563
843	0.400	0.554	0.600	0.486	0.490	0.494	0.498	0.500	0.503	0.504	0.505	0.514	0.540	0.567	0.578
943	0.405	0.559	0.610	0.493	0.497	0.501	0.505	0.507	0.510	0.511	0.511	0.520	0.547	0.574	0.585
1033	0.409	0.563	0.619	0.499	0.503	0.507	0.511	0.513	0.516	0.517	0.517	0.527	0.553	0.581	0.592
1133	0.413	0.569	0.630	0.507	0.511	0.515	0.519	0.521	0.524	0.525	0.525	0.534	0.561	0.590	0.601

3.3 Results

3.3.1 Phase composition

Fig.3.1 (a) shows the x-ray diffraction patterns of the solid solutions. The pure $La_2Zr_2O_7$ ($x = 0$) is single phase with pyrochlore structure (P), as indicated by the presence of the small superstructure reflections of (311) and (511) due to cation ordering. The single pyrochlore phase can be maintained in the solid solutions with x up to ~ 0.40, which is consistent with the results in Ref.[18]. Further increases in x lead to the formation of the fluorite phase (F), thus the solid solutions consist of two phases (P + F) across the composition range of $0.4 \leq x \leq 0.7$, and they become single fluorite phase when $0.9 \leq x \leq 1.0$.

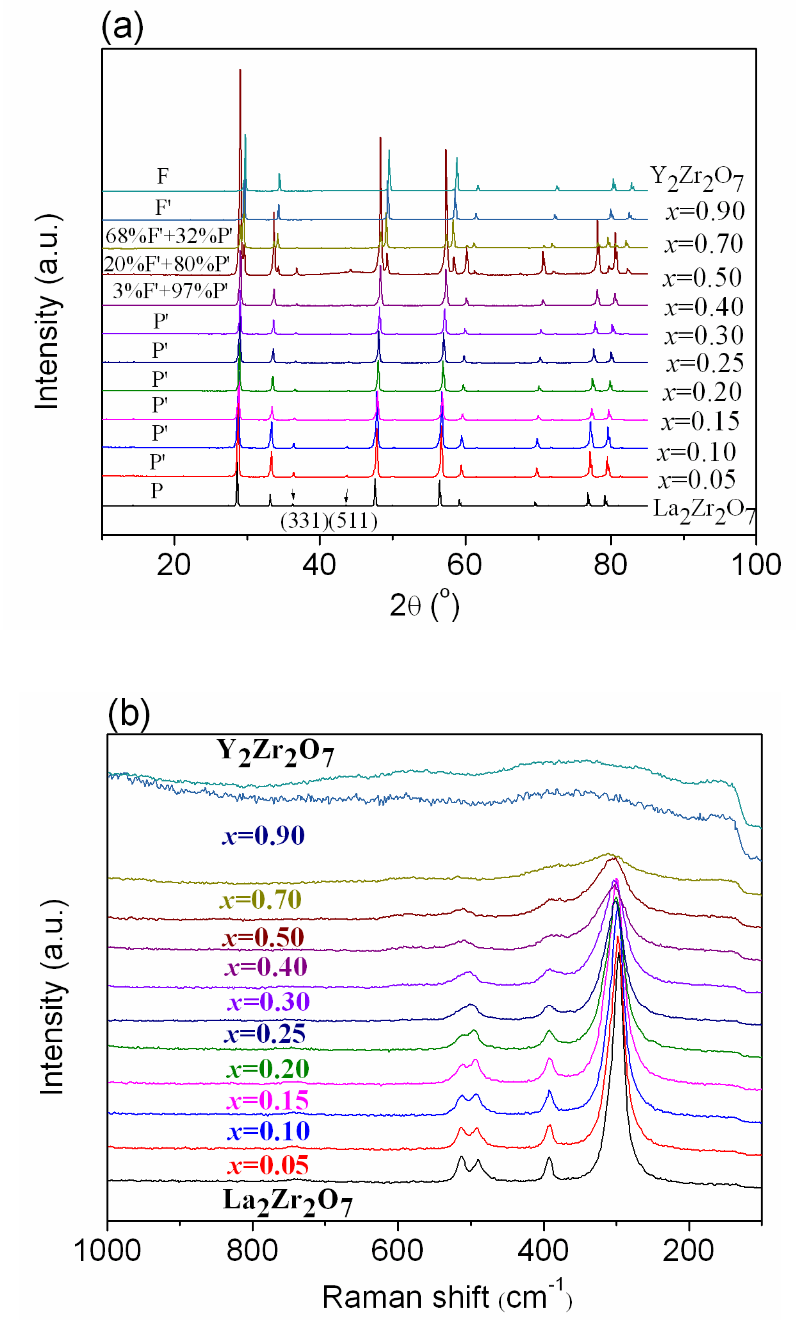

Fig.3.1 (a) X-ray diffraction patterns and (b) Raman spectra of Y-$La_2Zr_2O_7$ solid solutions. The mass fraction of two-phase mixtures ($0.4 \leq x \leq 0.7$) is calculated from the peak intensity and linear absorption coefficient of each phase.

The phase compositions of the solid solutions are also indentified by Raman spectroscopy, as shown in Fig.3.1(b). It can be observed that $La_2Zr_2O_7$ ($x = 0$) has four well-resolved Raman bands, which are typical for pyrochlore structures. In contrast, the Raman spectroscopy of $Y_2Zr_2O_7$ (x = 1.0) shows an absence of distinct Raman bands, which is due to the totally random distribution of oxygen vacancies in the defect fluorite structure. The Raman spectra in Fig.3.1(b) confirm the XRD result that a pyrochlore-fluorite transition occurs in the solid solutions with increasing x.

3.3.2 Lattice parameter

Fig.3.2 shows the lattice parameters of Y-$La_2Zr_2O_7$ solid solutions. It can be seen that when $x \leq 0.15$, the experimental values are in agreement with the theoretical ones calculated by assuming solely A-site substitution based on Vegard’s law. However, with further increase in x ($0.2 \leq x \leq 0.7$), the lattice parameter for the pyrochlore phase deviates from the theoretical value. Since the theoretical lattice parameter is calculated based on the assumption that Y^{3+} ions solely substitute La^{3+} ions (the A-site in the pyrochlore structure), the difference between the experimental and the theoretical values suggests a different position of the Y^{3+} ions in the pyrochlore structure, which will be discussed in detail in Section 3.4.1. On the other hand, the lattice parameters for the fluorite phase are consistent with the theoretical values.

3.3.3 Density

The measured and the theoretical densities (assuming only Y^{3+}, La^{3+} inter-substitution: $(La_{1-x}Y_x)_2Zr_2O_7$) of the solid solutions are listed in Table 3.2. It can be seen that within the composition range of $0.2 \leq x \leq 0.7$, the measured densities are higher than the theoretical values. This also indicates that the assumption that Y^{3+} only substitutes the La^{3+} ions is false. Based on the discrepancies of these two density values, the proportion of Y^{3+} substituting Zr^{4+} can be estimated (last column of Table 3.2) as presented in Section 3.4.1.

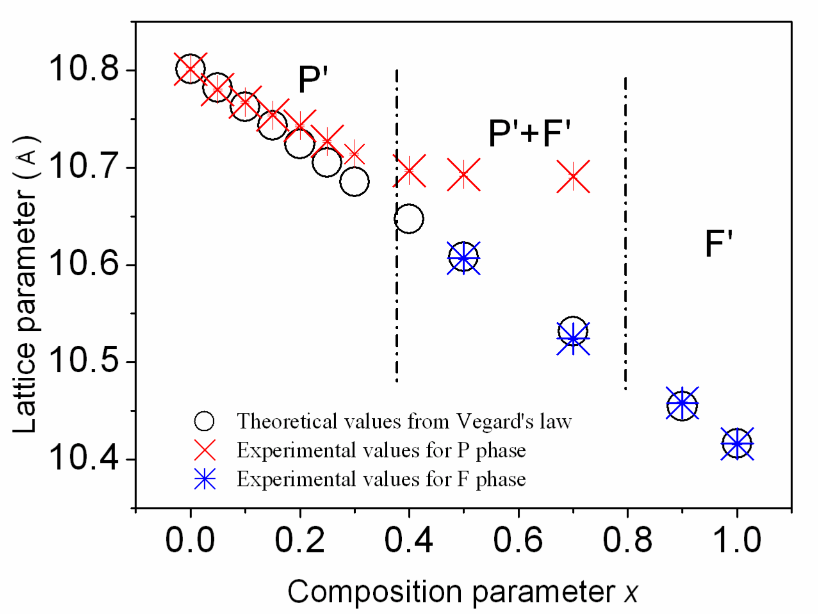

Fig.3.2 Lattice parameters of Y-$La_2Zr_2O_7$ solid solutions. The red crosses (for pyrochlore phase) and the blue symbols (for fluorite phase) are the experimental values obtained from the XRD patterns. The black hollow circles represent the theoretical values calculated from the Vegard's law, assuming that the smaller Y^{3+} ions (1.019Å, VIII coordinated) solely substitute La^{3+} ions (1.16Å, VIII coordinated). In highly doped pyrochlore range, the discrepancies indicate bigger Y^{3+} ions (0.90Å, VI coordinated) begin to occupy Zr^{4+} ions (0.72Å, VI coordinated).

Table 3.2

Densities and proposed formulae of Y-$La_2Zr_2O_7$ solid solutions. The theoretical densities are calculated based on the assumption that the substitution only occurs between Y^{3+} and La^{3+}. A higher measured density than the theoretical density suggests the possible Y^{3+}, Zr^{4+} inter-substitution in pyrochlores.

x	Theoretical density (g/cm^3)	Archimedes' density (g/cm^3)	formulae
0	6.040	6.040 ± 0.020	$La_2Zr_2O_7$
0.05	6.016	6.010 ± 0.010	$(La_{0.95}Y_{0.05})_2Zr_2O_7$
0.10	5.984	5.980 ± 0.020	$(La_{0.90}Y_{0.10})_2Zr_2O_7$
0.15	5.952	5.940 ± 0.020	$(La_{0.85}Y_{0.15})_2Zr_2O_7$
0.20	5.931	5.934 ± 0.006	$(La_{0.82}Y_{0.18})_2(Zr_{0.98}Y_{0.02})_2O_{6.98}$
0.25	5.904	5.914 ± 0.010	$(La_{0.78}Y_{0.22})_2(Zr_{0.97}Y_{0.03})_2O_{6.97}$
0.30	5.878	5.912 ± 0.007	$(La_{0.76}Y_{0.24})_2(Zr_{0.94}Y_{0.06})_2O_{6.94}$
0.40	5.823	5.898 ± 0.008	$(La_{0.74}Y_{0.26})_2(Zr_{0.86}Y_{0.14})_2O_{6.86}$
0.50	5.791	5.844 ± 0.009	/
0.70	5.694	5.706 ± 0.009	/
0.90	5.601	5.600 ± 0.005	$(La_{0.10}Y_{0.90})_2Zr_2O_7$
1.00	5.552	5.550 ± 0.010	$Y_2Zr_2O_7$

3.3.4 Thermal diffusivity/conductivity

Fig.3.3 (a) and (b) show the thermal diffusivities and the thermal conductivities of the solid solutions at various temperatures, respectively. The thermal diffusivity and the thermal conductivity have similar composition dependence: they both initially decrease with increased *x*, reach their lowest values at $x = 0.5$, and then rise with further increases of *x*. Another marked feature in Fig.3.3 (b) is that within the composition range of $0.20 \leq x < 0.50$ (as indicated in the dashed rectangle), the thermal conductivity exhibits a temperature-independent behaviour. These thermal conductivity data display two significant effects. First, the introduction of Y^{3+} into $La_2Zr_2O_7$ and the introduction of La^{3+} into $Y_2Zr_2O_7$ can both effectively decrease the thermal conductivity of the end members. Second, the introduction of Y^{3+} into $La_2Zr_2O_7$ remarkably changes the thermal conductivity-temperature (*k*-T) relationship, however this effect is not as significant when La^{3+} is introduced into $Y_2Zr_2O_7$.

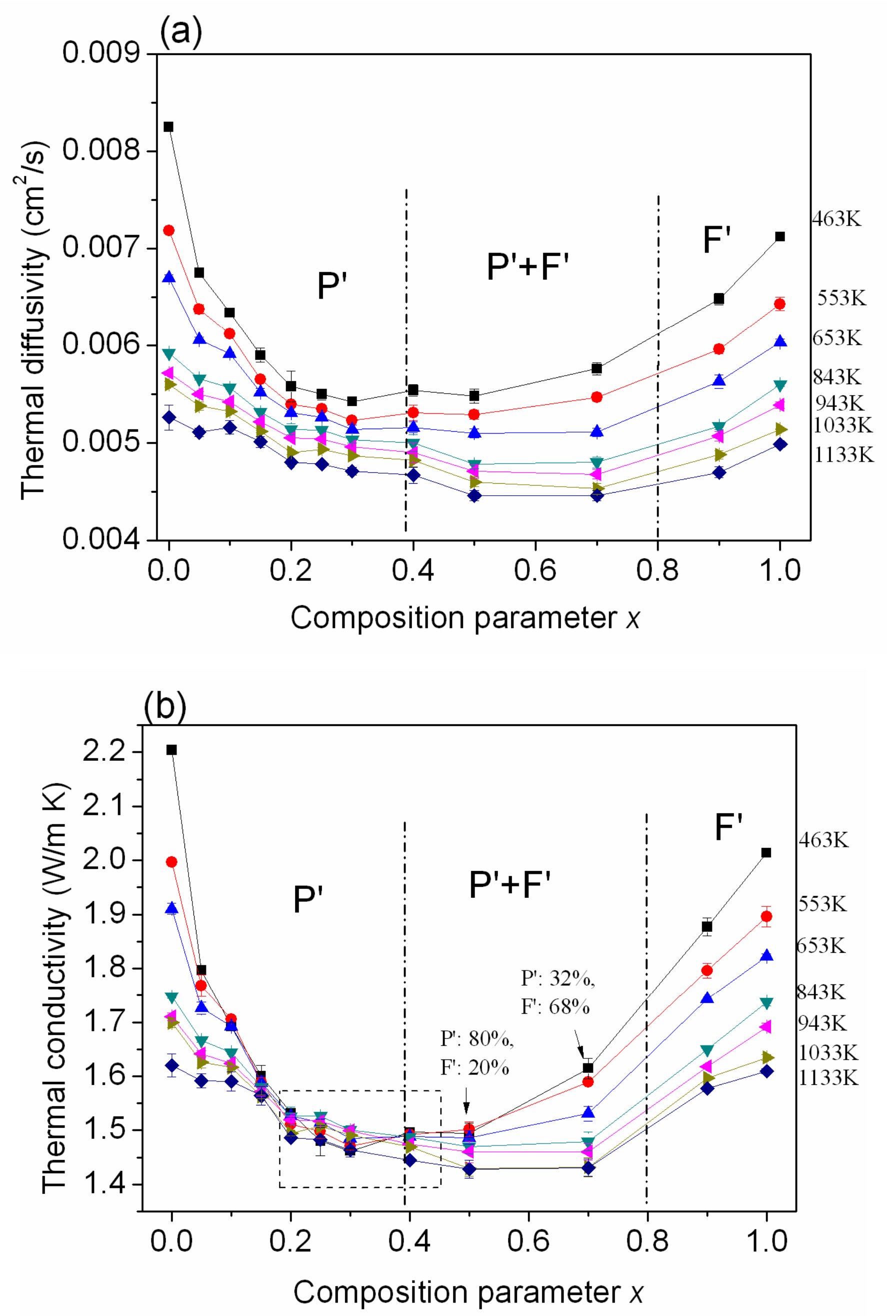

Fig.3.3 (a) Thermal diffusivities and (b) thermal conductivities of Y-$La_2Zr_2O_7$ solid solutions measured from 463 to 1133 K.

3.4 Discussions

The major finding of this chapter is that doping Y^{3+} into $La_2Zr_2O_7$ not only decreases the thermal conductivity but also changes the temperature dependence of the thermal conductivity. A glass-like thermal conductivity, which nearly reaches the amorphous limit calculated from Cahill's model [21], has been observed within the composition range of $0.20 \leq x < 0.40$. The main purpose of this discussion is to consider the possible mechanisms behind the temperature-independent thermal conductivity due to the Y^{3+} doping. It should be noted that SEM observation shows that the samples are almost fully dense and that the average grain sizes of the samples are larger than 1 μm, which is much larger than the phonon mean free path of $La_2Zr_2O_7$ (about 10 nm). Therefore, the porosity and the grain boundary have minimal effects on the thermal conductivity and can be eliminated from our discussions.

3.4.1 Extra oxygen vacancies due to Y^{3+}, Zr^{4+} inter-substitution

The occupation site(s) of Y^{3+} in $La_2Zr_2O_7$ is an issue which remains controversial in the literature. The studies by Whittle et al [15] and Ota et al [16] conclude that the substitution only occurs between the Y^{3+} and the La^{3+} ions at the A-site due to Y^{3+} and La^{3+} being isovalent. By contrast, Speakman et al [17] initially presumed that Y^{3+} only substituted Zr^{4+} ions (B-site) but concluded that it could replace both La^{3+} (A-site) and Zr^{4+} (B-site) ions, which was consistent with the conclusion reached by Fabrichnaya et al [18]. Based on lattice parameters and density measurements, we suggest that Y^{3+} solely replaces La^{3+} on the A-site when x is below a critical value, above which it substitutes both La^{3+} and Zr^{4+} ions. We justify this conclusion in the following paragraphs.

(1) Lattice parameter

In Fig.3.2, the lattice parameter decreases with increasing x, indicating that substitution between Y^{3+} (1.019Å, VIII coordinated)[22] and La^{3+} (1.16Å, VIII coordinated)[22] dominates. When $x < 0.15$, the experimental lattice parameters agrees well with the values expected from Vegard's law, indicating that Y^{3+} ions occupy the La^{3+} sites in the pyrochlore structure. However, within the composition range of $0.2 \leq x < 0.4$ (over which a single pyrochlore phase is maintained) the lattice parameters are higher than those calculated by assuming the replacement of La^{3+} with Y^{3+}, suggesting that substitution between Y^{3+} (0.90 Å, VI coordinated)[22] and Zr^{4+} (0.72 Å, VI coordinated)[22] also occurs.

(2) Density

As stated in Section 3.3.3, when $0.2 \leq x < 0.4$ (in the following discussion we focus on the single pyrochlore phase region), the measured densities are consistently higher than the calculated values assuming merely Y^{3+}, La^{3+} inter-substitution (Table 3.2). This discrepancy indicates the invalidity of that assumption, i.e. Y^{3+}, Zr^{4+} inter-substitution also occurs. Therefore, solid solutions can be formulated as $(La_{1-x_1}Y_{x_1})_2(Zr_{1-x_2}Y_{x_2})_2O_{7-x_2}$ ($x = x_1 + x_2$). The real theoretical densities (ρ_{real}) of the solid solutions can be calculated by: $\rho_{real} = 8(572.26 - 100.008x + 79.373x_2)/(N_A(a_1)^3)$, where N_A is Avogadro's constant and a_1 is the lattice parameter obtained from XRD. Since all samples are almost fully dense, using

Archimedes' density as ρ_{real}, x_2 and thus the formula for each composition can be obtained, as listed in Table 3.2.

To sum up, when $x \leq 0.15$, Y^{3+} ions solely occupy the A-site in host pyrochlore lattice; when $x \geq 0.20$, the majority of Y^{3+} ions substitute the La^{3+} sites whereas a small amount of Y^{3+} ions occupy Zr^{4+} sites and create additional oxygen vacancies. Based on this information, we discuss the *k* of the solid solutions with a focus on the temperature effect in the following section.

3.4.2 Resonant phonon scattering in Y-$La_2Zr_2O_7$ pyrochlore solid solutions

3.4.2.1 Fitting of thermal conductivity- temperature (*k*-T) curves

Fig.3.4 indicates that the introduction of smaller Y^{3+} cations into $La_2Zr_2O_7$ lattice dramatically changes the temperature dependence of *k*, suggesting that strong phonon scattering source is present. However, we cannot ascribe this to oxygen vacancies (like in yttria-stabilized zirconia (YSZ)[23]) for two reasons. Firstly, there are no additional oxygen vacancies in $(La_{1-x}Y_x)Zr_2O_7$ when $x \leq 0.15$. Secondly, oxygen vacancy concentration due to Y^{3+}, Zr^{4+} inter-substitution ($x \geq 0.2$) is much lower than that in YSZ, as a comparison, the oxygen vacancy concentration[*] for $(La_{0.76}Y_{0.24})_2(Zr_{0.94}Y_{0.06})_2O_{6.94}$ ($x = 0.3$) is 0.005 whilst for 12 mol% Y_2O_3 stabilized zirconia (the composition at which glassy *k* becomes apparent[23]) the concentration is much greater at 0.04. The normal

---

[*] Oxygen vacancy concentration $[V_O]$ in this thesis is defined as the ratio of all oxygen vacancies present divided by all atomic sites in the lattice.

point defect–phonon scattering mechanism fails to explain the presence of strong phonon scattering source in Y^{3+}-doped $La_2Zr_2O_7$ pyrochlore solid solutions.

For solid solutions containing point defects (substitutional defects or vacancies), phonons interact with the defects and reduce the thermal conductivity, and the *k*-T relation can be expressed as[24, 25]:

$$k_{U+P} = \frac{A}{T}\frac{\omega_0}{\omega_D}\arctan(\frac{\omega_1}{\omega_0}) + \frac{A}{3T}\frac{1}{1+(\omega_1/\omega_0)^2}[(\frac{\omega_D}{\omega_1})^2 - \frac{\omega_1}{\omega_D}] \quad , \tag{3.2}$$

in which ω_0, ω_1 are expressed as:

$$\omega_0 = \sqrt{\frac{D_P T}{D_U c_P}}\,, \tag{3.3a}$$

$$\omega_1 = \omega_0\sqrt{-0.5 + \sqrt{0.25 + (\omega'/\omega_0)^2}} \tag{3.3b}$$

where ω’ is defined by $\Lambda_U(\omega') = \Lambda_{\min}$, and $\omega' = \sqrt{\frac{D_U}{\Lambda_{\min} T}}$.

(3.3c)

By incorporating Eq.(3.3), Eq.(3.2) can be re-written as:

$$k_{U+P} = \frac{A}{3T_1} + \frac{A}{T^{0.5}}\frac{2}{\sqrt{\alpha}}\arctan\sqrt{-\frac{1}{2} + \frac{1}{2}\sqrt{1+\alpha\frac{T_1}{T^2}}} - \frac{2\sqrt{2}}{3}\frac{A\sqrt{T_1}}{T^{1.5}}\frac{1}{(1+\sqrt{1+\alpha\frac{T_1}{T^2}})^{1.5}} \tag{3.4a}$$

where $\alpha = \frac{4c_P\omega_D^2 D_U}{D_P} = \frac{\sqrt{2}}{4\pi^2}\frac{c_P\Omega_0\overline{M}\omega_D^2\Gamma}{k_B a\gamma^2} = 0.544\frac{c_P N\overline{M}v^2\Gamma}{k_B\gamma^2}$ [26-30], (3.4b)

In the above expressions, D_P and D_U are temperature-independent parameters related to the phonon-point defect scattering and phonon-phonon Umklapp scattering, respectively; c_P is the point defect concentration, defined as the ratio of the total number of point defects to total number of atomic sites; Λ_{min} is the minimum mean free path of phonons; T_1 is a characteristic temperature, defined as $D_U/(\Lambda_{min}(\omega_D)^2)$ [24]; A and α are fitting parameters; ω_D is the Debye frequency; γ is the Grüneisen constant; $\overline{M}$ is the mean atomic mass; Ω_0 is the volume of a unit cell; a^3 is the average atomic volume; N is the number of atoms per unit cell ($\Omega_0=Na^3$); v is the mean speed of sound; and Γ is the scattering coefficient.

Since α=0 for end members ($La_2Zr_2O_7$ and $Y_2Zr_2O_7$), Eq.(3.4a) simplifies to $k_U=A/(3T_1)+2A(T_1)^{0.5}/(3T^{1.5})$. Therefore, for end members, A and T_1 are used as fitting parameters. By contrast, for solid solutions, A and α are used as the adjustable parameters (see Table 3.3). The fitting curves are shown in Fig.3.4 (a) and (b), and the parameters A and α are obtained and listed in Table 3.3. An insight into the *k*-T curves in

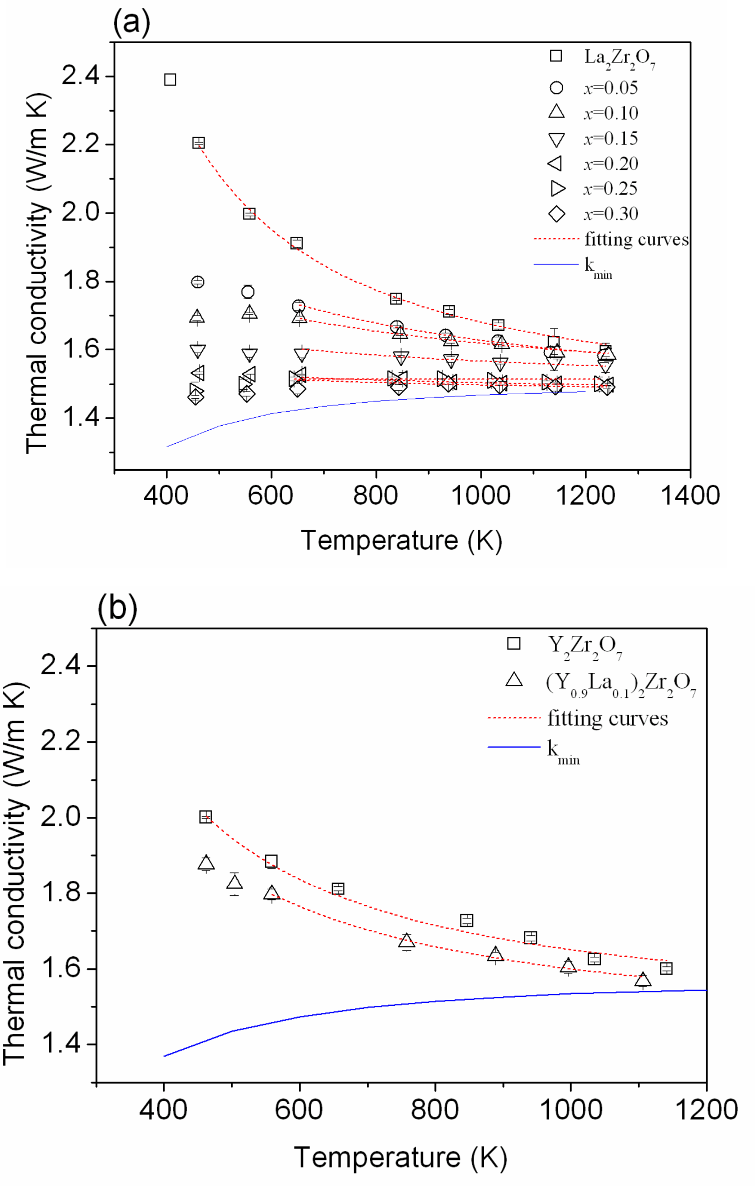

Fig.3.4 Thermal conductivity as a function of temperature: (a) samples with single pyrochlore phase and (b) samples with single defect fluorite phase. The dashed red lines are fitting curves based on Eq.(3.4). Since the precondition for Eq.(3.4) is $T > \Theta_D$ (Debye temperature), the k-T curves are fitted above Θ_D. The solid blue line is the minimal thermal conductivity (k_{min}) of amorphous $La_2Zr_2O_7$ and $Y_2Zr_2O_7$ calculated from Cahill's model [21].

Table 3.3

Basic parameters used for calculation and fitting results of the $(La_{1-x}Y_{x_1})_2(Zr_{1-x_2}Y_{x_2})_2O_{7-x_2}$ $(x = x_1 + x_2,\ 0 \le x \le 1)$ solid solutions with single phase.

x	Lattice parameter (Å)	a^3, atomic volume (10^{-29} m^3) [a]	a (Å)	c_P [b]	ρ (10^3 kg·m^{-3})	$\overline{M}$ (10^{-26} kg)	E (GPa)	v (m/s)	ω_D (10^{13} Hz) [f]	Θ_D (K) [g]	γ	Λ_{min} (Å)	T_1 (K)	A (W/m)	α
0	10.801	1.432	2.428	0	6.033	8.642	180 [c] 175 [d]	4752 [e]	7.633	583	2.07 [h]	3.135 [j]	189 [l]	818 [l]	/
0.05	10.780	1.424	2.424	0.0083	6.015	8.563	190 [c]	4890 [e]	7.868	601	2.07 [h]	3.135 [j]	198 [m]	857 [l]	19822 [l]
0.10	10.767	1.418	2.421	0.0167	5.984	8.488	199 [c]	5017 [e]	8.082	617	2.07 [h]	3.135 [j]	206 [m]	905 [l]	72734 [l]
0.15	10.754	1.413	2.418	0.025	5.952	8.412	205 [c]	5106 [e]	8.235	629	2.07 [h]	3.135 [j]	211.5 [m]	933 [l]	244200 [l]
0.20	10.743	1.412	2.417	0.035	5.934	8.374	200 [c]	5051 [e]	8.150	622	2.07 [h]	3.135 [j]	206 [m]	899 [l]	464900 [l]
0.25	10.727	1.406	2.414	0.0442	5.914	8.318	197 [c]	5021 [e]	8.112	619	2.07 [h]	3.135 [j]	202 [m]	918 [l]	1280000 [l]
0.30	10.714	1.405	2.413	0.055	5.912	8.303	194 [c]	4984 [e]	8.055	615	2.07 [h]	3.135 [j]	198.5 [m]	870 [l]	2110000 [l]
0.90	5.225	1.297	2.349	0.0167	5.601	7.280	160 [c]	4650 [e]	7.716	589	2.08 [i]	3.014 [k]	152 [m]	656 [l]	800 [l]
1.0	5.208	1.284	2.342	0	5.552	7.129	155 [c]	4597 [e]	7.655	584	2.08 [i]	3.014 [k]	145 [l]	650 [l]	/

[a] average atomic volume, calculated by $\overline{M}/\rho$, or Ω_0/N. [h] the overall defect concentration. [c] Young's modulus measured in this study. [d] Ref.[1].

[e] average sound speed, calculated by $v=0.87(E/\rho)^{0.5}$[25]. [f] Debye frequency, calculated by $\omega_D=(6\pi^2)^{1/3}v/a$ [30].

[g] Debye temperature, calculated by $\Theta_D=\hbar\,\omega_D/k_B$ [30].

[h] Grüneisen parameter in pyrochlore structure, calculated from $\gamma = \left(\frac{Ma\omega_D^2}{2661.8A}\right)^{0.5}$[26,27,29]based on the fitted A of $La_2Zr_2O_7$, assumed constant for all Y^{3+} doped $La_2Zr_2O_7$ pyrochlore; [i] corresponding value for defect fluorite structure.

[j] Minimum phonon mean free path (inter-atomic spacing) in pyrochlore structure, calculated from $\Lambda_{min} - \frac{D_U}{T_1\omega_D^2}$[24]based on the fitted T_1 of $La_2Zr_2O_7$, where $D_U = \frac{\sqrt{2}}{4\pi}\left(\frac{v^2}{a}\right)\left(\frac{\overline{M}v^2}{\gamma^2 k_B}\right)$[26,27], assumed constant for all Y^{3+} doped $La_2Zr_2O_7$ pyrochlore; [k] corresponding value for fluorite.

[l] fitted results. For end members ($La_2Zr_2O_7$, $Y_2Zr_2O_7$), A and T_1 obtained by fitting; for solid solutions with point defects, A and α obtained by fitting whereas [m] T_1 calculated by $T_1 = 0.0074\frac{\overline{M}av^2}{k_B\gamma^2\Lambda_{min}}$.[24,26,27,29]

Fig.3.4 and the fitting results in Table 3.3 leads to the following information. (1) The parameter α describes the temperature dependence of k. A very large value of α indicates a flat k-T curve and thus a temperature-insensitive k; (2) The high-temperature plateau value on the k-T curve is determined by $A/3T_1$ (Eq.(3.4a) when T approaches infinity), which reflects an intrinsic property of a material, in the form of:

$$\frac{A}{3T_1}=\frac{1}{3}\frac{3k_B}{a^3}v\Lambda_{\min}=\frac{1}{3}\frac{3k_B}{a^3}va_0 \tag{3.5}$$

where a_0 is inter-atomic spacing. This suggests that high-temperature plateau k is dominated by the phonons with a mean free path of inter-atomic spacing[25]. Once α and $A/3T_1$ are known, the k-T relationship is established.

According to Eq.(3.4b), parameter α (temperature-insensitive indicator of k) is directly related to the scattering coefficient Γ. Given that the Y^{3+} occupation site(s) are known, as discussed in Section 3.4.1, according to Slack[31] (for different atomic sites in lattice) and Abeles[9] (for each atomic site), Γ can be given as:

$$\Gamma=\Sigma x_i[(\Delta M_i/M)^2+\varepsilon(\Delta\delta_i/\delta)^2] \tag{3.6}$$

where x_i, M_i, δ_i are concentration, mass and ionic radius for dopant i, $M=\Sigma x_iM_i$, $\delta=\Sigma x_i\delta_i$, $\Delta M_i=M_i-M$, $\Delta\delta_i=\delta_i-\delta$. This allows Γ to be calculated with only one unknown parameter ε (shown in Table 3.4). ε is a parameter describing the contributions from all the other factors other than the mass difference to the scattering coefficient. ε can be empirically estimated from the Grüneisen constant and the Poisson’s ratio[28, 32], which are less than 200 for typical ceramic materials [5, 9].

By combining α values shown in Table 3.3 (from fitting of *k*-T plots based on Eq.(3.4a)) and Γ expressions (Eq.(3.6)), the ε values can be obtained as shown in Table 3.4. Anomalously large ε values (one magnitude higher than the normal ones) are obtained for compositions $0.05 \leqslant x \leqslant 0.30$ (i.e. pyrochlore solid solutions). By contrast, for undoped $La_2Zr_2O_7$ and La^{3+}-doped $Y_2Zr_2O_7$ fluorite solid solutions, the fitting ε values are unequivocally within the normal range. The only explanation for this is that an extra unknown strong source of phonon scattering is merely present in Y-$La_2Zr_2O_7$ pyrochlore solid solutions.

Table 3.4
Scattering coefficient Γ and the parameter ε of Y-$La_2Zr_2O_7$ solid solutions with single phase (pyrochlore for $0 \le x \le 0.30$, fluorite for $x = 0.9$ and 1.0) based on the assumption that each atomic site has similar ε values.

x	Γ	ε
0	--	196
0.05	$8.86 \times 10^{-3} + 9.86 \times 10^{-4}$ ε	1444
0.10	$1.708 \times 10^{-2} + 1.86 \times 10^{-3}$ ε	1347
0.15	$2.464 \times 10^{-2} + 2.16 \times 10^{-3}$ ε	2097
0.20	$2.91 \times 10^{-2} + 4.00 \times 10^{-3}$ ε	1915
0.25	$3.441 \times 10^{-2} + 4.97 \times 10^{-3}$ ε	3429
0.30	$3.722 \times 10^{-2} + 6.58 \times 10^{-3}$ ε	3500
0.90	$2.322 \times 10^{-2} + 1.53 \times 10^{-3}$ ε	173
1.00	--	198

3.4.2.2 Presence of rattlers in pyrochlore lattice

We now know that strong phonon scatterers are strongly related to the specific crystalline structure of pyrochlore. Given the fact of the pyrochlore gradually transition to fluorite with an increase of *x* (composition parameter), these two structures are highly similar except for the following two distinctions: (1) as Raman spectra (Fig.3.1(b)) suggest, defective fluorite has disordered oxygen vacancies while pyrochlore has ordered ones; (2) the distinctive oversized oxygen cages (AO_8), as shown in Fig.3.5, are unique in the pyrochlore lattice, formed by the six 48f-site O1 relaxation towards the adjacent unoccupied 8b-site oxygen vacancy (Fig.3.5)[33, 34]. If the disordered oxygen vacancies were the reason, then the temperature insensitive *k* should emerge in fluorite solid solutions, since, as mentioned in Section 3.3.1, the disorder of oxygen vacancies in defective fluorite is at its extreme. Therefore, the unique oversized oxygen cages AO_8 in pyrochlore lattice must be the reason.

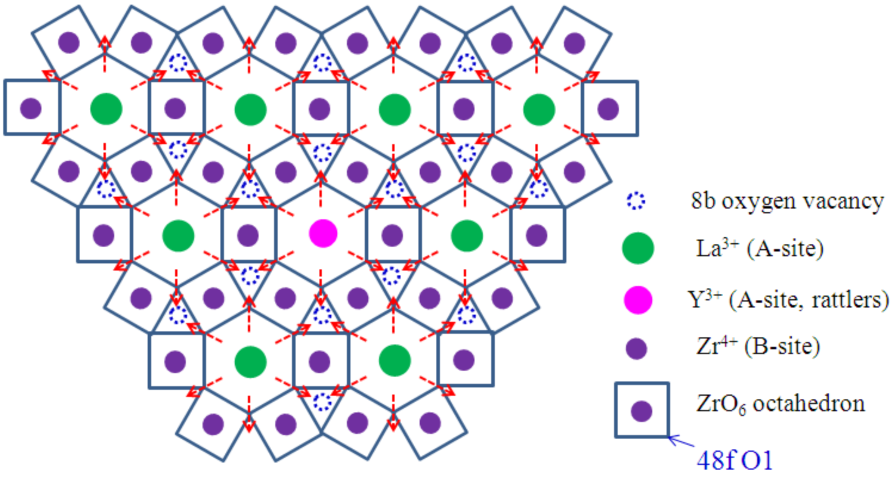

Fig.3.5 Schematic diagram of pyrochlore crystalline structure along (1 1 1) plane. The backbone of pyrochlore is the network of corner-sharing BO_6 octahedra (vertices of which are 48f-site O1). A^{3+} cations fill the interstices, coordinated with six 48f-site O1 and two 8a-site O2 (not shown). Since 48f-site O1 tends to relax towards the adjacent 8b-site vacancy (indicated as red arrows), the oxygen cages formed surrounding A^{3+} (AO_8) are oversized. With smaller Y^{3+} replacing La^{3+}, AO_8 cages become more spacious.

The idea that the oversized atomic cages are connected to strong phonon scattering sources is demonstrated by clathrate-like compounds such as YB_{66}[13, 35], $Al_{10}V$[36], and partially filled skutterudites[10, 11], in which the existence of incoherent, localized vibrations of rattlers significantly reduces lattice thermal conductivity. Among these compounds, there are two common characteristics of rattlers[11]: (1) guest atoms (or rattlers) occupy the oversized atomic cages formed by non-metallic host atoms; (2) guest atoms (or rattlers) are loosely bound to host atoms. For Y-$La_2Zr_2O_7$ pyrochlores, there is a loose oxygen coordination environment of interstice centre Y^{3+} cations (Fig.3.5) and Hess et al [37] have shown that the Y/La-O1 bond is greatly weakened. With smaller Y^{3+} cations occupying AO_8 cage centres, these AO_8 cages become more spacious for Y^{3+} to vibrate locally and independently (Fig.3.5), which leads to the strong incoherent scattering of the sound waves in all directions and thereby greatly impedes thermal transport.

The superiority of rattlers over point defects on suppressing *k* is illustrated in Fig.3.6. Based on the preceding Abeles model, *k* reduction attributed purely to rattlers can be successfully separated from point defect effects by assuming normal ε values (about 200). For comparison, two symmetrical compositions at each end member: $(La_{0.9}Y_{0.1})_2Zr_2O_7$ pyrochlore and $(La_{0.1}Y_{0.9})_2Zr_2O_7$ fluorite solid solutions, are considered. If there were not rattlers in the former, *k* reductions due to normal point defects of them should be similar, since they have similar scattering coefficient Γ. The gap (Fig.3.6(a), $(La_{0.9}Y_{0.1})_2Zr_2O_7$ pyrochlore) and overlap (Fig.3.6(b), $(La_{0.1}Y_{0.9})_2Zr_2O_7$ fluorite) of measured and calculated *k*-T curves unambiguously confirms the presence of rattlers in the Y^{3+}-doped $La_2Zr_2O_7$ pyrochlore solid solutions. As shown in Fig.3.6(a), the *k* reduction magnitude

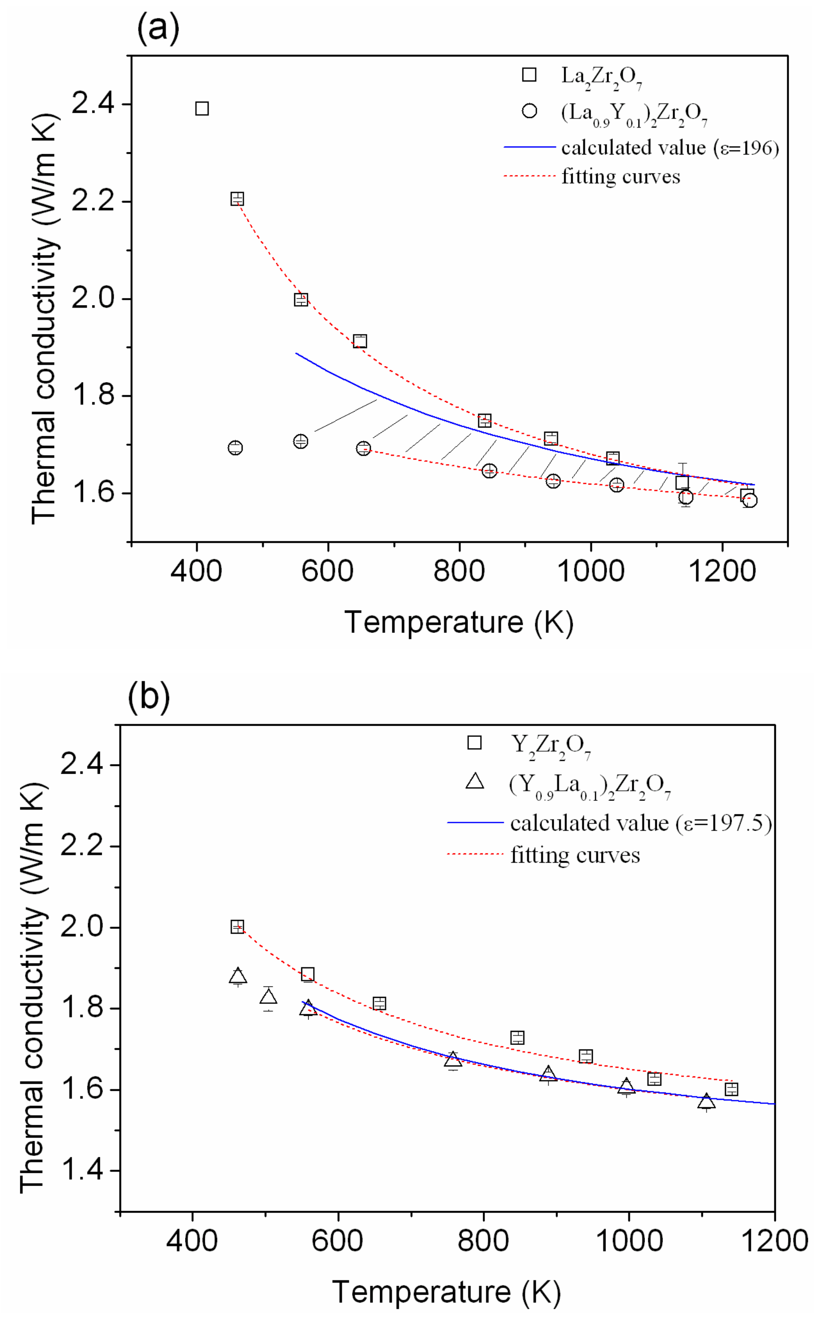

Fig.3.6 The measured and calculated (solid blue line, Abeles model: ε=196 for $La_2Zr_2O_7$ and ε=197.5 for $Y_2Zr_2O_7$) thermal conductivities of (a) $(La_{0.9}Y_{0.1})_2Zr_2O_7$ and (b) $(Y_{0.9}La_{0.1})_2Zr_2O_7$. The hatched area in (a) is the *k* reduction purely due to phonon-rattler (Y^{3+} ions in AO_8 cages) scattering. The perfect agreement of calculated and measured *k* in (b) signifies the lack of rattlers in defect fluorite structure.

due to the rattling effect (hatched area) is much bigger than that due to the point defect effect, signifying that rattlers are far more effective than normal point defects at impeding heat transport. In contrast to point defects, which are only effective in scattering high-frequency phonons ($\Lambda_D \propto \omega^{-4}$[24, 38]), rattlers are more efficient in scattering low-frequency phonons which contribute considerably to lattice thermal conductivity [11, 39]. Therefore, as a new decay channel for low-frequency phonons, the introduction of rattlers in lattice can reduce *k* significantly.

Taking rattlers as an individual phonon scattering source, the phonon mean free path (Λ) can be written as $\Lambda^{-1}=(\Lambda_U)^{-1}+(\Lambda_D)^{-1}+(\Lambda_{rattler})^{-1}$, where Λ_U, Λ_D, Λ_{rattle} denote phonon mean free path due to phonon-phonon Umklapp scattering, phonon-point defect scattering and phonon-rattler scattering, respectively. For a perfect dielectric lattice, the temperature-dependence of *k* mainly originates from the temperature- dependent Λ_U ($\propto \omega^{-2}T^{-1}$[24, 26], ω is phonon frequency). However, in analogy with Rayleigh scattering, it is well-established that Λ_D of point defects in the lattice is only proportional to ω^{-4} and thus Λ_D is irrelated to temperature[38]. That is the reason why the presence of point defects in the lattice can change *k*-T curves, mildly in the case of most of normal substitutional point defects, but dramatically for oxygen vacancies (a strong phonon scatterer), in some cases to the point of causing a temperature-insensitive *k* [23]. Similarly, Λ_{rattle} has been proposed as temperature-irrelated and can be written as $C((\omega_R)^2-\omega^2)^2/\omega^2$[40], where C is constant and ω_R is the resonant frequency. Clearly, rattlers can effectively scatter phonons with frequencies near ω_R, and therefore, they are strong phonon scatterers, as reported in Refs.[10-12]. Consequently, the overall phonon mean free path of Y-$La_2Zr_2O_7$ pyrochlores with the presence of rattlers is dictated by the temperature- insensitive $\Lambda_{rattler}$ term and thus overshadows the temperature- dependent Λ_U term. This is true for at least the low and intermediate temperature range.

The presence of adequate strong phonon scatterers (rattlers) in Y^{3+}-doped $La_2Zr_2O_7$ pyrochlore results in glasslike *k*, as shown in Fig.3.4(a), with the typical glassy feature that *k* lacks dependence on either temperature or defect concentration [23] (i.e. nearly overlapping *k*-T curves when $0.2 \leq x \leq 0.3$). The highly phonon scattering regime in crystalline solids with enough strong phonon scatterers present makes the heat transport behave like an amorphous glass, despite fundamentally different structures. These strong phonon scatterers, the presence of which can make a crystalline solid acquire glasslike lattice vibrations, are always connected to vacancies [21, 23], interstitials [21, 41], and rattlers [10, 13]. Instead of conventional phonon-gas model, Allen and co-workers developed a harmonic diffusion model, which is applicable to both glass and crystalline solids with strong scattering [42, 43]. In this model, the dominant mechanism for heat transport is the intrinsic harmonic diffusion of 'diffusons' (which occupy ~93% of vibrational modes and are neither localized nor propagating), and contributes to *k* an amount $C_i(T)D_i/V$ per mode *i*, where $C_i(T)/V$ is specific heat per unit volume and D_i is temperature-independent mode diffusivity ($D_i = va_0/3$, v: sound speed; a_0: inter-atomic spacing). Therefore, for crystalline solids with strong scattering, the temperature dependence of *k* is solely due to the temperature dependence of heat capacity. This can well explain the k-T curves for composition $0.2 \leq x \leq 0.3$, which exhibit firstly a smooth increase and then finally saturation at high temperatures, similar to the trend in heat capacity.

3.4.2.3 High-temperature plateau *k*

The high-temperature plateau k expression (Eq.(3.5), where $3k_B/a^3$ is specific heat per unit volume) is consistent with the harmonic diffusion model for all common dielectric materials, regardless of the presence or absence of strong phonon scatterers. This unambiguously signifies that, when temperature is adequately high, Y-$La_2Zr_2O_7$ (indeed all dielectric materials) can be treated as crystalline solids with strong scattering, with phonon-phonon Umklapp scattering itself as a highly phonon-scattering source. Since $\Lambda_U \propto \omega^{-2}T^{-1}$, with increasing temperature, Λ_U gradually becomes the dominant contributor to overall phonon mean free path Λ. This can explain the declining efficacy of point defects or rattlers to suppress k with increasing of temperature (Fig.3.6 (a)), indicating the weak impact of rattlers on this high-temperature plateau regime. The introduction of strong phonon scatterers (rattlers) only reduces the commencement temperature of glasslike heat transport behaviour in crystalline solids, and in some extreme cases (i.e. with adequately strong phonon scatterers present), the glassy heat transport in crystalline solids could possibly be found over the whole temperature range. By contrast, according to Eq.(3.5), the alternative way to reduce plateau k is to reduce sound velocity v, i.e. to reduce internal bonding strength to achieve lower elastic modulus E, which is probably related to strong anharmonicity of lattice (large Grüneisen parameter γ).

3.5 Conclusions

Dopant position and thermal conductivity of $(La_{1-x_1}Y_{x_1})_2(Zr_{1-x_2}Y_{x_2})_2O_{7-x_2}$ ($x=x_1+x_2$, $0 \le x \le 1$) solid solutions were thoroughly investigated in this study. The introduction of yttrium dopant drives the gradual order (pyrochlore) and disorder (defective fluorite) transition. It has been clarified that, within the pyrochlore range, a small amount of extra oxygen vacancies are produced when $x \geq 0.20$ due to Y^{3+} substituting Zr^{4+} on B-site. By fitting *k*-T curves, anomalously large ε values (one magnitude higher than normal) are found exceptionally in Y^{3+}-doped $La_2Zr_2O_7$ pyrochlore solid solutions. This provides solid evidence for the existence of a novel strong phonon scattering source, which is closely related to the specific crystalline structure of pyrochlore. It is revealed that the strong phonon scatterers are those smaller Y^{3+} cations (rattlers), which reside in the oversized oxygen AO_8 cages formed by the six O1 outward movements in pyrochlore structure. When adequate rattlers are present ($0.20 \le x < 0.40$), the crystalline pyrochlore solid solutions are so strongly scattering that they even acquire glasslike thermal behaviour. At adequately high temperature, the phonon-phonon Umklapp scattering becomes so strong that it turns thermal behaviour of crystalline solids to be glasslike and therefore, the presence of rattlers (or other strong phonon scatterers) has little impact. Thus, we suggest that introducing weak bonds would profitably reduce the high-temperature plateau *k*.

References

[1] R.Vassen, X.Q. Cao, F.Tietz, D.Basu and D.Stover. *Zirconates as new materials for thermal barrier coatings*. J Am Ceram Soc **83** (2000) 2023-2028.

[2] X.Q. Cao, R. Vassen and D.Stoever. *Ceramic materials for thermal barrier coatings.* J Eur Ceram Soc **24**(2004)1-10.

[3] N.P. Padture, M. Gell and E.H. Jordon. *Thermal barrier coatings for gas-turbine engine applications*. Science **296** (2002) 280-284.

[4] N.P.Bansal and D.M. Zhu. *Effects of doping on thermal conductivity of pyrochlore oxides for advanced thermal barrier coatings*. Mater Sci Engi A-Struct **459** (2007) 192-195.

[5] C.L.Wan, W. Pan, Q. Xu, Y.X. Qin, J.D. Wang, Z.X. Qu and M.H. Fang. *Effect of point defects on the thermal transport properties of* $(La_xGd_{1-x})_2Zr_2O_7$*: experiment and theoretical model*. Phys Rev B **74** (2006) 144109 1-9.

[6] H. Lehmann, D. Pitzer, G. Pracht, R. Vassen and D. Stover. *Thermal conductivity and thermal expansion coefficients of the lanthanum rare-earth-element zirconate system*. J Am Ceram Soc **86** (2003):1338-1344.

[7] P.K. Schelling. *Thermal conductivity of A-site doped pyrochlore oxides studied by molecular-dynamics simulation*. Comp Mater Sci **48** (2010) 336-342.

[8] C.Wan, W.Zhang, Y. Wang, Z.Qu, A. Du, R. Wu and W. Pan. *Glass-like thermal conductivity in ytterbium-doped lanthanum zirconate pyrochlore*. Acta Mater **58** (2010) 6166-6172.

[9] B. Abeles. *Lattice thermal conductivity of disordered semiconductor alloys at high temperatures*. Phys Rev **131** (1963) 1906-1911.

[10] B.C. Sales, D. Mandrus and R.K. Williams. *Filled skutterudite antimonides: a new class of thermoelectric materials*. Science **272** (1996) 1325-1328.

[11] V. Keppens, D. Mandrus, B.C. Sales, B.C. Chakoumakos, P. Dai, R. Coldea, M.B.Maple, D.A.Gajewski, E.J. Freeman and S.Bennington. *Localized vibrational modes in metallic solids*. Nature **395** (1998) 876-878.

[12] G.A. Slack and V.G. Tsoukala. *Some properties of semiconducting* $IrSb_3$. J Appl Phys **76** (1994) 1665-1671.

[13] D.G. Cahill, H.E. Fischer, S.K. Watson, R.O. Pohl and G.A. Slack. *Thermal properties of boron and borides*. Phys Rev B **40** (1989) 3254-3260.

[14] B.Saruhan, P. Francois, K. Fritscher and U. Schulz. *EB-PVD processing of pyrochlore-structured* $La_2Zr_2O_7$*-based TBCs*. Surf Coat Technol **182** (2004) 175-183.

[15] K.R. Whittle, L.M.D. Cranswick, S.A.T. Redfern, I.P. Swainson and G.R. Lumpkin. *Lanthanum pyrochlores and the effect of yttrium addition in the systems* $La_{2-x}Y_xZr_2O_7$ *and* $La_{2-x}Y_xHf_2O_7$. J Solid State Chem **182** (2009) 442-450.

[16] A. Ota, Y. Matsumura, M. Yoshinaka, K. Hirota and O. Yamaguchi. *Formation and sintering of 8 mol %* Y_2O_3*-substituted* $La_2Zr_2O_7$ *by the hydrazine method*. J Mater Sci Lett **17** (1998) 199-201.

[17] S.A. Speakman, R.D. Carneim, E.A. Payzant and T.R. Armstrong. Developments of proton conductors using pyrochlore-perovskite phase boundaries. J Mater Eng Perform **13** (2004) 303-308.

[18] O. Fabrichnaya, G. Savinykh, G. Schreiber, M. Dopita and H.J. Seifert. *Experimental investigation and thermodynamic modelling in the* ZrO_2-La_2O_3-Y_2O_3 *systems*. J Alloy Compd **493** (2010) 263-271.

[19] I.Barin. *Thermochemical Data of Pure Substances*, 3rd ed., Weinheim: VCH, 1995.

[20] M. Bolech, E.H.P. Cordfunke, A.C.G. VanGenderen, R.R. VanderLaan, F.J.J.G. Janssen and J.C. VanMiltenburg. *The heat capacity and derived thermodynamic*

functions of $La_2Zr_2O_7$ and $Ce_2Zr_2O_7$ from 4 to 1000K. J Phys Chem Solids **58** (1997) 433-439.

[21] D.G. Cahill, S.K. Watson and R.O. Pohl. *Lower limit to the thermal conductivity of disordered crystals*. Phys Rev B Condens Matter **46** (1992) 6131-6140.

[22] R.D. Shannon. *Revised effective ionic radii and systematic studies of interatomic distances in Halides and Chalcogenides*. Acta Cryst **A32** (1976) 751-767.

[23] P.K. Schelling and S.R. Phillpot. *Mechanism of thermal transport in zirconia and yttria-stabilized zirconia by molecular-dynamics simulation*. J Am Ceram Soc **84** (2001) 2997-3007.

[24] R. Mevrel, J.-C. Laizet, A. Azzopardi, B. Leclercq, M. Poulain, O.Lavigne and D. Demange. *Thermal diffusivity and conductivity of $Zr_{1-x}Y_xO_{2-x/2}$ (x = 0, 0.084 and 0.179) single crystals*. J Eur Ceram Soc **24** (2004) 3081-3089.

[25] D.R. Clarke. *Materials selection guidelines for low thermal conductivity thermal barrier coatings*. Surf Coat Technol **163-164** (2003) 67-74.

[26] M. Roufosse and P.G. Klemens. *Thermal conductivity of complex dielectric crystals*. Phys Rev B **7** (1973) 5379-5386.

[27] J.F. Bisson, D. Fournier, M. Poulain, O. Lavigne and R. Mevrel. *Thermal conductivity of yttria-zirconia single crystals, determined with spatially resolved infrared thermography*. J Am Ceram Soc **83** (2000) 1993-1998.

[28] P.G. Klemens. *The scattering of low-frequency lattice waves by static imperfections*. Proc Phys Soc Lond A **68** (1955) 1113-1128.

[29] P.G. Klemens. *Theory of thermal conduction in thin ceramic films*. Int J Thermophys **22** (2001) 265-275.

[30] C. Kittel. *Introduction to Solid State Physics*, 8th ed., John Wiley & Sons, 2005.

[31] G.A. Slack. *Thermal conductivity of MgO, Al_2O_3, $MgAl_2O_4$ and Fe_3O_4 crystals from 3 K to 300 K*. Phys Rev **126** (1962) 427-441.

[32] J.D. Eshelby. *The continuum Theory of Lattice Defects*, in: F. Seitz, D. Turnbull (Eds.). *Solid State Physics*, Vol.3. New York, Academic Press Inc., 1956.

[33] B.J. Wuensch and K.W. Eberman. *Order-disorder phenomena in $A_2B_2O_7$ pyrochlore oxides*. JOM-J Min Met Mat S **52** (2000) 19-21.

[34] R.A. McCauley. *Structural characteristics of pyrochlore formation*. J Appl Phys **51** (1980) 290-294.

[35] D.G. Cahill and R.O. Pohl. *Lattice-vibrations and heat-transport in crystals and glasses*. Ann Rev Phys Chem **39** (1988) 93-121.

[36] A.D. Caplin, G. Gruner and J.B. Dunlop. *$Al_{10}V$- Einstein solid*. Phys Rev Lett **30** (1973) 1138-1140.

[37] N.J. Hess, B.D. Begg, S.D. Conradson, D.E. McCready, P.L. Gassman and W.J. Weber. *Spectroscopic investigations of the structural phase transition in $Gd_2(Ti_{1-y}Zr_y)_2O_7$ pyrochlores*. J Phys Chem B **106** (2002) 4663-4677.

[38] P.G. Klemens. *Thermal resistance due to point defects at high temperatures*. Phys Rev **119** (1960) 507-509.

[39] M. Zebarjadi, K. Esfarjani, J. Yang, Z.F. Ren and G. Chen. *Effect of filler mass and binding on thermal conductivity of fully filled skutterudites*. Phys Rev B **82** (2010) 195207 1-6.

[40] Y.G. Wang, X.F. Xu and J.H. Yang. *Resonant oscillation of misch-metal atoms in filled skutterudites*. Phys Rev Lett **102** (2009) 175508 1-4.

[41] D.G. Cahill and R.O. Pohl. *Low-energy excitations in the mixed-crystal $Ba_{1-x}La_xF_{2+x}$*. Phys Rev B **39** (1989) 10477-10480.

[42] P.B. Allen and J.L. Feldman. *Thermal conductivity of disordered harmonic solids*. Phys Rev B **48** (1993) 12581-12588.

[43] J.L. Feldman, M.D. Kluge, P.B. Allen and F. Wooten. *Thermal conductivity and localization in glasses-numerical study of a model of amorphous silicon*. Phys Rev B **48** (1993) 12589-12602.

Chapter 4 Rattlers or oxygen vacancies: Determinant of high temperature plateau thermal conductivity in doped pyrochlores

4.1 Introduction

Heat transport at elevated temperature is extremely important in thermal insulation layers under harsh service environments such as for thermal barrier coatings (TBCs) [1]. The materials capable of surviving such extreme conditions are usually ceramics. For ceramics as typical dielectric materials, heat conduction at high temperature is primarily determined by phonon-phonon Umklapp scattering. Thermal conductivity (k) becomes almost constant (termed as the high temperature plateau k_{min}) beyond a critical temperature [2], at which the phonon mean free path Λ approaches the inter-atomic spacing Λ_0 whilst the specific volumetric heat capacity C_V approaches its asymptotic value ($3\mathrm{k_B}/a^3$), as shown in Eq.(4.1):

$$k_{\mathrm{min}}=\frac{1}{3}\frac{3k_B}{a^3}\Lambda_0 v \qquad (4.1),$$

where a^3, v and $\mathrm{k_B}$ are the average atomic volume, phonon group velocity and Boltzmann constant, respectively. Since v and a have very weak temperature dependence, they can be taken as constant at different temperatures. Consequently, the high temperature plateau k_{min} can be treated as a temperature independent value.

For a given material, both the atomic volume (a^3) and inter-atomic spacing (Λ_0) are fixed. To lower k_{min}, the only strategy is to reduce v, which can be expressed as [3]:

$$v = \xi' \sqrt{\frac{E}{\rho\gamma}} \tag{4.2}$$

in which ρ is the density, E is Young's modulus, γ is Grüneisen parameter (a description of lattice anharmonicity), and ξ' is a constant related to Poisson's ratio. Eq.(4.2) suggests a bigger γ and lower E favour a smaller v. Moreover, a stronger lattice anharmonicity leads to a greater decrease of E at high temperatures [4]. These suggest the dominance of γ over k_{min}.[3,4] Recently, Christensen et al [5] pointed out that lattice anharmonicity could be raised by introducing rattlers. As a recently-identified phonon scattering source, rattlers widely exist in a lattice with cage-like voids, such as filled skutterudites [6, 7], hydrate clathrates [8, 9] and Y (Chapter 3) and Yb [10] doped $La_2Zr_2O_7$ pyrochlores. In Chapter 3, a subtle decrease of k_{min} was found in Y doped $La_2Zr_2O_7$ with a variation of dopant content but it is not yet clear to attribute to rattlers or oxygen vacancies, the latter of which will later be identified as an effective enhancer of lattice anharmonicity besides their well-accepted role as strong phonon scatterers. Therefore, it is of theoretical and practical importance to study the effects of oxygen vacancies and rattlers on heat transport at high temperatures, and more crucially, the underlying factor determining k_{min}.

In this chapter, we study thermal conductivity of In/Sc doped $La_2Zr_2O_7$ pyrochlores because: (1) $La_2Zr_2O_7$ as a high-temperature TBC material, the high temperature k is exceptionally important; (2) the specific crystalline structure of $La_2Zr_2O_7$ allow us to investigate effects of both rattlers and oxygen vacancies on heat conduction: on one hand, one eighth of oxygen sites in $La_2Zr_2O_7$ lattice are empty, and they are ordered intrinsic oxygen vacancies (see Fig.4.1); on the other hand, as illustrated in Fig.4.1, the outward movement of O1 towards its adjacent oxygen vacancy forms oversized AO_8 cages and hence makes formation of rattlers possible; (3) considering the size effect of rattlers [8], we employ much smaller octahedrally coordinated cations (In^{3+}, 0.919 Å; Sc^{3+}, 0.87 Å)[11] than Y^{3+} (1.019 Å) or Yb^{3+} (0.985 Å) [11] to occupy the oversized AO_8 cages in order to achieve an enhanced rattling effect. Meanwhile, some of In^{3+}/Sc^{3+} dopants substitute for Zr^{4+} on B-sites to produce extra oxygen vacancies. Therefore, In/Sc-$La_2Zr_2O_7$ pyrochlores are expected to have both strong rattlers and a variation of oxygen vacancies. Our study suggests that, strong rattlers can effectively cause heat conduction glass-like at a very low doping level, while the oxygen vacancy concentration $[V_O]$ controls k_{min}. The underlying reason for the dominant effect of oxygen vacancies on k_{min} is further uncovered as the repulsive electrostatic force of cations surrounding anionic vacancy sites results in an enhanced lattice anharmonicity as well as a reduced elastic modulus.

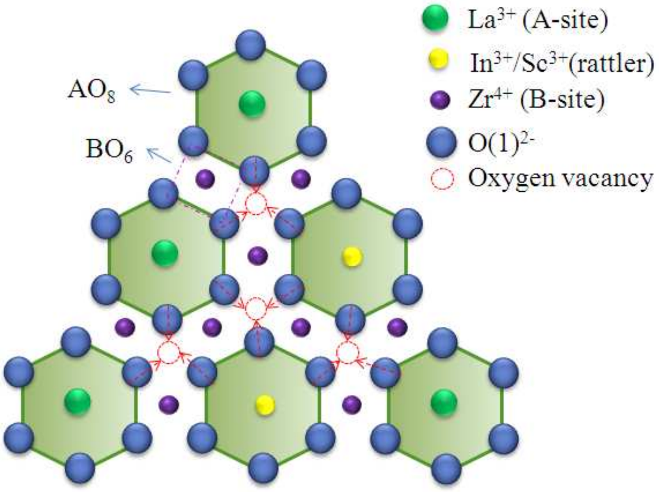

Fig.4.1 Schematic drawing of a pyrochlore structure along (1 1 1) plane. The pyrochlore constitutes two interpenetrating polyhedra: AO_8 dodecahedron and BO_6 octahedron respectively. A special feature of pyrochlores is that O1 tends to relax towards its adjacent vacancy as indicated by red arrows, which affords the formation of the oversized AO_8 cages, a necessity for the presence of rattlers.

4.2 Experiments

Polycrystalline pellets of $(La_{1-x_1}R_{x_1})_2(Zr_{1-x_2}R_{x_2})_2O_{7-x_2}$ (x=x_1+x_2, x=0.02, 0.05, 0.10, R=In, Sc) solid solutions were prepared by a conventional coprecipitation-calcination method using $La(NO_3)_36H_2O$, $ZrO(NO_3)_28H_2O$ and $In(NO_3)_36H_2O$, $Sc(NO_3)_36H_2O$ as starting materials. The powder processing and subsequent cold-pressing and sintering were the same as described in Chapter 3. The phase compositions were examined by X-ray diffraction (XRD) with Cu Kα radiation and Raman spectroscopy with the 514 nm line of an argon laser. The density (ρ) was measured by the Archimedes' method and the relative densities of all compositions were above 99.4% (Table 4.1). The thermal diffusivity (D) was measured by a laser-flash system (built-in house, Manchester, UK) in an argon atmosphere and the same procedure was followed after the description in Chapter 3. The specific heat capacitances (C_p) were measured using a simultaneous thermal analyzer (Netzsch STA 449C) in air. The measurements of ionic conductivity, providing the information on the occupation sites of In^{3+}/Sc^{3+} in pyrochlores, were conducted by the *ac* impedance spectroscopy on tablet samples by a Solatron SI 1255HF frequency response analyser coupled with a Solatron 1296 Dielectric Interface. Silver paint was coated on two polished surfaces and fired at 623 K for 1 h to serve as electrodes. During impedance measurements, an AC voltage of 0.1 V was applied to the sample over a frequency range from 0.1 to 10^7 HZ at 823 K. Equivalent circuit fittings of the measured impedance spectra were carried out using Zview Impedance Analysis Software. For a clear comparison, all impedance spectra were normalized by a geometric factor $\chi = 4h/(\pi L^2)$, where h and L denote to sample thickness and diameter, respectively, to eliminate the influence of sample geometry.

Table 4.1

Lattice parameter, theoretical, measured and relative densities of $La_2Zr_2O_7$ (x=0) and In/Sc-$La_2Zr_2O_7$ pyrochlore solid solutions (x=0.02, 0.05, 0.10).

	Lattice parameter (nm)	Theoretical density (g/cm^3)	Archimedes' density (g/cm^3)	Relative density
x=0	1.0801	6.035	6.04±0.02	100%
x=0.02(In)	1.0795	6.033~6.050 [a]	6.018±0.005	>99.5%
x=0.05(In)	1.0797	6.014~6.038 [a]	6.01±0.01	>99.5%
x=0.10(In)	1.0808	5.971~6.054 [a]	6.02±0.01	>99.4%
x=0.05(Sc)	1.0779	5.971~6.013 [a]	6.00±0.01	>99.8%
x=0.05(Y)	1.0780[b]	6.016	6.01±0.01[b]	>99.9%

[a] lowest and highest density calculated from purely A-site (In^{3+}/Sc^{3+}-La^{3+}) and B-site (In^{3+}/Sc^{3+}-Zr^{4+}) substitutions, respectively;

[b] from Chapter 3.

4.3 Results and discussions

Fig.4.2 shows the XRD (a) and Raman (b) patterns of In/Sc-$La_2Zr_2O_7$ solid solutions. The presence of small characteristic peaks reflects the specific cation ordering of the pyrochlore structure, suggesting all compositions crystallize into a cubic pyrochlore phase, which is further confirmed by the presence of four characteristic Raman bands of pyrochlore in (b). Neither XRD nor Raman patterns show any sign of a second phase, indicative of the complete dissolution of dopants at a given amount in the pyrochlore lattice.

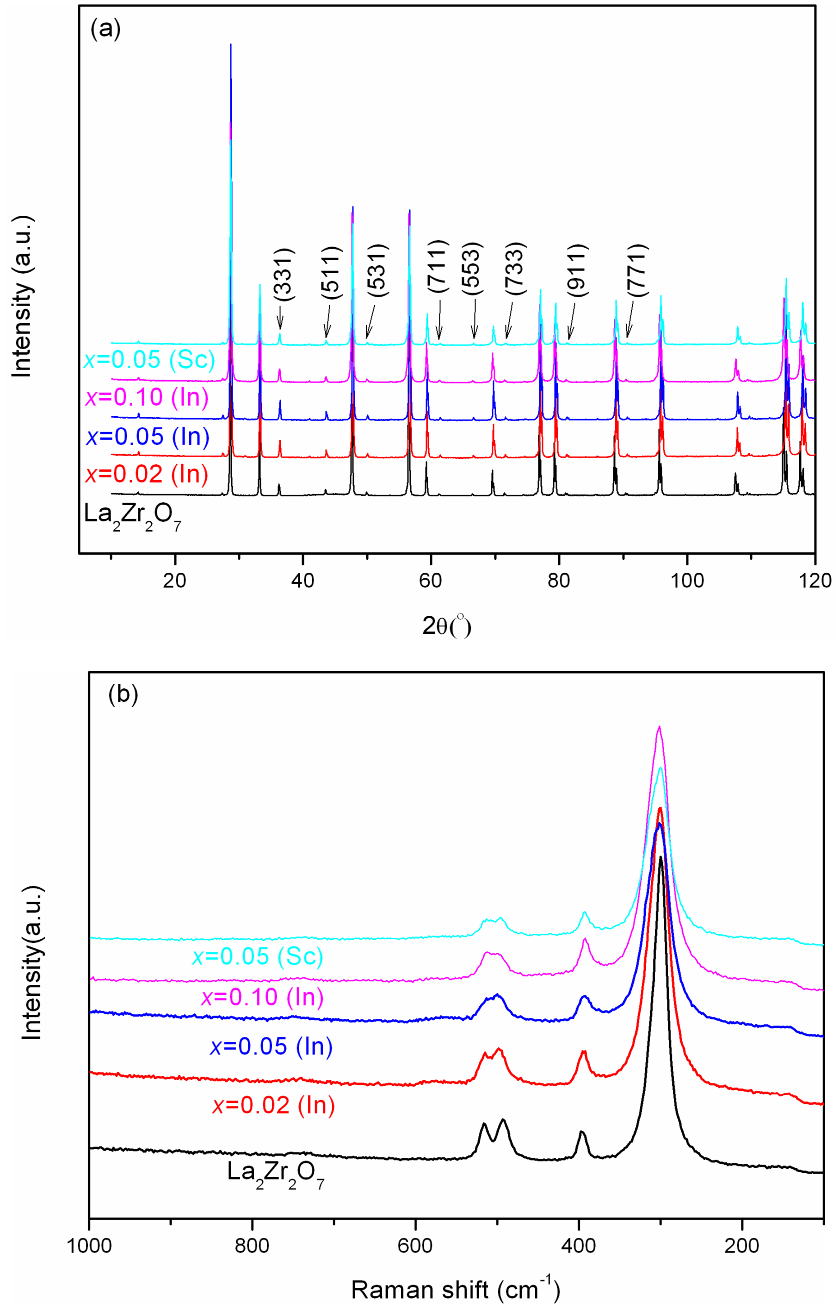

Fig.4.2 X-ray diffraction (a) and Raman (b) spectra of $La_2Zr_2O_7$ and In/Sc-$La_2Zr_2O_7$ solid solutions. The small reflections labelled with their Miller indices in (a) are characteristic peaks of the pyrochlore structure. The four Raman bands of pyrochlore in (b) are present for all compositions.

In^{3+}/Sc^{3+} dopants essentially substitute both La^{3+} on A-sites and Zr^{4+} on B-sites, supported by two pieces of evidence. Firstly, from the absence of lattice contraction with doping of Sc/In, it can be inferred that some of the dopant cations enter the hexagonally coordinated sites (B-sites), compensating the expected contraction anticipated if these cations were to enter only the octahedral sites (A-sites), according to a slight bigger size of dopant cations (In^{3+}: 0.80 Å; Sc^{3+}: 0.745 Å) occupying the hexagonal sites than their hosts (Zr^{4+}: 0.72 Å) [11]. Secondly, the aliovalent B-site substitutions inevitably generate additional oxygen vacancies, which can be reflected by an increase of electrical conductivity of In/Sc-$La_2Zr_2O_7$ pyrochlores (see Fig.4.3) from *ac* impedance spectroscopy measurements at 823 K. This is because, $La_2Zr_2O_7$ as an ionic conductor below 973 K [11], electrical conduction is achieved by an oxygen vacancy hopping mechanism [13] and hence a higher vacancy concentration favours a higher ionic conductivity. Therefore, In/Sc can substitute both La^{3+} on A-sites and Zr^{4+} on B-sites and the general formula can be represented as: $(La_{1-x_1}R_{x_1})_2(Zr_{1-x_2}R_{x_2})_2O_{7-x_2}$ (R=In, Sc).

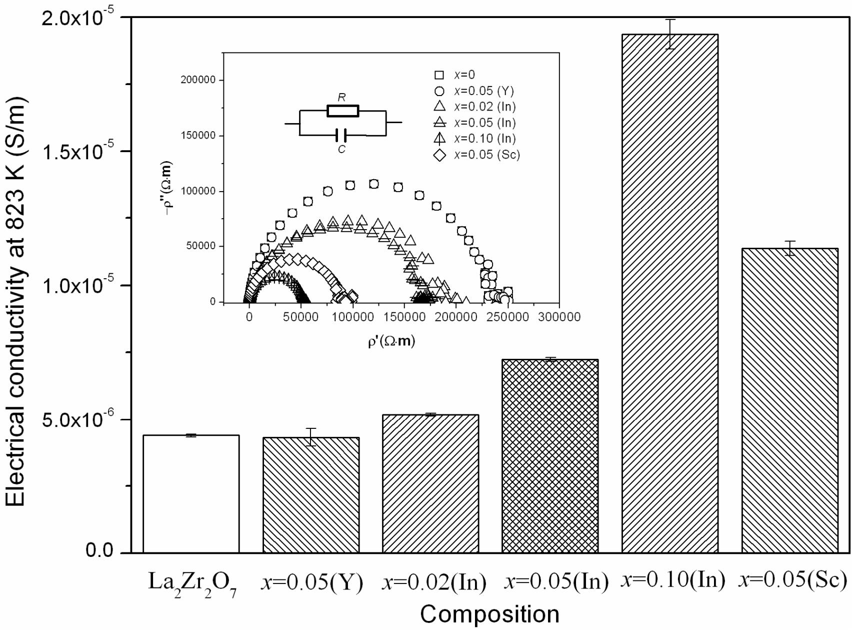

Fig.4.3 Ionic conductivity measured at 823 K for In/Sc-$La_2Zr_2O_7$ pyrochlore solid solutions in comparison with $La_2Zr_2O_7$ and $(La_{0.95}Y_{0.05})_2Zr_2O_7$. The increased ionic conductivity for In/Sc-$La_2Zr_2O_7$ pyrochlores suggests the increase of oxygen vacancies in lattice due to In^{3+}/Sc^{3+}-Zr^{4+} inter-substitution. The inset shows the Nyquist plot and the equivalent circuit for impedance data fitting.

Thermal conductivity of In/Sc-$La_2Zr_2O_7$ solid solutions is obtained according to:

$$k=\rho\cdot C_p\cdot D \qquad (4.3).$$

Fig.4.4 gives *k*-T curves of In/Sc-$La_2Zr_2O_7$ solid solutions, ZrO_2, yttria-stabilized zirconia (YSZ), Ba_2ErAlO_5, and $La_2Mo_2O_9$. Some of the curves are labeled by the lattice oxygen vacancy concentration [V_O], a ratio of all oxygen vacancies present on the basis of charge neutrality divided by all atomic sites in the lattice. For example, the proportions of vacant positions in oxygen sub-lattice ($\frac{1}{8}$, $\frac{1}{6}$ and $\frac{1}{4}$ for $La_2Zr_2O_7$, Ba_2ErAlO_5 [14] and $La_2Mo_2O_9$ respectively) multiplying by anionic proportions per unit formula, can get the corresponding [V_O] values shown in Fig.4.4. Here we find [V_O] determines $k_{\min}$: (1) $k_{\min}$ decreases consistently with an increase of [V_O] from 0 (ZrO_2) [15], 0.010 (3YSZ, $(Y_2O_3)_{0.03}(ZrO_2)_{0.97}$)[16], 0.014 (4.4YSZ, $(Y_2O_3)_{0.044}(ZrO_2)_{0.956}$) [15] to 0.083 ($Y_2Zr_2O_7$, $La_2Zr_2O_7$), 0.1 (Ba_2ErAlO_5) [14] and 0.188 ($La_2Mo_2O_9$) [17]; (2) For compounds with approximately similar [V_O] (around 0.083 for In, Sc, or Y lightly doped $La_2Zr_2O_7$ pyrochlores, their undoped counterpart, and $Y_2Zr_2O_7$ fluorite), they appear to exhibit similar $k_{\min}$, no matter what structures they possess: pyrochlore or fluorite, ordered or disordered (for $Y_2Zr_2O_7$) oxygen vacancies, and the presence or absence of rattlers. For In-$La_2Zr_2O_7$ (Fig.4.4(b)), with an increase of *x* from 0.02, 0.05 to 0.10, *k*-T curves exhibit a slight decreasing trend as a result of extra oxygen vacancies generated by In^{3+}-Zr^{4+} inter-substitution. By contrast, presence of rattlers, unlike oxygen vacancies, tends to dramatically flatten the *k*-T curves. For those solid solutions with the same doping content (x = 0.05 for Y, In, Sc, Fig.4.4 (b)), smaller rattlers show a greater capacity on

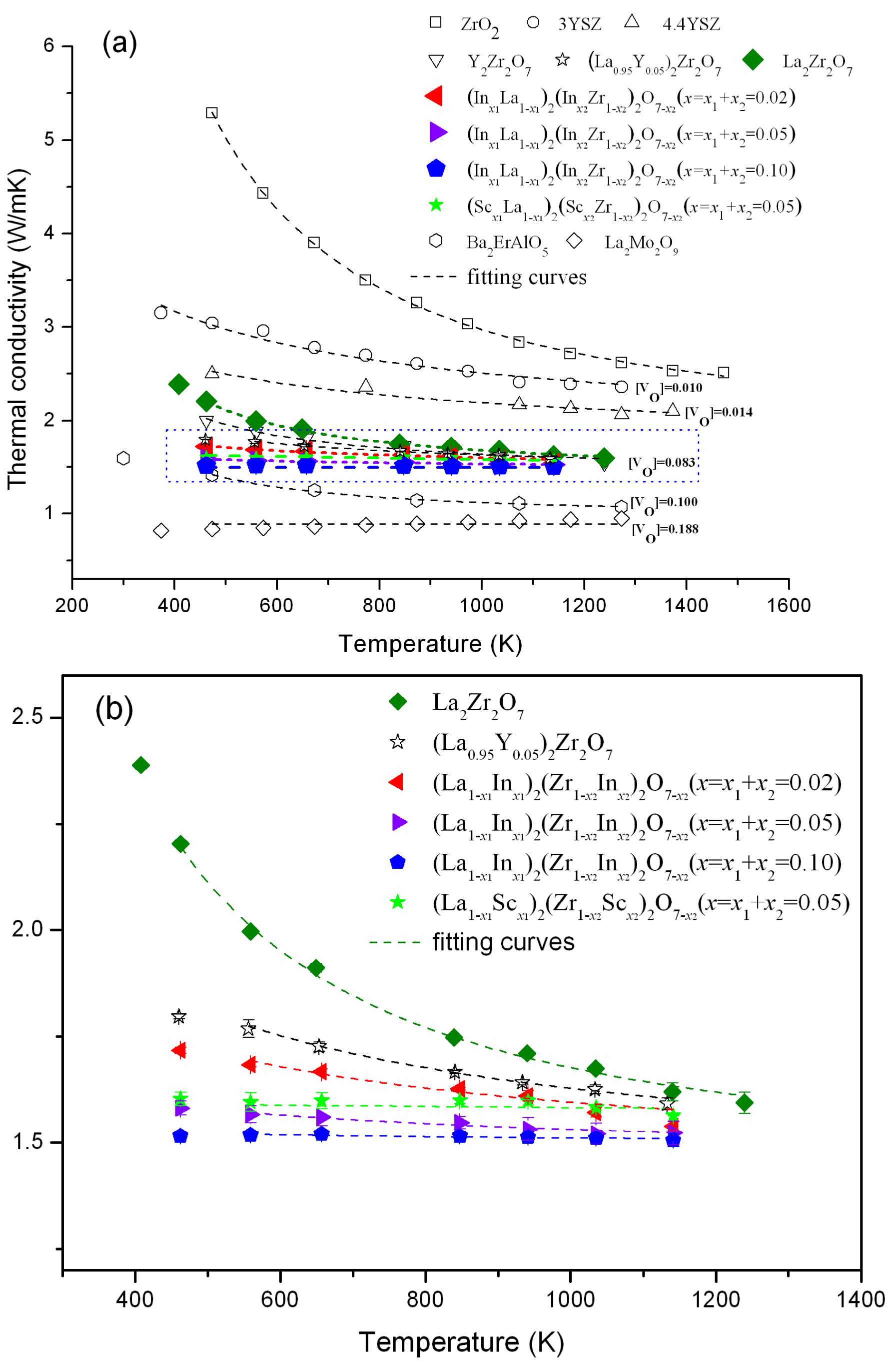

Fig.4.4 (a) Thermal conductivity – temperature (k-T) curves of In/Sc-$La_2Zr_2O_7$ pyrochlore solid solutions in comparison with compounds with varied levels of oxygen vacancy concentration [V_O] (b) enlarged plot of k-T curves of the rectangular area in (a). Solid symbols refer to measured values in this study whilst hollow symbols represent those extracted from references. All values represent the k of a fully dense material. The dashed lines are fitted based on the measured k according to Eq.(3.4) in Chapter 3. In (a), k_{min} decreases steadily with an increase of [V_O] and k_{min} appears to be similar for compounds with similar [V_O]. (b) suggests smaller rattlers have a stronger capacity on flattening the k-T curves.

driving k glass-like (i.e. enhanced rattling effect), particularly when considering that not all dopant cations act as rattlers. However, the stronger rattlers still have little influence on reducing $k_{\min}$.

By combining Eq.(4.1) and (4.2) and noticing the same order of a and Λ_0, we can obtain:

$$k_{\min} = \xi \sqrt{\frac{E}{a\overline{M}\gamma}} \tag{4.4}$$

where $\overline{M}$ is average atomic weight ($\rho = \overline{M} / a^3$). Eq.(4.4) suggests that $k_{\min}$ can be achieved by lowering the bonding strength E, or raising the average atomic volume (a^3) or mass ($\overline{M}$), or increasing Grüneisen parameter (γ). Table 4.2 lists parameters relating to Eq.(4.4) and Fig.4.5 (a) gives both Young's modulus and Grüneisen parameter as function of oxygen vacancy concentration. As shown in Table 4.2, for different compounds, the adjustable ranges of a and $\overline{M}$ are relatively small. However, an increase of the oxygen vacancy concentration $[V_O]$ in the lattice results in an almost linear decrease /increase of E /γ (see Fig.4.5 (a)), which can explain the reason why $[V_O]$ is the determinant of $k_{\min}$. Fig.4.5 (b) gives the linear regression of $k_{\min}$ against $\sqrt{E/a\overline{M}\gamma}$ for different compounds, which yields ξ in Eq.(4.4) around 2.43×10^{-23} $m^2 \cdot kg \cdot s^{-2}$.

Table 4.2

Average atomic mass ($\overline{M}$) and volume (a^3), Grüneisen parameter (γ) and elastic modulus (E) of compounds with different oxygen vacancy concentrations $[V_O]$ in the lattice

	$\overline{M}$ ($\times 10^{-26}$kg)	a (nm)	γ	$[V_O]$	E(GPa)
ZrO_2	6.85	0.225[a]	1.37[g]	0	220±10[k]
3YSZ	6.85	0.225[b]	1.39[h]	0.010	
4.4YSZ	6.87	0.225[c]	1.40[g]	0.014	
$La_2Zr_2O_7$	8.64	0.243	2.07[d]	0.083	180±2[d]
$Y_2Zr_2O_7$	7.13	0.234[d]	2.08[d]	0.083	155±5[d]
x=0.02(In)	~8.64	0.243	~2.07	~0.083	175±2[*l*]
x=0.05(In)	~8.60	0.243	~2.07	~0.083	169±4[*l*]
x=0.10(In)	~8.57	0.243	~2.07	~0.083	165±3[*l*]
x=0.05(Sc)	~8.54	0.242	~2.07	~0.083	185±2[*l*]
Ba_2ErAlO_5	10.13	~0.25[e]	~2.2[e]	0.100	109±8[e]
$La_2Mo_2O_9$	7.84	0.243[f]	~2.6[i]	0.188	~70

[a] Ref.[18];

[b] Ref.[19];

[c] Ref.[20];

[d] from Chapter 3;

[e] Ref.[19];

[f] Ref.[20];

[g] Ref.[17];

[h] Ref.[18];

[i] estimated;

[k] Ref.[21,22];

[*l*] measured in this study by micro-indentation.

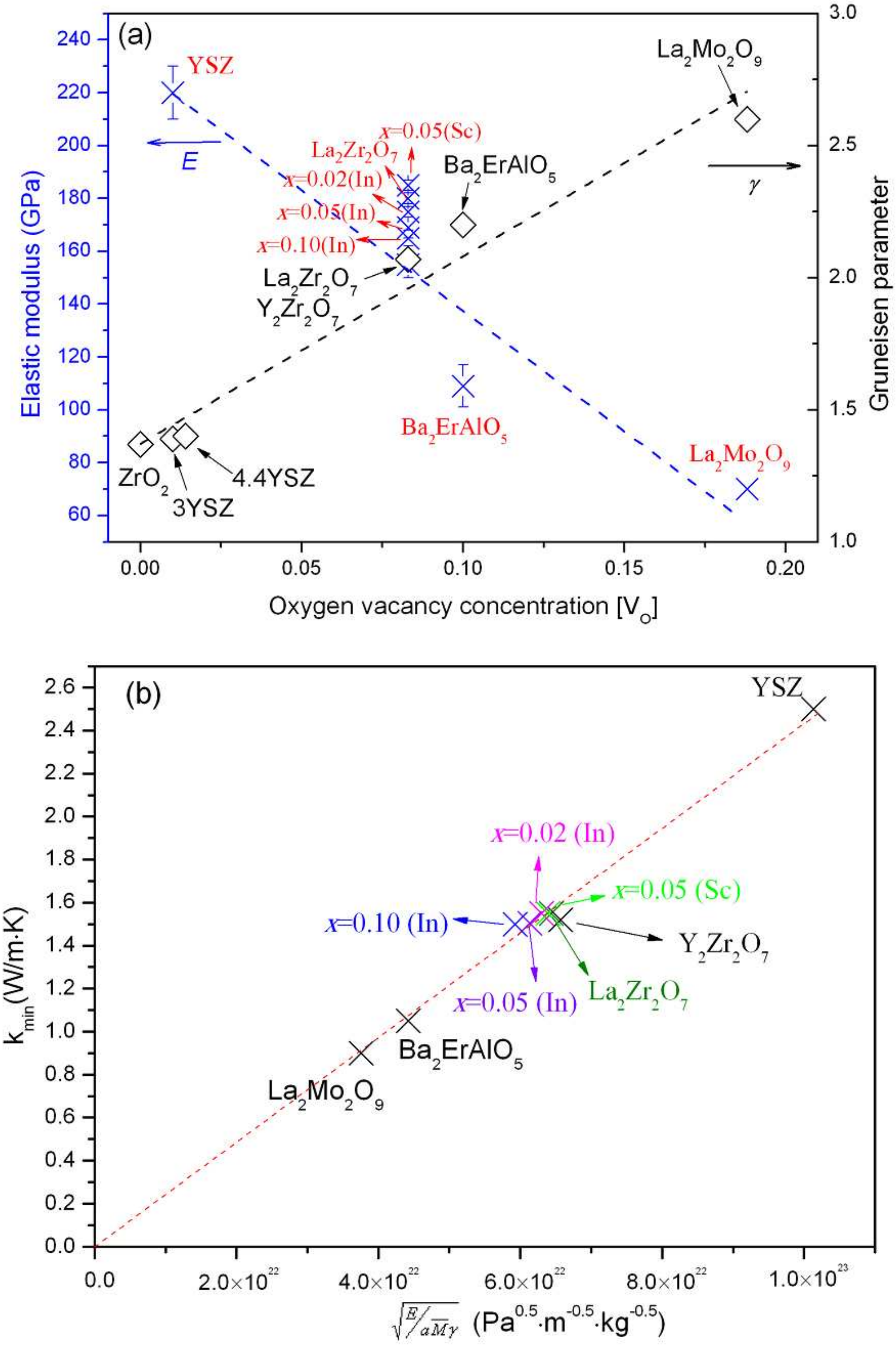

Fig.4.5 (a) The dependence of Young's modulus (E) and Grüneisen parameter (γ) on the oxygen vacancy concentration [V_O] and (b) the linear plot of k_{min} versus $\sqrt{E/a\overline{M}\gamma}$ for different materials.

The increase of γ and the decrease of E by oxygen vacancies arise from an electrostatic repulsion force of exposed cations surrounding them, because the emergence of vacancies disrupts the alternation of anions and cations in the perfect ionic lattice and therefore leads to cations/anions exposed to each other around anionic/cationic vacancies. For a normal lattice, anharmonic cubic term of the inter-atomic potential energy expansion favors lattice expansion as if it generates a repulsive component of the lattice force. Conversely, the presence of any additional repulsion of the lattice force can in turn contribute to a stronger lattice anharmonicity, which is supported by the findings of Morelli and coworkers, who reported an anomalously large γ (strong anharmonicity) in cubic I-V-VI_2 semiconductors and attributed it to the electrostatic repulsion of lone-pair electrons [23,24]. As an analogy, we propose the electrostatic repulsive force of the exposed cations surrounding oxygen vacancies as the underlying reason for the strong anharmonicity at oxygen vacancy sites. As evidence, Hayashi and co-workers found a steady increase of Grüneisen parameter in YSZ with an increase of the Y_2O_3 content, or essentially [V_O] [25]. Similarly, it is understandable that the repulsive lattice force introduced by vacancies can reduce the bonding strength, since the lattice repulsion force arising from neighbouring cations/anions surrounding anionic/cationic vacancies offsets a certain attractive force which defines the strength of bond.

The remaining question is why strong rattlers, despite their amazing capability of driving k glass-like, are still not able to reduce $k_{\min}$. The fact that rattlers are good at flattening the decreasing temperature dependence of k indicates that, according to $k = \frac{1}{3} C_v v \Lambda$, they are essentially affecting Λ, or precisely the mean free path due to phonon Umklapp scattering Λ_U, since the decreasing temperature dependence of k primarily originates from Λ_U. As shown in Eq.(4.5), the temperature independent rattler term becomes exceptionally large when the phonon frequency ω approaches the resonant frequency ω_{Ri}, and thus overshadows the Λ_U term [26-28]:

$$\frac{1}{\Lambda} = \frac{1}{\Lambda_U(\omega)} + \frac{1}{\Lambda_{rattler}(\omega)} = \frac{\omega^2 T}{D_U} + \sum_i \frac{C_i \omega^2}{(\omega_{Ri}^2 - \omega^2)^2} \tag{4.5}$$

in which D_U and C_i are temperature independent constants.

Otherwise, if rattlers effectively decreased v by raising lattice anharmonicity, as suggested in Ref.[29,30], k would become consistently lower at all temperatures but show an evident temperature dependent trend, i.e. parallel k-T curves rather than flattened ones. However, at high temperatures, heat is conducted by high-frequency phonons which are insensitive to rattlers, since they tend to scatter low-frequency phonons [7,31]. Therefore, rattlers are not effective, at least not as oxygen vacancies are, in raising lattice anharmonicity, and thus have little influence on $k_{\min}$.

4.4 Conclusions

To conclude, we have revealed the importance of rattlers and their size effect on heat transport. Smaller In^{3+}/Sc^{3+} rattlers, residing in the oversized atomic AO_8 cages, make *k* of In/Sc-$La_2Zr_2O_7$ pyrochlores glass-like at an amazingly low doping content (x=0.05) but still show no significant decrease of k_{min}. By contrast, oxygen vacancies, generated by In^{3+}/Sc^{3+} substituting Zr^{4+} on B-sites, are very powerful in reducing k_{min}, especially by enumerating compounds with a wide range of oxygen vacancy concentration [V_O]. We have found that k_{min} decreases steadily with an increase of [V_O], whereas, k_{min} is almost identical at a given [V_O], with any structure details irrelevant. The underlying reason has been suggested that the electrostatic repulsive force of cations surrounding oxygen vacancies leads to stronger lattice anharmonicity as well as weaker atomic bonds. To lower k_{min}, we suggest introducing a repulsion component of the lattice force, such as with vacancies, interstitials, etc.

References

[1] N. P. Padture, M. Gell and E. H. Jordan. Thermal barrier coatings for gas turbine engine applications. Science **296** (2002) 280-284.

[2] D. R. Clarke. Materials selection guidelines for low thermal conductivity thermal barrier coatings. Surf Coat Tech **163-164** (2003) 67-74.

[3] D. S. Sanditov, V. V. Mantatov, M. V. Darmaev and B. D. Sanditov. *On the Gruneisen parameter for crystals and glasses*. Tech Phys+ **54** (2009) 385-388.

[4] O. L. Anderson. *Derivation of Wachtmans Equation for temperature dependence of elastic moduli of oxide compounds*. Phys Rev **144** (1966) 553-557.

[5] M. Christensen, A. B. Abrahamsen, N. B. Christensen, F. Juranyi, N. H. Andersen, K. Lefmann, J. Andreasson, C. R. H. Bahl and B. B. Iversen. *Avoided crossing of rattler modes in the thermoelectric materials*. Nat Mater **7** (2008) 811-815.

[6] B.C. Sales, D. Mandrus, R.K. Williams. *Filled skutterudite antimonides: a new class of thermoelectric materials*. Science **272** (1996) 1325-1328.

[7] G. S. Nolas, M.Kaeser, R.T. Littleton IV and T.M. Tritt. High figure of merit in partially filled ytterbium skutterudite materials. Appl Phys Lett **77** (2000) 1855-1857.

[8] G. S. Nolas, J. L. Cohn, G. A. Slack and S. B. Schujman. *Semiconducting Ge clathrates: promising candidates for thermoelectric applications*. Appl Phys Lett **73** (1998) 178-180.

[9] G. S. Nolas and G. A. Slack. *Thermoelectric clathrates*. Am Sci **89** (2001) 136-141.

[10] C.Wan, W.Zhang, Y. Wang, Z.Qu, A. Du, R. Wu and W. Pan. *Glass-like thermal conductivity in ytterbium-doped lanthanum zirconate pyrochlore*. Acta Mater **58** (2010) 6166-6172.

[11] Shannon RD. *Revised effective ionic radii and systematic studies of interatomic distances in Halides and Chalcogenides*. Acta Cryst **A32** (1976) 751-767.

[12] J. A. Labrincha, J. R. Frade and F. M. B. Marques. *$La_2Zr_2O_7$ formed at ceramic electrode YSZ contacts*. J Mater Sci **28** (1993) 3809-3815.

[13] P. J. Wilde and C. R. A. Catlow. *Defects and diffusion in pyrochlore structured oxides*. Solid State Ionics **112** (1998) 173-183.

[14] C. L. Wan, Z. X. Qu, Y. He, D. Luan and W. Pan. *Ultralow thermal conductivity in highly anion-defective aluminates*. Phys Rev Lett **101** (2008) 085901 1-4.

[15] R. Mevrel, J.-C. Laizet, A. Azzopardi, B. Leclercq, M. Poulain, O.Lavigne and D. Demange. *Thermal diffusivity and conductivity of $Zr_{1-x}Y_xO_{2-x/2}$ ($x = 0, 0.084$ and 0.179) single crystals*. J Eur Ceram Soc **24** (2004) 3081-3089.

[16] K.W. Schlichting, N.P. Padture and P.G. Klemens. *Thermal conductivity of dense and porous yttria-stabilized zirconia*. J Mater Sci **36** (2001) 3003-3010.

[17] M. R. Winter and D. R. Clarke. Oxide materials with low thermal conductivity. J Am Ceram Soc **90** (2007) 533-540.

[18] F. Yang, X. F. Zhao and P. Xiao. *The effects of temperature and composition on the thermal conductivities of $[(ZrO_2)_{1-x}(CeO_2)_x]_{0.92}(Y_2O_3)_{0.08}$ ($0 \leq x \leq 1$) solid solutions*. Acta Mater **60** (2012) 914-922.

[19] U. Martin, H. Boysen and F. Frey. *Neutron powder investigation of tetragonal and cubic stabilized zirconia, TZP and CSZ at temperatures up to 1400 ^oK*. Acta Crystallogr B **49** (1993) 403-413.

[20] J. A. Krogstad, M. Lepple, Y. Gao, D. M. Lipkin and C. G. Levi. *Effect of yttria content on the zirconia unit cell parameters*. J Am Ceram Soc **94** (2011) 4548-4555.

[21] S. Giraud and J. Canel. Young’s modulus of some SOFCs materials as a function of temperature. J Eur Ceram Soc **28** (2008) 77-83.

[22] R.Vassen, X.Q. Cao, F.Tietz, D.Basu, D.Stover. *Zirconates as new materials for thermal barrier coatings*. J Am Ceram Soc **83** (2000) 2023-2028.

[23] D. T. Morelli, V. Jovovic and J. P. Heremans. *Intrinsically minimal thermal conductivity in cubic I-V-*VI_2 *semiconductors*. Phys Rev Lett **101** (2008) 035901 1-4.

[24] E. J. Skoug and D. T. Morelli. *Role of lone-pair electrons in producign minimum thermal conductivity in nitrogen-group chalcogenide compounds*. Phys Rev Lett **107**, (2011) 235901 1-4.

[25] H. Hayashi, T. Saitou, N. Maruyama, H. Inaba, K. Kawamura and M. Mori. *Thermal expansion coefficient of yttria stabilized zirconia for various yttria contents*. Solid State Ionics **176** (2005) 613-619.

[26] Y.G. Wang, X.F. Xu, J.H. Yang. *Resonant oscillation of misch-metal atoms in filled skutterudites*. Phys Rev Lett **102** (2009) 175508 1-4.

[27] G. S. Nolas, J. L. Cohn, B. C. Chakoumakos and G. A. Slack. *Proceedings of the 25th International Thermal Conductivity Conference*, edited by C. Uher and D.T. Morelli, Technomic Publishing Co., Lancaster, PA, 2000, pp.122.

[28] X. Shi, H. Kong, C.-P. Li, C. Uher, J. Yang, J.R. Salvador, H. Wang, L. Chen and W. Zhang. *Low thermal conductivity and high thermoelectic figure of merit in n-type* $Ba_xYb_yCo_4Sb_{12}$ *double-filled skutterudites*. Appl Phys Lett **92** (2008) 182101 1-3.

[29] J. S. Tse, D. D. Klug, J. Y. Zhao, W. Sturhahn, E. E. Alp, J. Baumert, C. Gutt, M. R. Johnson and W. Press. *Anharmonic motions of Kr in the clathrate hydrate*. Nat Mater **4** (2005) 917-921.

[30] O. Delaire, J. Ma, K. Marty, A. F. May, M. A. McGuire, M. H. Du, D. J. Singh, A. Podlesnyak, G. Ehlers, M. D. Lumsden and B. C. Sales. *Giant anharmonic phonon scattering in PbTe*. Nat Mater **10** (2011) 614-619.

[31] J. S. Tse, V. P. Shpakov, V. R. Belosludov, F. Trouw, Y. P. Handa and W. Press. *Coupling of localized guest vibrations with the lattice modes in clathrate hydrates*. Europhys Lett **54** (2001) 354-360.

Chapter 5 Role and determining factor of substitutional defects on thermal conductivity: A study on $La_2(Zr_{1-x}B_x)_2O_7$ (B=Hf, Ce, $0 \leq x \leq 0.5$) pyrochlore solid solutions

5.1 Introduction

One of the conventional methods to reduce the thermal conductivity (k) of materials is to introduce substitutional defects to the lattice. A substitutional defect induces a mass contrast, a linkage (or force constant) difference and an elastic field [1,2], which are all effective phonon scattering sources to decrease k. In order to further reduce the k of a material for the application such as thermal barrier coatings (TBC), numerous researches [2-12] have been carried out to study the effect of substitutional defects on k. However, the following several issues still remain unclear.

(1) Are substitutional defects as strong phonon scatterers as vacancies? Vacancies are usually believed to be very strong phonon scatterers due to the complete mass and linkage losses, together with an intensive elastic field generated from the maximum size mismatch between the host ion and the vacancy. In this perspective, substitutional defects are relatively weak phonon scatterers as the guest ion can only cause a limited mass and size mismatch. However, Raghavan et al [5] and Shen et al [6] observed that, zirconia doped with equimolar (16 mol% - 20 mol%) trivalent ($Y/YbO_{1.5}$) and pentavalent ($Nb/TaO_{2.5}$) oxides without any oxygen vacancies showed a temperature independent k, which is much lower than that of 16 mol% $YO_{1.5}$ stabilized zirconia [6] with a considerably large amount of oxygen vacancies. Their results suggest that the

substitutional defects can be as effective as vacancies in scattering phonons. However, the underlying mechanism is still unclear.

(2) Which factor is more important to the phonon scattering of substitutional defects, the mass or the ionic size difference between guest and host ions? Although the majority of the studies are based on defect scattering models proposed by Slack [13] and Abeles [14], mass difference is more readily considered than size difference in the literature [5-9] owing to an unknown adjustable parameter (□) related to the size difference. As a result, the contribution of ionic size disorder to *k* reduction is somehow underestimated, which does not cause big problems in the case of a similar ionic size for host and guest ions, such as Hf^{4+} substituting for Zr^{4+} in yttria-stabilized zirconia (YSZ) [9]. However, in the study of $YNb(Ta)O_4$ co-doped zirconia, Raghavan et al[5] found Nb^{5+}(92.91 a.u., 0.69 Å [15]) and Ta^{5+} (180.95 a.u., 0.69 Å[15]), the mass of the former is an half of the latter, were equally effective in lowering the *k* of YSZ, suggesting that the contribution of the ionic size difference between Nb^{5+} (or Ta^{5+}) and Zr^{4+} (91.224 a.u., 0.78 Å [15]) overrides that of their mass difference. This is confirmed by Song et al [10], who argued that the elastic fields caused by the size difference contributed overwhelmingly than the mass variation to *k* reduction in $YNbO_4$ doped zirconia where Y was partially substituted by some rare earth elements. This issue still needs further investigation.

(3) Do substitutional defects influence the high temperature plateau thermal conductivity (k_{min})? If they do, how do they affect k_{min}? The k_{min} is a plateau minimum value of thermal conductivity that a ceramic material reaches beyond a critical temperature [16, 17]. Normally substitutional defects reduce *k* effectively by increasing scattering coefficient Γ (which relies on the relative difference between guest and host ions) at

relatively low temperatures where phonon-point defects scattering dominates; whereas, they are generally believed to have negligible influence on the high temperature regime where Umklapp phonon scattering dominates heat transport. However, Winter and Clarke [9] found for the first time that $k_{\min}$ could be markedly reduced by substituting a much-heavier Hf^{4+} ion for the Zr^{4+} host in the YSZ lattice due to an increase of average atomic mass $\overline{M}$. Nevertheless, yttria stabilized hafnia (YSH) that can be seen as a complete substitution of Zr^{4+} by Hf^{4+} in the YSZ lattice and thus having the heaviest $\overline{M}$ did not have the lowest $k_{\min}$, which indicates some factors other than the mass alone influencing $k_{\min}$. A second factor is apparently the Grüneisen parameter (γ), a reflection of the lattice anharmonicity and the strength of Umklapp phonon scattering. A third factor is suggested as the strength of the inter-atomic bond (or the elastic modulus E) by Chapter 4, in which the oxygen vacancies in the lattice are the determinant of $k_{\min}$ because vacancies facilitate not only the increase of γ but also the decrease of E. However, for substitutional defects, it is still unknown whether they can influence γ and/or E.

To clarify the role and its determining factor of a substitutional defect on heat transport particularly at high temperatures, we studied Hf^{4+} and Ce^{4+} doped $La_2Zr_2O_7$ pyrochlores. With reference to the Zr^{4+} host as shown in Table 5.1, Hf^{4+} has a 96% heavier mass and an almost identical ionic size whilst Ce^{4+} has a 21% larger ionic size and a 50% heavier mass. Hence, the roles of the relative mass/size difference of a dopant, or its absolute values played in heat transport can be distinguished. We find that, the high temperature plateau $k_{\min}$ is determined by the absolute mass/size value of dopants, particularly the latter, attributable to that $k_{\min}$ is proportional to $\sqrt{E/\overline{M}}$ and that a larger dopant ion substituted tends to dramatically weaken an inter-atomic bond exhibiting typical ionic character. By contrast, the low and intermediate *k* (or the *k*-T curve flatness) is controlled by the relative mass/size difference between substituting and substituted ions, particularly the size difference. The insights gained in this study into the high temperature plateau regime provide a guideline for the design and selection of a low-*k* material at high temperatures.

Table 5.1

The atomic mass and size of the hexagonally coordinated Zr^{4+}, Ce^{4+} and Hf^{4+}

	Zr^{4+}	Ce^{4+}	Hf^{4+}
Ionic radius (VI-coordinated, Å)	0.72 [a]	0.87 [a]	0.71 [a]
Mass (a.u.)	91.224	140.12	178.49

[a] From Ref.[15]

5.2 Experiments

The powders of $La_2(Zr_{1-x}B_x)_2O_7$ (B=Hf, Zr, $0 \leq x \leq 0.5$) were synthesized by the solid state reaction method. Appropriate amounts of La_2O_3 (Sigma Aldrich, UK, 99.9% pure), ZrO_2 (Pi-Kem, UK, 99.9% pure), HfO_2 (Sigma Aldrich, UK, 99.8% pure) and CeO_2 (Pi-Kem, UK, 99.98% pure) were weighed after they were heated at 1373 K for 4 h to remove the absorbed moisture. The oxide mixtures were attrition milled (400 r.p.m.) in distilled water for 24 h and then subjected to freeze-drying. The powders obtained were subsequently reacted at 1473 K for 24 h. In order to achieve a thorough reaction of oxides and thus a homogeneous composition, the resulting powders were then undergone another cycle of milling, drying and reacting. The finally obtained fine powders with the designed compositions were cold pressed into tablets under a uniaxial pressure of 100 MPa and sintered at 1873 K for 2 h.

The phase compositions of the sintered pellets were identified by X-ray diffraction (XRD) (Philips X'Pert) with a CuK_α radiation. The lattice parameters were calculated from fine scan XRD patterns (from 5^o to 120^o, 0.05^o per step, $0.003^o s^{-1}$) of the corresponding powders. The phases were further identified using a Raman optical microprobe system (Renishaw 1000, UK) .The spectra were generated with use of the 514 nm wavelength argon laser, and collected across the wave numbers from 100 to 1000 cm^{-1}. Densities of the sintered specimens were measured by the Archimedes' method. The speed of sound in each of the solid solutions, used for the discussion of high temperature thermal conductivity, was estimated from the Young's modulus of the samples, which were measured by micro-indentation (MHTX CSM Inc. Switzerland). The thermal diffusivities were measured by the laser flash technique as reported in Chapter 3.

The specific heat capacitances of the solid solutions at various temperatures were calculated according to the Neumann-Kopp rule based on the reference specific heat values [18] of La_2O_3, ZrO_2, HfO_2 and CeO_2, as listed in Table 5.2. The validation of the Neumann-Kopp rule in pyrochlores has been proved in Chapter 3. The thermal conductivities (k) of the solid solutions were obtained from the density (ρ), specific heat capacitance (C_p) and thermal diffusivity (D) using the relationship:

$$k = \rho \cdot C_p \cdot D \tag{5.1}$$

Table 5.2

Specific heat capacities of La_2O_3, ZrO_2, HfO_2 and CeO_2 extracted from Barin [18] and calculated for $La_2(Zr_{1-x}Hf_x)_2O_7$ and $La_2(Zr_{1-x}Ce_x)_2O_7$ solid solutions based on the Neumann- Kopp rule at various temperatures.

T (K)	Specific heat capacity (J g^{-1} K^{-1})													
					x in $La_2(Zr_xB_{1-x})_2O_7$									
	La_2O_3	ZrO_2	HfO_2	CeO_2	B=Hf					x=0	B=Ce			
					0.1	0.2	0.3	0.4	0.5		0.1	0.2	0.3	0.4
462	0.366	0.538	0.330	0.401	0.428	0.417	0.406	0.396	0.386	0.440	0.433	0.427	0.421	0.415
559	0.378	0.564	0.346	0.418	0.446	0.434	0.423	0.412	0.403	0.458	0.451	0.445	0.438	0.432
657	0.387	0.581	0.358	0.431	0.458	0.446	0.435	0.424	0.414	0.471	0.464	0.457	0.450	0.444
847	0.400	0.601	0.373	0.447	0.474	0.461	0.450	0.439	0.429	0.487	0.479	0.472	0.466	0.459
941	0.405	0.609	0.377	0.453	0.480	0.468	0.456	0.445	0.434	0.493	0.486	0.479	0.472	0.465
1035	0.409	0.619	0.382	0.458	0.486	0.474	0.462	0.450	0.440	0.500	0.492	0.485	0.478	0.471
1141	0.413	0.631	0.386	0.464	0.494	0.480	0.468	0.457	0.445	0.507	0.500	0.492	0.485	0.478

5.3 Results

5.3.1 Phase compositions

Fig.5.1 (a) shows the XRD patterns of the solid solutions. Due to the similar ionic size between the dopant (Hf^{4+}) and host (Zr^{4+}) cations, all compositions studied ($0\leq x \leq 0.5$) for $La_2(Zr_{1-x}Hf_x)_2O_7$ exhibit single pyrochlore structure and no evident peak shifts can be detected. On the contrary, the substitution of Zr^{4+} hosts by bigger Ce^{4+} dopants results in peaks shifting towards low angles (i.e. lattice expansion) as well as the pyrochlore (order) to fluorite (disorder) transition. Therefore, $La_2(Zr_{1-x}Ce_x)_2O_7$ with a low doping content ($x \leq 0.3$) exhibits a single pyrochlore phase, whereas, that with a higher x shows a mixture of pyrochlore and fluorite phases, which can be reflected by the “broadened” XRD peaks of $La_2(Zr_{1-x}Ce_x)_2O_7$ with x = 0.4, 0.5, owing to the coalescence of the very close neighbouring peaks of $La_2Zr_2O_7$ pyrochlores and $La_2Ce_2O_7$ fluorites.

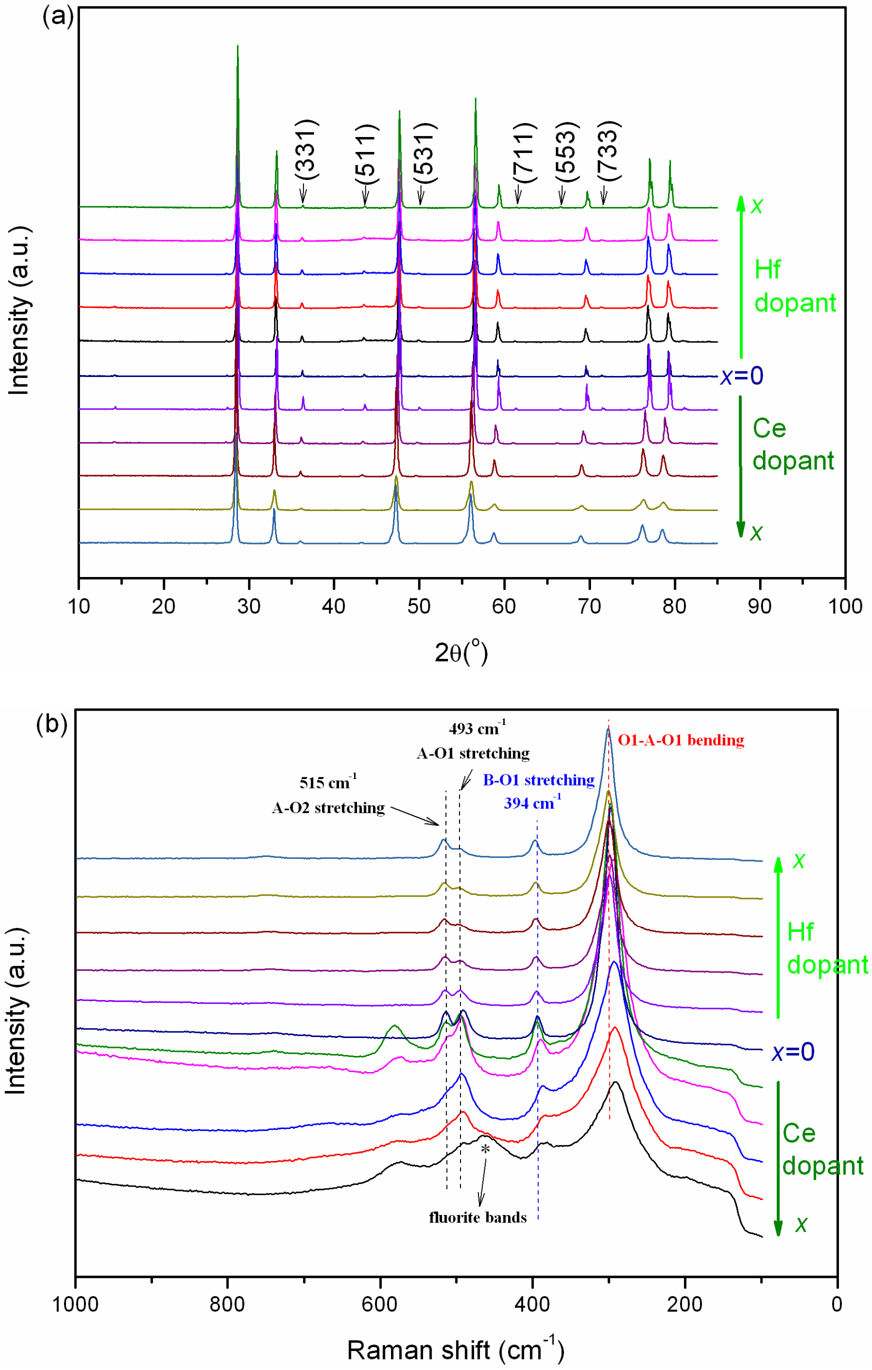

Fig.5.1 XRD pattern (a) and Raman spectra (b) of $La_2(Zr_{1-x}B_x)_2O_7$ (B=Hf, Ce, $0\leq x \leq 0.5$) solid solutions. The small reflections annotated with the Miller indices in (a) and the A-O2 stretching mode at 515 cm^{-1} in (b) are characteristic peaks of the pyrochlore phase.

In comparison with XRD patterns, the Raman spectra (Fig.5.1 (b)) provide consistent but complementary structural details of the solid solutions. For Hf^{4+} doped $La_2Zr_2O_7$, all compositions exhibit four typical Raman bands of pyrochlores. No impurity bands can be detected. The Raman bands at around 394 cm^{-1}, representing the B-O1 stretching mode [11, 19], slightly shift to high frequencies (blue shifts), indicative of bond shortening and strengthening, as a result of a slightly smaller Hf^{4+} substituting its host Zr^{4+}. By contrast, for Ce^{4+} doped $La_2Zr_2O_7$, the same Raman bands markedly shift toward low frequencies (red shift), suggesting bond elongating and weakening due to a much bigger Ce^{4+} replacing its Zr^{4+} host. With Ce^{4+} progressively substituting Zr^{4+}, $La_2(Zr_{1-x}Ce_x)_2O_7$ gradually undergoes the pyrochlore-to-fluorite transition, which can be reflected by (1) the gradual broadening of Raman bands; and (2) the gradual disappearance of characteristic bands at about 515 cm^{-1} for pyrochlores, corresponding to A-O2 stretching mode [19]. On the other hand, the Raman bands of $La_2Ce_2O_7$ fluorites are present at 460 cm^{-1} [20] for composition at $x = 0.5$.

5.3.2 Lattice parameter and density

Fig.5.2 shows the measured lattice parameters of Hf^{4+} and Ce^{4+} doped $La_2Zr_2O_7$ solid solutions. As shown, the lattice parameters of $La_2(Zr_{1-x}Ce_x)_2O_7$ increase linearly with x, in line with the lattice expansion due to a bigger Ce^{4+} dopant substituting its host Zr^{4+}. By contrast, the lattice parameters of $La_2(Zr_{1-x}Hf_x)_2O_7$ decrease linearly with a smaller slope, attributed to a slightly smaller Hf^{4+} dopant than its host Zr^{4+}. Table 5.3 lists theoretical, Archimedes' and relative densities of the Hf /Ce doped $La_2Zr_2O_7$ solid solutions. As shown, all compositions are almost fully dense and therefore, in the following discussions, we can comfortably eliminate the effects of porosity on thermal conductivity.

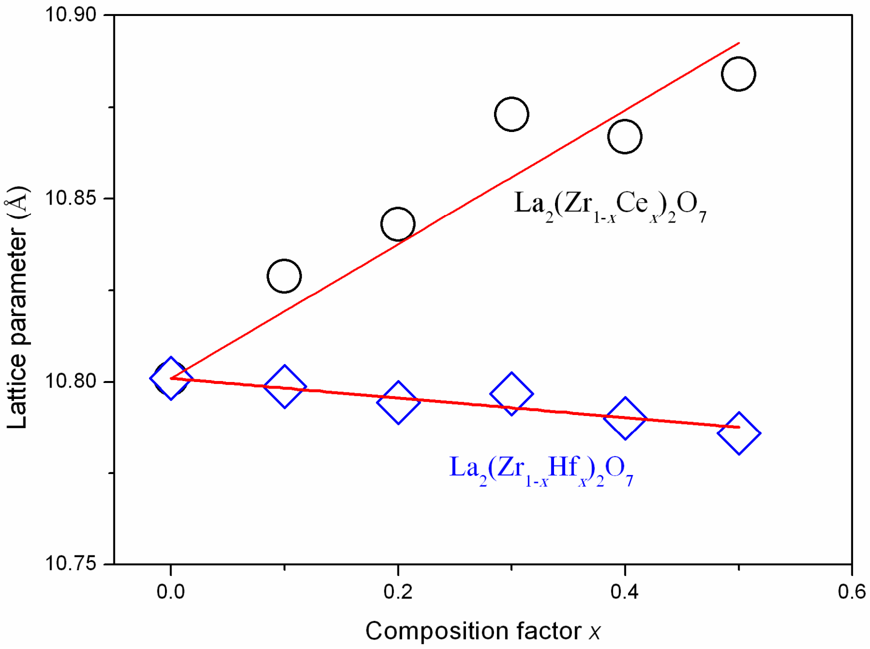

Fig.5.2 Measured lattice parameters of $La_2(Zr_{1-x}B_x)_2O_7$ (B=Hf, Ce, $0 \leq x \leq 0.5$) solid solutions

Table 5.3

Lattice parameters, theoretical, Archimedes' and relative densities of $La_2(Zr_{1-x}B_x)_2O_7$ (B=Hf, Ce, $0 \leq x \leq 0.5$) solid solutions.

	Lattice parameter (Å)	Theoretical density (g/cm^3)	Archimedes' density (g/cm^3)	Relative density (%)
$La_2(Zr_{0.5}Hf_{0.5})_2O_7$	10.7860	6.982	6.968±0.012	99.8
$La_2(Zr_{0.6}Hf_{0.4})_2O_7$	10.7900	6.790	6.744±0.008	99.3
$La_2(Zr_{0.7}Hf_{0.3})_2O_7$	10.7968	6.593	6.587±0.006	99.9
$La_2(Zr_{0.8}Hf_{0.2})_2O_7$	10.7944	6.413	6.333±0.006	98.8
$La_2(Zr_{0.9}Hf_{0.1})_2O_7$	10.7988	6.221	6.146±0.010	98.8
$La_2Zr_2O_7$	10.8010	6.033	6.040±0.020	100
$La_2(Zr_{0.9}Ce_{0.1})_2O_7$	10.8288	6.089	6.016±0.004	98.8
$La_2(Zr_{0.8}Ce_{0.2})_2O_7$	10.843	6.167	6.130±0.010	99.4
$La_2(Zr_{0.7}Ce_{0.3})_2O_7$	10.873	6.217	6.180±0.011	99.4

5.3.3 Thermal diffusivity/conductivity

Fig.5.3 shows thermal diffusivities (D) and thermal conductivities (k) of single-phased Hf^{4+}/Ce^{4+} doped $La_2Zr_2O_7$ pyrochlores against composition factor x and we can find the following features. Generally, the k of $La_2Zr_2O_7$ can be more significantly reduced by

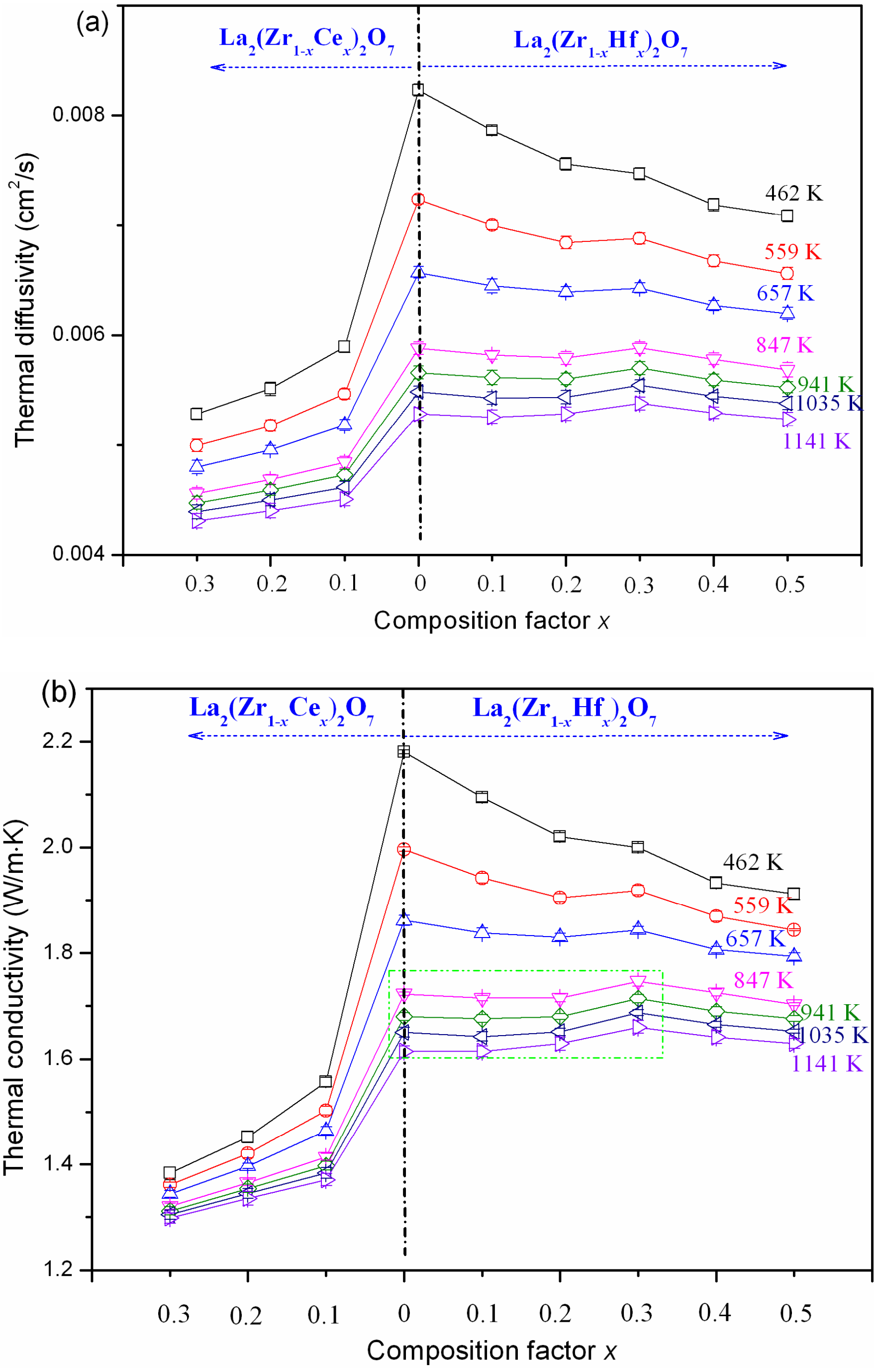

Fig.5.3 The plots of thermal diffusivity (a) and thermal conductivity (b) of Hf/Ce-doped $La_2Zr_2O_7$ with the single pyrochlore phase versus dopant content x.

introducing a 21% bigger Ce^{4+} than a 96% heavier Hf^{4+}. Furthermore, the *k* of $La_2(Zr_{1-x}Ce_x)_2O_7$ pyrochlores exhibits a more evident temperature-independent trend than that of $La_2(Zr_{1-x}Hf_x)_2O_7$. The Hf^{4+} dopant, whose mass is almost the twice of its host Zr^{4+}, appears to be ineffective in reducing *k* particularly at high temperatures, which is in contradiction to the findings in Ref.[9]. Even more surprisingly, the *k* of $La_2(Zr_{1-x}Hf_x)_2O_7$ exhibits a slightly rising trend with an increase of *x* from 0.1 to 0.3 at temperature range of 941 to 1141 K (see the rectangular box in the Fig.5.3(b)), which severely challenges the general belief that *k* can be reduced by incorporating impurity atoms.

5.4 Discussions

The major findings of this chapter are: (1) by introducing a 96% heavier Hf^{4+} and a 21% larger Ce^{4+} dopant to the B-sites of $La_2Zr_2O_7$, we find $La_2(Zr_{1-x}Ce_x)_2O_7$ pyrochlores show a much lower $k_{\min}$ and a more temperature-independent trend than $La_2(Zr_{1-x}Hf_x)_2O_7$, suggesting the importance of the size of substituting ions to both high temperature plateau $k_{\min}$ and the *k*-*T* curve flatness parameter α; (2) the similar or even higher *k* of $La_2(Zr_{1-x}Hf_x)_2O_7$ at elevated temperatures than its end member severely challenges the conclusion reached by Ref.[9, 21] that $k_{\min}$ is proportional to $\overline{M}^{-0.5}$. In this part, based on the established phonon defect scattering model, two parameters, α and $k_{\min}$, are proposed to govern heat transport at low and high temperatures respectively. Secondly, we clarify that the size difference (Δr) between the guest and host ions determines the parameter α (or the strength of phonon-point defect interaction). Thirdly, we find that a great absolute size, in addition to a heavy mass, of substituting ions effectively reduces the plateau $k_{\min}$, attributed to (1) that $k_{\min}$ is proportional to $\sqrt{E/\overline{M}}$ and (2) that a larger guest ion substituted tends to effectively weaken a bond showing typical ionic character and thus reduce *E*. Lastly, in accordance with the model, we suggest that, the interstitials rather than the substitutional atoms are responsible for the temperature-independent *k* in $Y(Yb)Nb(Ta)O_4$ doped zirconia found in Ref.[5,6].

5.4.1 The defect scattering model: the *k*-T curve flatness α and plateau $k_{\min}$

Have taken into account that phonon mean free path (Λ) cannot decrease indefinitely but reach the minimum value ($\Lambda_{\min}$), the *k* of dielectric solid solutions with solute atoms at different temperatures can be described as the following equation:

$$k=\frac{A}{3T_1}+\frac{A}{T^{0.5}}\frac{2}{\sqrt{\alpha}}\arctan\sqrt{-\frac{1}{2}+\frac{1}{2}\sqrt{1+\alpha\frac{T_1}{T^2}}}-\frac{2\sqrt{2}}{3}\frac{A\sqrt{T_1}}{T^{1.5}}\frac{1}{(1+\sqrt{1+\alpha\frac{T_1}{T^2}})^{1.5}} \tag{5.2}$$

in which *A* is:

$$A=\frac{\overline{M}v^3}{45a^2\gamma^2}\propto\frac{E^{1.5}a^{2.5}}{\overline{M}^{0.5}\gamma^{3.5}} \qquad (5.3);$$

T_1 is a characteristic temperature, under which phonon mean free path never reaches its minimal value ($\Lambda_{\min}$) and has the form:

$$T_1=0.0074\frac{\overline{M}v^2a}{k_B\Lambda_{\min}\gamma^2}\propto\frac{Ea^3}{\gamma^3} \qquad (5.4);$$

and α is a parameter describing the flatness of *k*-*T* curves and has the following form:

$$\alpha=0.544\frac{c_PN\overline{M}v^2\Gamma}{k_B\gamma^2}\propto\frac{c_PNEa^3\Gamma}{\gamma^3} \qquad (5.5).$$

In the above expressions, $\overline{M}$ and a^3 are the average atomic mass and volume; *v* is the sound velocity; γ is the Grüneisen parameter; *E* is the Young’s modulus; c_P is the point defect concentration; *N* is the number of atoms per unit cell; and k_B is the Boltzmann constant.

From Eq.(5.2), the thermal conductivity of a dielectric material at different temperatures (the *k*-*T* curve) is determined by the following two parameters. Firstly, the parameter α determines the flatness of *k*-*T* curves and a very large value of α tends to give a rather flat *k*-*T* curve (i.e. a temperature- independent *k*). Secondly, $A/3T_1$ controls the magnitude of the plateau $k_{\min}$, which is characteristic of most ceramics and can be attained above a critical temperature. By combining Eq.(5.3) and Eq.(5.4), we can get the following expression:

$$k_{\min} = \frac{A}{3T_1} = \xi\sqrt{\frac{E}{a\overline{M}\gamma}} \tag{5.6}$$

in which ξ is a constant. These two parameters, α and $k_{\min}$, related respectively to phonon-point defect scattering and phonon-phonon Umklapp scattering, are responsible for the *k* reduction at low and high temperatures respectively. However, the majority of the previous studies rely on the scattering coefficient Γ (which is related to α through Eq.(5.5)) to discuss the *k* reduction effect, with $k_{\min}$ being rarely touched on. In fact, the plateau $k_{\min}$ is extremely important to heat transport not only at high temperatures but also throughout the whole temperature range, as schematically illustrated the following scenarios in Fig.5.4.

Firstly, while a large α (or Γ) is usually thought to be accompanied by a low $k_{\min}$ (Fig.5.4 (a)), an often neglected scenario is the co-existence of both a large α (or Γ) and a high $k_{\min}$ (Fig.5.4 (b)), because, as α and $k_{\min}$ are independent parameters and determined by different parameters (see Eq.(5.5) for α and Eq.(5.6) for $k_{\min}$), a larger α (i.e. stronger phonon-point defect scattering) does not necessarily mean a lower $k_{\min}$ (i.e. stronger phonon-phonon Umklapp scattering). The latter scenario is intriguing because a larger *k* is expected despite of a stronger phonon-point defect interaction, suggesting a significant

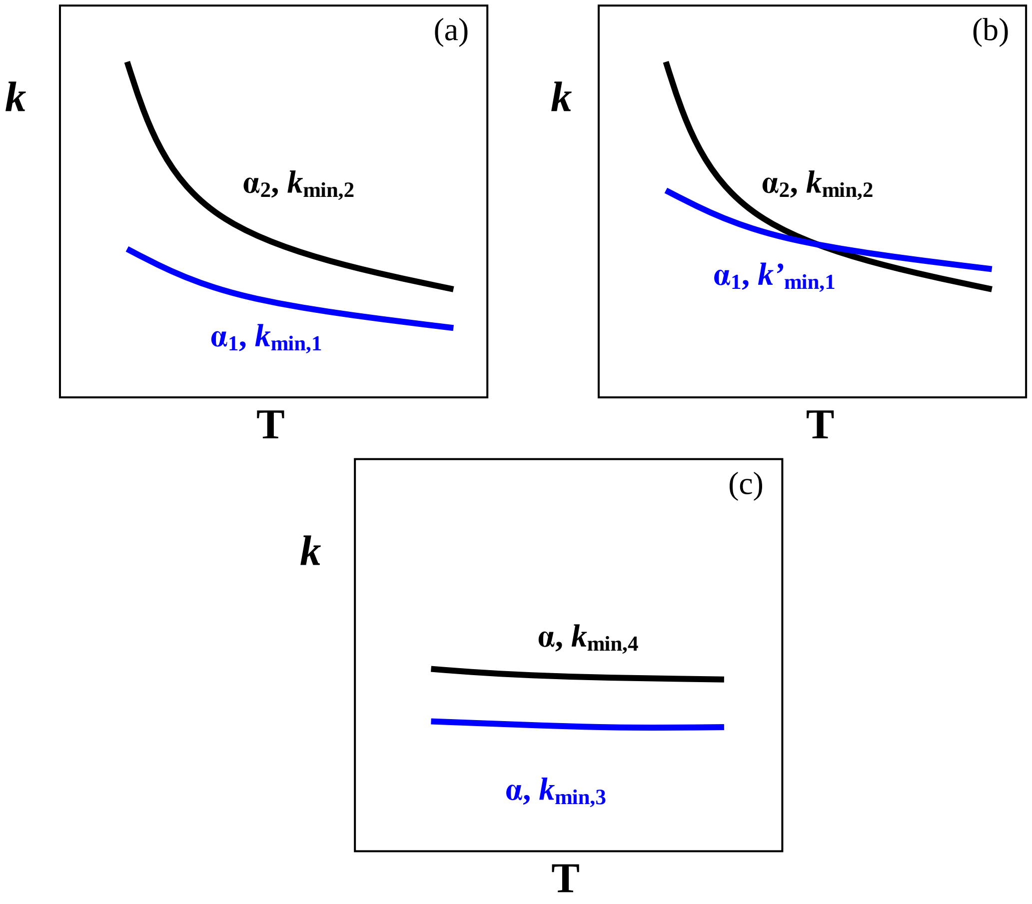

Fig.5.4 Schematic drawings of three sets of k-T curves: (a) $\alpha_2 < \alpha_1$, $k_{min,1} < k_{min,2}$; (b) $\alpha_2 < \alpha_1$, $k_{min,2} < k'_{min,1}$; and (c) α is extremely large and , $k_{min,3} < k_{min,4}$, stressing the importance of k_{min} on heat transport.

role played by k_{min}. Secondly, the parameter k_{min} becomes overwhelmingly important for those dielectric materials with strong phonon scatterers present, such as oxygen vacancies, rattlers, etc. Those strong phonon scatterers usually render their host lattice an extremely large flatness parameter α and thus a temperature-insensitive k, as illustrated in Fig.5.4 (c). As a result, this temperature-independent k is apparently determined by k_{min}.

Interestingly, the Hf^{4+} doped $La_2Zr_2O_7$ pyrochlore sets a good example of the scenario as envisaged in Fig.5.4 (b) whilst Ce^{4+} doped $La_2Zr_2O_7$ fits the situation described in Fig.5.4 (a), as shown in Fig.5.5. On the basis of Eq.(5.2), the dashed lines in Fig.5.5 are the fitting curves of the measured k at different temperatures for Hf^{4+}/Ce^{4+} doped $La_2Zr_2O_7$ pyrochlores, employing A and α as adjustable parameters. The fitting results and some relevant parameters are listed in Table 5.4. As shown, these two different dopants generate distinct curve plateau (k_{min}) and curve flatness (α) parameters. A larger substitutional atom (Ce^{4+}) is more effective than a much heavier one (Hf^{4+}) in strengthening the phonon-point defect scattering (i.e. increasing the parameter α). Furthermore, the Ce^{4+} substitutional ion appears to have a role in reducing the curve plateau k_{min}. The distinct effects of Hf^{4+} and Ce^{4+} dopants on α and k_{min} are going to be presented in 5.4.2 and 5.4.3 by exploring the prevailing factors contributing to α and k_{min} respectively.

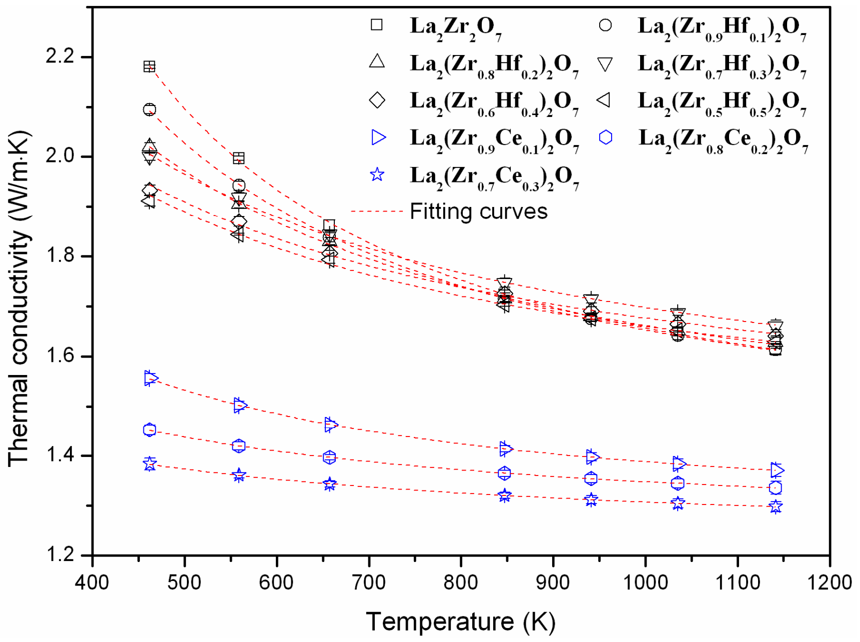

Fig.5.5 The temperature dependence of thermal conductivities for Hf/Ce doped $La_2Zr_2O_7$ solid solutions with a single pyrochlore phase. Dashed lines are fitted curves according to Eq.(5.2).

Table 5.4

Some basic parameters of $La_2(Zr_{1-x}B_x)_2O_7$ (B=Hf, Ce) with single pyrochlore phase and the fitting results (A and α).

x	Lattice parameter (Å)	a (Å)	c_P	ρ (10^3kg· m^{-3})	$\overline{M}$ (10^{-26}kg)	E^a (GPa)	v^b (m/s)	γ^c	A_{min} (Å)^c	T_1^d (K)	A^e (W/m)	α^e
0.5(Hf)	10.786	2.425	0.0833	6.982	9.956	208±5	4742	2.07	3.135	216.5	936	18914
0.4(Hf)	10.789	2.426	0.0667	6.790	9.693	205±4	4774	2.07	3.135	213.8	929	14000
0.3(Hf)	10.792	2.426	0.05	6.593	9.429	202±6	4809	2.07	3.135	211	924	10132
0.2(Hf)	10.756	2.427	0.0333	6.413	9.166	193±5	4763	2.07	3.135	203.6	872	5144
0.1(Hf)	10.799	2.428	0.0167	6.221	8.902	185±7	4742	2.07	3.135	196.1	835	1466
0	10.801	2.428	0	6.033	8.642	180±5	4746	2.07	3.135	189^e	818^e	/
0.1(Ce)	10.829	2.435	0.0167	6.089	8.787	123±6	3927	2.07	3.135	131.6	505	9231
0.2(Ce)	10.869	2.444	0.0333	6.167	8.934	119±4	3816	2.07	3.135	126.8	480	32313
0.3(Ce)	10.873	2.445	0.05	6.217	9.082	116±5	3753	2.07	3.135	124.7	462	63854

[a] measured by micro-indentation; [b] calculated by $v = 0.87\sqrt{E/\rho}$; [c] Results from Chapter 3; [d] calculated by Eq.(5.4); [e] fitting results

5.4.2 The controlling factor(s) of the *k*-T curve flatness parameter α: Δ*r* and *x*

The curve flatness parameter α reveals the strength of phonon-point defect interactions and, according to Eq.(5.5), depends on the scattering coefficient Γ. According to [13] and [14], the scattering coefficient of $La_2(Zr_{1-x}B_x)_2O_7$ (B=Hf, Ce) can be calculated by:

$$\Gamma = \frac{2}{12}\left(\frac{M_{Zr,B}}{\overline{\overline{M}}}\right)^2 x(1-x)\left[\left(\frac{M_B - M_{Zr}}{xM_B + (1-x)M_{Zr}}\right)^2 + \varepsilon\left(\frac{r_B - r_{Zr}}{xr_B + (1-x)r_{Zr}}\right)^2\right] \qquad (5.7)$$

in which M_B, M_{Zr} denote atomic mass of guest (Hf^{4+} or Ce^{4+}) and host (Zr^{4+}) cations; $M_{Zr,B}$ is the average atomic mass on B-sites; r_B, r_{Zr} denote cationic size of guest (Hf^{4+} or Ce^{4+}) and host (Zr^{4+}) cations; and ε is an adjustable parameter related to the Grüneisen parameter (γ) and the Poisson's ratio (μ) and has the following form[1,3]:

$$\varepsilon = 2\left(\frac{2\gamma}{\sqrt{6}} + \frac{6.4}{3}\gamma\frac{1+\mu}{1-\mu}\right)^2 \qquad (5.8).$$

Depending on the value of γ and μ, ε has a value ranging from several dozens to several hundreds. Therefore, the size difference term in Eq.(5.7), multiplying by ε, is believed to override the mass difference term and dominate its contribution to Γ.

Fig.5.6 (a) and (b) are the plots of scattering coefficient Γ and curve flatness parameter α against composition factor *x*, which are calculated by Eq.(5.7) and the combination of Eqs.(5.5) and (5.7) respectively. Fig.5.6 unambiguously demonstrates that, the Γ and α produced by the 21% bigger Ce^{4+} dopants are much larger than those by the 96% heavier Hf^{4+} dopants, arguably due to the very large value of ε (~200) for $La_2Zr_2O_7$ [17], confirming the dominant contribution of size difference (Δ*r*) between host and guest ions to point defect-phonon scattering. Another feature of Γ-*x* and α-*x* curves is that, they show a similar 'Λ' trend for both Hf^{4+} and Ce^{4+} doped $La_2Zr_2O_7$ pyrochlores, reaching

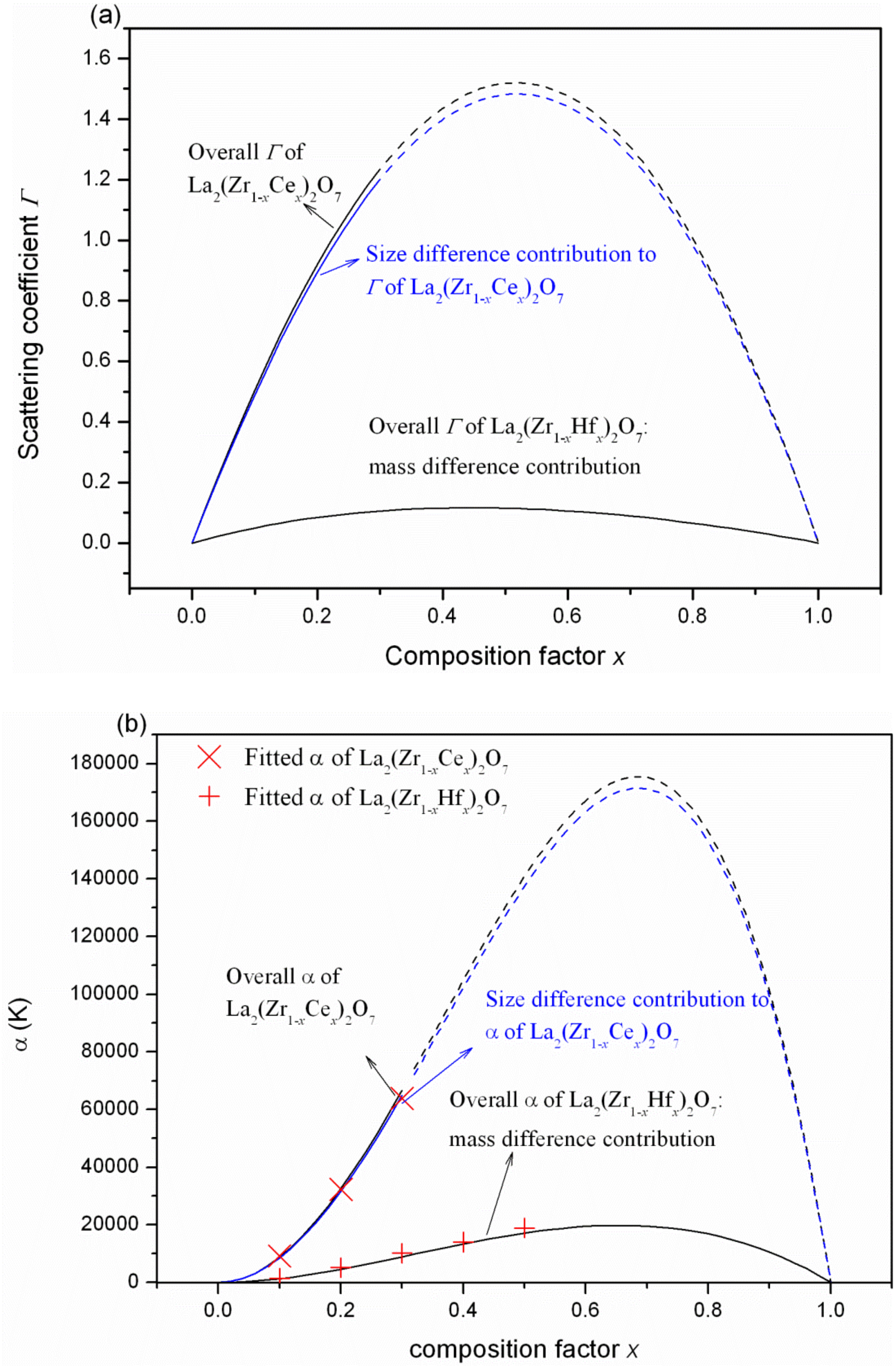

Fig.5.6 The plots of scattering coefficient *Γ* (a) and *α* (b) versus composition factor *x* for $La_2(Zr_{1-x}Hf_x)_2O_7$ (solid lines) and $La_2(Zr_{1-x}Ce_x)_2O_7$ (partial solid ($x \leq 0.3$) and partial dashed ($x > 0.3$) lines).

their peaks at about x = 0.5 and $\frac{2}{3}$ respectively, due to the respective $x(1-x)$ (for Γ, see Eq.(5.7)) and $x^2(1-x)$ (for α, see Eqs.(5.5) and (5.7)) dependence on x. This suggests that α (or Γ) strongly relies on the composition factor x and that point defect-phonon interaction tends to be strongest near the intermediate composition ($x = 0.5$).

5.4.3 The role of substitutional defects and their dominant factor(s) on the *k*-T curve plateau $k_{\min}$

According to Eq.(5.6), there are four parameters contributing to $k_{\min}$: E, $a, \overline{M}$ and γ. The variations of E, $a, \overline{M}$ and γ with the doping content of Hf^{4+} and Ce^{4+} (i.e. the composition factor x) are shown in Fig.5.7, from which the following features can be seen. Firstly, a and γ are relatively invariable at different compositions; whereas, while $\overline{M}$ varies linearly with x, E varies particularly dramatically upon the doping of substitutional defects. It appears that the variations of E almost determine the changing tendency of $k_{\min}$ for different compositions. Secondly, the introduction of Ce^{4+} to the $La_2Zr_2O_7$ lattice results in (1) a steady increase of $\overline{M}$ and (2) a consistent decrease of E. As both the increase of $\overline{M}$ and the decrease of E favor the decrease of $k_{\min}$, $La_2(Zr_{1-x}Ce_x)_2O_7$ pyrochlores exhibit a steady decrease of $k_{\min}$. By contrast, the doping of Hf^{4+} to the $La_2Zr_2O_7$ lattice results in a steady increase of both $\overline{M}$ and E. As the increases of $\overline{M}$ and E have an opposite effect on $k_{\min}$, $k_{\min}$ is instead determined by the relative changing extents of E and $\overline{M}$, the former of which is marginally bigger than the latter for $La_2(Zr_{1-x}Hf_x)_2O_7$ pyrochlores.

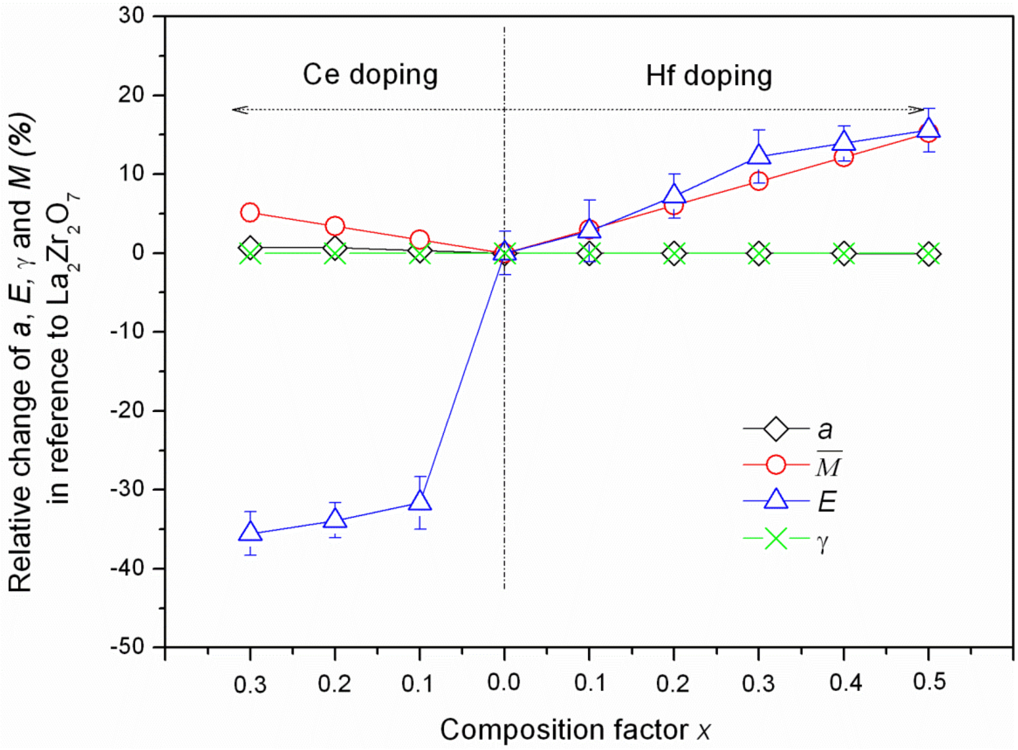

Fig.5.7 The relative change (in percentage) of a, E, γ and $\overline{M}$ of Ce doped $La_2Zr_2O_7$ (left) and Hf doped $La_2Zr_2O_7$ (right) in reference to the end member $La_2Zr_2O_7$.

5.4.3.1 The effect of B-site substitutional defects on elastic modulus E of $La_2Zr_2O_7$ pyrochlores

Owing to the specific pyrochlore structure of $La_2Zr_2O_7$ that the corner-sharing ZrO_6 octahedra make up its backbone with La^{3+} ions filling the interstices [22-24], its overall stiffness is determined by the Zr-O bonds. Hence, the substitution of Zr^{4+} by Hf^{4+} or Ce^{4+}, resulting in the switch of Zr-O bonds to Hf (or Ce)-O bonds, has some influences on E, particularly for those ionic bonds. These B-O bonds (B = Zr, Hf, Ce) show typical ionic character in pyrochlores, which is affirmed by Pruneda et al [25]. For ionic bonds, the E is defined by:

$$E = \frac{(n-1)M_a z^+ z^- e^2}{4\pi\varepsilon_0 r_0^4} \propto \frac{M_a}{r_0^4} \tag{5.9}$$

in which n is the Born exponent, M_a is the Madelung constant, z is the charge on each ion, e is the elementary charge, ε_0 is the permittivity of free space, and r_0 is the inter-ionic spacing. According to Eq.(5.9), for the isovalent doping of Zr^{4+} by Hf^{4+} and Ce^{4+}, the E of pyrochlore solid solutions is determined predominantly by r_0 and subsidiarily by M_a.

Firstly, owing to the strong fourth-power dependence of E on r_0, the E of pyrochlores is very sensitive to the change of the ionic B-O bond length (i.e. the inter-ionic spacing r_0). For the ionic bond, its length depends on the ionic sizes of ions that form this bond. As a result, the B-O ionic bond length in pyrochlores relies on the ionic size of B-site ions. As shown in Fig.5.1 (b), the elongation or shortening of the B-O bonds in $La_2(Zr_{1-x}B_x)_2O_7$ (B = Hf, Ce) with x can be reflected by the shifts of Raman bands located near 394 cm^{-1} that corresponds to the B-O stretching mode. This band of $La_2(Zr_{1-x}Ce_x)_2O_7$ clearly shifts to low frequencies (i.e. red shifts), suggestive of the Zr(Ce)-O bond elongation and thereby yielding a bigger r_0; whereas, the same band of $La_2(Zr_{1-x}Hf_x)_2O_7$ shifts to high frequencies (i.e. blue shifts) with a smaller magnitude, indicative of the Zr(Hf)-O bond shortening and thereby producing a smaller r_0. Therefore, as long as B-O bonds exhibit ionic character, a larger ion on B-sites tends to effectively reduce the stiffness of the pyrochlore structure. This conclusion is consistent with the simulation work by Schelling et al [26] on $A_2B_2O_7$ pyrochlores with a series of A- and B-site ions. However, the premise of the above discussion is that B-O bonds show a typical ionic feature, or in other words, an adequately large electronegativity difference between B and O. For those B-site elements exhibiting nonmetal features, such as Pb, Mo, Ge, Sn etc, B-O bonds show instead a covalent character and their bond strengths are not determined by the size of B-site ions.

Secondly, the variations of the Madelung constant M_a with x play a subsidiary role in the change of E at different compositions. According to [11,27], the doping of Hf^{4+} to the $La_2Zr_2O_7$ lattice drives the long-range ordering of pyrochlores and thus increases the Madelung constant M_a; whereas, the doping of Ce^{4+} disturbs the ordering of pyrochlores (with the broadened bands in Fig.5.1(b) as a proof) and thus reduces M_a. Therefore, besides the strong dependence of E on the ionic bond length r_0, the variation of M_a with x leads to a further decrease (or increase) of E for Ce (or Hf) doped $La_2Zr_2O_7$ pyrochlores respectively, as the changing tendencies of both r_0 and M_a favor the decrease of E for $La_2(Zr_{1-x}Ce_x)_2O_7$ relative to those being against the decrease of E for $La_2(Zr_{1-x}Hf_x)_2O_7$.

5.4.3.2 The effect of substitutional defects on a, $\overline{M}$ and γ of $La_2Zr_2O_7$ pyrochlores

The effect of substitutional defects on average atomic mass ($\overline{M}$) or volume (a^3) is straightforward. That is, $\overline{M}$ and a^3 usually have a linear dependence on the doping content x with the former usually having a larger slope than the latter. However, the influence of impurity ions on the Grüneisen parameter γ (or the lattice anharmonicity) is not so apparent. The substitution of Zr^{4+} by the Hf^{4+} and Ce^{4+} ions in $La_2Zr_2O_7$ pyrochlores has negligible influence on γ, with the following three pieces of evidence. Firstly, while the increase of lattice anharmonicity usually relies on, according to Chapter 4, a repulsive lattice force, there appears to be no such force present in Hf/Ce doped $La_2Zr_2O_7$. Secondly, the fact that ZrO_2, HfO_2 and CeO_2, the latter two of which can be regarded as Hf/Ce doped ZrO_2, have a similar Grüneisen parameter γ (~1.4) [4] suggests that a similar γ is expected as well in Hf/Ce doped $La_2Zr_2O_7$ pyrochlores as in $La_2Zr_2O_7$. Thirdly, by employing the same γ value (~2.07) for different compositions of Hf^{4+}/Ce^{4+} doped $La_2Zr_2O_7$ pyrochlores as that of the end member, a good linear regression of $k_{\min}$

against $\sqrt{E/a\overline{M}\gamma}$ can be found in Fig.5.8, further confirming the negligible effect on γ by doping Hf^{4+} and Ce^{4+} to the $La_2Zr_2O_7$ pyrochlore lattice. The constant ξ in Eq.(5.6) has been obtained as $2.476\times10^{-23} m^2\cdot kg\cdot s^{-2}$ through the process of the linear regression.

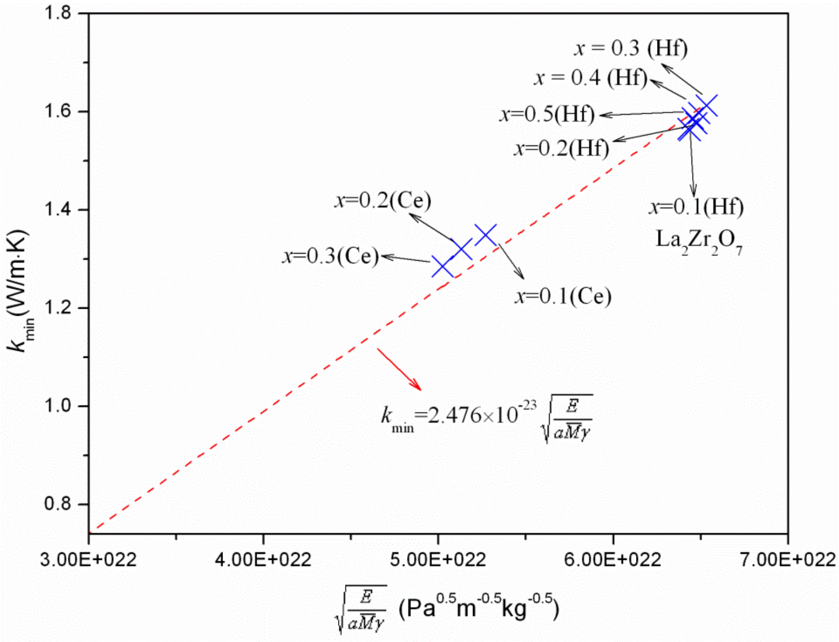

Fig.5.8 The plot of k_{min} versus $\sqrt{E/a\overline{M}\gamma}$ of Hf/Ce doped $La_2Zr_2O_7$ pyrochlore solid solutions shows a decent linear regression (dashed line), yielding ξ in Eq.(5.6) to be around $2.476\times10^{-23} m^2\cdot kg\cdot s^{-2}$.

To sum up, from the above discussions, the prevailing factor controlling the k_{min} of Hf/Ce doped $La_2Zr_2O_7$ pyrochlores is the elastic modulus E, attributable to its remarkable dependence on the ionic size of B ions in the B-O bonds that show typical ionic character. In fact, the ignorance of the variations of E by doping in Ref.[9] has brought in the question why the lowest k does not emerge at the composition with the largest $\overline{M}$ in hafnia doped 6.55 and 12.3YSZ. As envisaged in Fig.5.4 (c), owing to the presence of heavy oxygen vacancies in the lattice, α is large enough to generate a temperature-independent k and the heat transport can then be discussed in the plateau regime. Similar as Hf^{4+} doped $La_2Zr_2O_7$, an increasing tendency of E is predicted in Hf doped YSZ when the smaller Hf^{4+} ions are progressively substituting the Zr^{4+} hosts, which is supported by the finding of Ibegazene et al [28] that the doping of 4.5YSZ by Hf^{4+} markedly increased E. As a result, determined by $E/\overline{M}$ instead of $1/\overline{M}$ alone, the lowest k can understandably emerge at some composition with the lowest $E/\overline{M}$ instead of the heaviest average atomic mass.

5.4.4 Substitutional defects or interstitials: comments on co-doped zirconia

The findings by Raghavan [5] and Shen [6] that substitutional defects could result in a temperature-independent k are clearly against our preceding discussions. Their discussions are built on the assumption that all dopants resided in substitutional positions, evidenced by the reduced ionic conductivity because of the annihilation of oxygen vacancies by co-doping zirconia with trivalent ($Y/YbO_{1.5}$) and pentavalent ($Nb/TaO_{2.5}$) oxides. However, it is still an open question whether Nb^{5+}/Ta^{5+} ions to occupy substitutional or interstitial sites in the YSZ lattice. The evidence favoring the occupation of Nb^{5+}/Ta^{5+} ions on the interstitial sites is threefold, arising from Raman spectra[29-31], a dramatic reduced elastic modulus[5,31-33] and a temperature-independent thermal conductivity of $YNb(Ta)O_4$ co-doped zirconia respectively.

Firstly, Ref.[29] found the selective shifts of Raman bands (representing Zr-O stretching mode) towards high frequencies, attributed to the pentavalent ions (Nb^{5+}/Ta^{5+}) occupying the tetrahedral interstitial sites instead of the dodecahedral substitutional sites, because Nb^{5+}/Ta^{5+} ions have a much smaller ionic size (0.48 Å) given their occupation at the tetrahedral sites and thereby a higher bond strength and the consequent blue shifts. Secondly, the dramatic reduction of elastic moduli (E) for YNb/TaO_4 co-doped zirconia [5, 31-33] suggests Nb^{5+}/Ta^{5+} residing in the interstitial sites, because, according to

Kanigel et al [34], interstitials tend to cause a marked reduction of *E*. Otherwise, if they occupied the dodecahedral substitutional sites, a larger *E* is predicted according to Eq.(5.9) because of a smaller size (0.69 Å) of guest ions than their host Zr^{4+}(0.78 Å)[15].

Thirdly, the interstitials can well explain the temperature-independent *k* in co-doped zirconia, with the following proofs that support them as strong phonon scatterers. Firstly, according to Eq.(5.2), the temperature-insensitive *k* relies on a large Γ and α, which are dependent on the relative mass/size difference between the guest and host ions. Interstitials are reciprocal to vacancies and are as capable as vacancies to generate an adequately large Γ and α that make *k* temperature-independent, because either the “guest” for vacancies or the “host” for interstitials is vacant and therefore a maximized mass or size difference can be achieved. Secondly, the findings by Cahill et al [35,36] confirmed the strong phonon-scattering nature of interstitials, whose presence in a lattice usually induces a glass-like thermal conductivity. The high similarity of interstitials with oxygen vacancies lies not only on their dramatic capability of flattening *k*-*T* curves, but also on their marked competence of reducing plateau $k_{\min}$ by means of reducing *E* in combination with raising lattice anharmonicity. The reduced *E* and increased γ by interstitials are probably attributed to the same reason proposed to account for those found in oxygen vacancies (i.e. the strong repulsive lattice force introduced), which is however out of the scope in the current study.

5.5 Conclusions

The effects of substitutional defects on *k* have been studied by introducing a 96% heavier Hf^{4+} and a 21% larger Ce^{4+} to the B-sites of the $La_2Zr_2O_7$ pyrochlore lattice. The size rather than mass difference between the host and guest ions dominates the phonon scattering by point defects and thus determines the flatness of *k*-*T* curves (or the *k* reduction at relatively low temperatures). By contrast, the absolute mass/size of guest ions, particularly the latter, determines the high temperature plateau $k_{\min}$, owing to that $k_{\min}$ is proportional to $\sqrt{E/a\overline{M}\gamma}$ and that a larger dopant ion introduced tends to dramatically weaken a bond that shows a typical ionic character. Therefore, compared to those strong phonon scatterers (such as vacancies, interstitials, rattlers, etc.) that usually render the host lattice a temperature-independent *k* but do not necessarily generate a lower $k_{\min}$, it is suggested by the current study that $k_{\min}$ can instead be effectively reduced by doping a substitutional atom that is heavy and large. The insights gained into the high temperature plateau regime provide a guideline for the selection and design of a low-*k* material for high temperature applications.

References

[1] P.G. Klemens. *The scattering of low-frequency lattice waves by static imperfections*. Proc Phys Soc Lond A **68** (1955) 1113-1128.

[2] H. Lehmann, D. Pitzer, G. Pracht, R. Vassen and D. Stover. *Thermal conductivity and thermal expansion coefficients of the lanthanum rare-earth-element zirconate system*. J Am Ceram Soc **86** (2003) 1338-1344.

[3] C.L.Wan, W. Pan, Q. Xu, Y.X. Qin, J.D. Wang, Z.X. Qu and M.H. Fang. *Effect of point defects on the thermal transport properties of* $(La_xGd_{1-x})_2Zr_2O_7$*: experiment and theoretical model*. Phys Rev B **74** (2006) 144109 1-9.

[4] F. Yang, X. F. Zhao and P. Xiao. *The effects of temperature and composition on the thermal conductivities of* $[(ZrO_2)_{1-x}(CeO_2)_x]_{0.92}(Y_2O_3)_{0.08}$ $(0 \leq x \leq 1)$ *solid solutions*. Acta Mater **60** (2012) 914-922.

[5] S. Raghavan, H. Wang, W.D. Porter, R.B. Dinwiddie and M.J. Mayo. *Thermal properties of zirconia co-doped with trivalent and pentavalent oxides*. Acta Mater **49** (2001) 169-179.

[6] Y. Shen, R.M. Leckie, C.G. Levi and D.R. Clarke. *Low thermal conductivity without oxygen vacancies in equimolar* $YO_{1.5}$ + $TaO_{2.5}$ *and* $YbO_{1.5}$ + $TaO_{2.5}$*-stabilized tetragonal zirconia ceramics*. Acta Mater **58** (2010) 4424-4431.

[7] P.G. Klemens. *Phonon scattering by oxygen vacancies in ceramics*. Phys B **263** (1999) 102-104.

[8] P.G. Klemens and M. Gell. *Thermal conductivity of thermal barrier coatings*. Mater Sci Eng A-Struct **245** (1998) 143-149.

[9] M.R. Winter and D.R. Clarke. *Thermal conductivity of yttria-stabilized zirconia-hafnia solid solutions*. Acta Mater **54** (2006) 5051-5059.

[10] X.W. Song, M. Xie, R.D. Mu, F. Zhou, G.X. Jia and S.L. An. *Influence of the partial substitution of* Y_2O_3 *with* Ln_2O_3 *(Ln = Nd, Sm, Gd) on the phase structure and thermophysical properties of* ZrO_2-Nb_2O_5-Y_2O_3 *ceramics*. Acta Mater **59** (2011) 3895-3902.

[11] C.L. Wan, Z.X. Qu, A.B. Du and W. Pan. *Influence of B site substituent Ti on the structure and thermophysical properties of $A_2B_2O_7$-type pyrochlore $Gd_2Zr_2O_7$.* Acta Mater **57** (2009) 4782-4789.

[12] P.K. Schelling. *Thermal conductivity of A-site doped pyrochlore oxides studied by molecular-dynamics simulation*. Comp Mater Sci **48** (2010) 336-342.

[13] G.A. Slack. *Thermal conductivity of MgO, Al_2O_3, $MgAl_2O_4$ and Fe_3O_4 crystals from 3 K to 300 K.* Phys Rev **126** (1962) 427-441.

[14] B. Abeles. *Lattice thermal conductivity of disordered semiconductor alloys at high temperatures*. Phys Rev **131** (1963) 1906-1911.

[15] R.D. Shannon. *Revised effective ionic radii and systematic studies of interatomic distances in Halides and Chalcogenides*. Acta Cryst **A32** (1976) 751-767.

[16] D. R. Clarke. Materials selection guidelines for low thermal conductivity thermal barrier coatings. Surf Coat Tech **163-164** (2003) 67-74.

[17] W.D. Kingery, J. Francl, R.L. Coble and T. Vasilos. *Thermal conductivity: X. data for several pure oxide materials corrected to zero porosity*. J Am Ceram Soc **37** (1954) 107-110.

[18] I. Barin. *Thermochemical Data of Pure Substances*, 3rd ed., Weinheim: VCH, 1995.

[19] C.L. Wan, Z.X. Qu, A.B. Du and W. Pan. *Order-disorder transition and unconventional thermal conductivities of the $(Sm_{1-x}Yb_x)_2Zr_2O_7$ series*. J Am Ceram Soc **94** (2011) 592-596.

[20] C.J. Wang, W.Z. Huang, Y. Wang, Y.L. Cheng, B.L. Zou, X.Z. Fan, J.L. Yang and X.Q. Cao. *Synthesis of monodispersed $La_2Ce_2O_7$ nanocrystals via hydrothermal method: a study of crystal growth and sintering behavior*. Int J Refract Met H **31** (2012) 242-246.

[21] R. Mevrel, J.-C. Laizet, A. Azzopardi, B. Leclercq, M. Poulain, O.Lavigne and D. Demange. *Thermal diffusivity and conductivity of $Zr_{1-x}Y_xO_{2-x/2}$ (x = 0, 0.084 and 0.179) single crystals*. J Eur Ceram Soc **24** (2004) 3081-3089.

[22] M.A. Subramanian, G. Aravamudan and G.V. Subba Rao. *Oxide pyrochlores- A review*. Prog Solid St Chem **15** (1983) 55-143.

[23] B. Liu, J.Y. Wang, F.Z. Li and Y.C. Zhou. *Theoretical elastic stiffness, structural stability and thermal conductivity of $La_2T_2O_7$ (T = Ge, Ti, Sn, Zr, Hf) pyrochlore*. Acta Mater **58** (2010) 4369-4377.

[24] F.X. Zhang, B. Manoun, S.K. Saxena and C.S. Zha. *Structure change of pyrochlore $Sm_2Ti_2O_7$ at high pressures*. Appl Phys Lett **86** (2005) 181906 1-3.

[25] J.M. Pruneda and E. Artacho. *First-principles study of structure, elastic, and bonding properties of pyrochlores*. Phys Rev B **72** (2005) 085107-1-8.

[26] P.K. Schelling, S.R. Phillpot and R.W. Grimes. *Optimum pyrochlore compositions for low thermal conductivity*. Phil Mag Lett **84** (2004) 127-137.

[27] K.V. Govindan Kutty, S. Rajagopalan, C.K. Mathews and U.V. Varadaraju. *Thermal expansion behavior of some rare-earth-oxide pyrochlores*. Mater Res Bull **29** (1994) 759-766.

[28] H. Ibegazene, S. Alperine and C. Diot. *Yttria-stabilized hafnia-zirconia thermal barrier coatings- the influence of hafnia addition on TBC structure and high-temperature behavior*. J Mater Sci **30** (1995) 938-951.

[29] D.J. Kim, H.J. Jung and I.S. Yang. *Raman spectroscopy of tetragonal zirconia solid solutions*. J Am Ceram Soc **76** (1993) 2106-2108.

[30] D.J. Kim, P.F. Becher and C.R. Hubbard. *Effect of Nb_2O_5 alloying on thermal expansion anisotropy of 2 mol-percent Y_2O_3-stabilized tetragonal ZrO_2*. J Am Ceram Soc **76** (1993) 2904-2908.

[31] D.J. Kim and T.Y. Tien. *Phase-stability and physical-properties of cubic and tetragonal ZrO_2 in the system ZrO_2-Y_2O_3-Ta_2O_5*. J Am Ceram Soc **74** (1991) 3061-3065.

[32] A. Bhattachaya, V. Shklover, K. Kunze, W. Steurer. *Effect of 7YSZ on the long term stability of $YTaO_4$ doped ZrO_2 system*. J Euro Ceram Soc **31** (2011) 2897-2901.

[33] X. Huang and Q. Yang. *Effects of co-doping on elastic modulus for zirconia based ternary ceramic materials*. Mater Sci Tech-Lond **24** (2008) 751-755.

[34] A. Kanigel, J. Adler and E. Polturak. *Influence of point defects on the shear elastic coefficients and on the melting temperature of copper*. Int J Mod Phys C **12** (2001)727-737.

[35] D.G. Cahill and R.O. Pohl. *Low-energy excitations in the mixed-crystal* $Ba_{1-x}La_xF_{2+x}$. Phys Rev B **39** (1989) 10477-10480.

[36] D.G. Cahill, S.K. Watson and R.O. Pohl. *Lower limit to the thermal conductivity of disordered crystals*. Phys Rev B Condens Matter **46** (1992) 6131-6140.

Chapter 6 The phase stability and toughening effect of 3Y-TZP dispersed in the lanthanum zirconate ceramics

6.1 Introduction

While lanthanum zirconate ($La_2Zr_2O_7$, LZ) is postulated as an alternative thermal barrier coating (TBC) topcoat material due to its excellent thermal resistance[1, 2], its application has been largely hindered by penalties in durability [3], attributable to the following two reasons. Firstly, the LZ topcoat and its underlying thermally grown oxide (TGO) are thermochemically instable and prone to react with each other and form a porous $LaAlO_3$ interphase, which therefore compromises the integrity of the TBC system and eventually the protective function of TGO [3]. Secondly, the premature failure of LZ topcoat arises from a combination of the low toughness [4] and the low thermal expansion coefficient (TEC) [5] of $La_2Zr_2O_7$. Upon cycling, the lower TEC of LZ topcoat causes a higher thermal stress, which can more easily initiate cracks and promote their growth, thereby leading to an earlier failure [6].

The thermochemical instability problem of LZ and TGO has been solved by inserting an inert layer, typically yttria-stabilized zirconia (YSZ), between LZ topcoats and the TGO layer [7]. Acting as a diffusion barrier layer as well as a stress alleviation layer, the YSZ transition layer has considerably improved the cyclic life of LZ TBC [8]. It is conceivable that the durability of LZ TBC would be further improved if the LZ ceramics could be toughened. The poor fracture toughness of the LZ ceramic originates from its lack of energy dissipative mechanisms and the essence of various toughening methods is to introduce different energy dissipative channels. Li et al [9] introduced a ferroelastic phase $BaTiO_3$ to LZ ceramics, attempting to make exploitation of domain wall switching as an energy dissipation pathway. They achieved a 24% increase of fracture toughness. In another study, they incorporated YAG ($Y_3Al_5O_{12}$) nano-phase to the LZ ceramic matrix and obtained a similar improvement of fracture toughness [10]. However, both $BaTiO_3$ and YAG are reactive with LZ matrix at high temperatures and thus not a desirable second phase inclusion for LZ ceramics.

Therefore, as an ideal toughening phase of LZ matrix, it should meet the following requirements. Firstly it should be thermochemically compatible with LZ ceramics; secondly, it should include a certain energy dissipative channels (or have high intrinsic fracture toughness); and finally it should have a desirably low thermal conductivity, since the toughening of LZ ceramics should not be at the expense of its thermally insulative capability. As a conventional TBC topcoat material, YSZ essentially satisfies all the above requirements and is therefore a qualified candidate as a toughening phase of LZ ceramics. In this study, the commercially available 3 mol %-Y_2O_3 tetragonal zirconia polycrystals (3Y-TZP, or 3YSZ) has been selected as the toughening agent. The slightly lower stabilizer concentration than that of the standard YSZ TBC (about 3.8 mol %-Y_2O_3 stabilized zirconia [4]) results in a larger tetragonality (*c*/*a* ratio) [11], upon which the high temperature ferroelastic toughening mechanism is dependent. The initial envisagement of this study is to homogeneously disperse the non-transferable tetragonal-prime (*t*') 3YSZ particulates in the LZ matrix so as to exploit the ferroelastic domain reorientation as a toughening mechanism. However, the introduced 3Y-TZP particulates are transformable especially with a low addition of the dispersive second phase, attributed not only to the equilibrium route of sample preparations by sintering but also to the thermal residual stress arisen from the TEC misfit between 3YSZ dispersive particulates and the LZ matrix. The 3YSZ particulates dispersed in LZ ceramics can greatly improve the fracture toughness of the matrix and the primary toughening mechanisms originate from the phase transformation of the dispersive 3YSZ second phases as well as the residual compressive stress within the LZ matrix.

6.2 Experiments

The $La_2Zr_2O_7$ polycrystalline powders were prepared by the co-precipitation technique as described in Chapter 3. Prior to mixing, 3 mol % yttria stabilized zirconia powders (Pi-Kem, 99% pure) were heated at 1423 K for 6 h so as to homogenize the composition to yield single tetragonal phase. Then, x3YSZ/(1-x)$La_2Zr_2O_7$ composite powders (where x is volume fraction and $x = 0.1, 0.2, 0.3, 0.4, 0.5$) were mixed by attrition milling (12 h, 300 r.p.m.) with zirconia media in distilled water. The received powder suspensions were subsequently freeze-dried to yield aggregation-free powders. Such powders were cold-pressed into disc compacts (12 mm in diameter and 2-3 mm in height) and sintered at 1673 K for 2 h.

The phase compositions of the composite ceramics were identified by an X-ray diffraction (XRD) facility (Philips X'Pert) with CuK_α radiation and a Raman optical microprobe system (Renishaw 1000, UK) with the 514 nm line of an argon laser. Densities of the sintered bodies were measured by the Archimedes' method. The microstructure details of the specimens were examined via scanning electron microscope (SEM, Philips XL 30) on the polished and thermally-etched surfaces. The fracture toughness was investigated by the indentation method at room temperature using a diamond Vickers indenter with a loading time 15 s at a constant load 50 N. Since the indenting of low-toughness materials with a Vickers indenter generally forms a half-penny crack [12, 13], the fracture toughness (K_{Ic}) is calculated by the following equation [14]:

$$K_{Ic} = 0.016\sqrt{\frac{E}{H}}\frac{P}{c^{1.5}} \tag{6.1}$$

where E is the elastic modulus, H is the hardness, P is the applied load and c is the sum of crack length (l) and one half of the indenter imprint diagonal (a).

6.3 Results

6.3.1 Phase compositions

Fig.6.1 (a) shows the XRD patterns of 3YSZ/LZ ceramic composites in comparison with the raw powders of each constituent. While LZ and 3YSZ exhibit single pyrochlore (*P*) and tetragonal (*t*) phase respectively, the monoclinic (*m*) phase of zirconia can be detected for the composites with a lower 3YSZ addition (i.e. the volume proportion $x \leq 0.3$), evidenced by the presence of the characteristic reflections at 31.5° for the monoclinic phase. However, when the volume fraction of 3YSZ exceeds 0.3, the monoclinic phase is absent and the introduced 3YSZ purely exhibits the tetragonal phase. The Raman spectra, Fig.6.1 (b) further confirm the prior findings. The characteristic bands of monoclinic zirconia, the doublets near 180 cm^{-1}, are present for the volume fraction x lower than 0.3 but absent for x above 0.3.

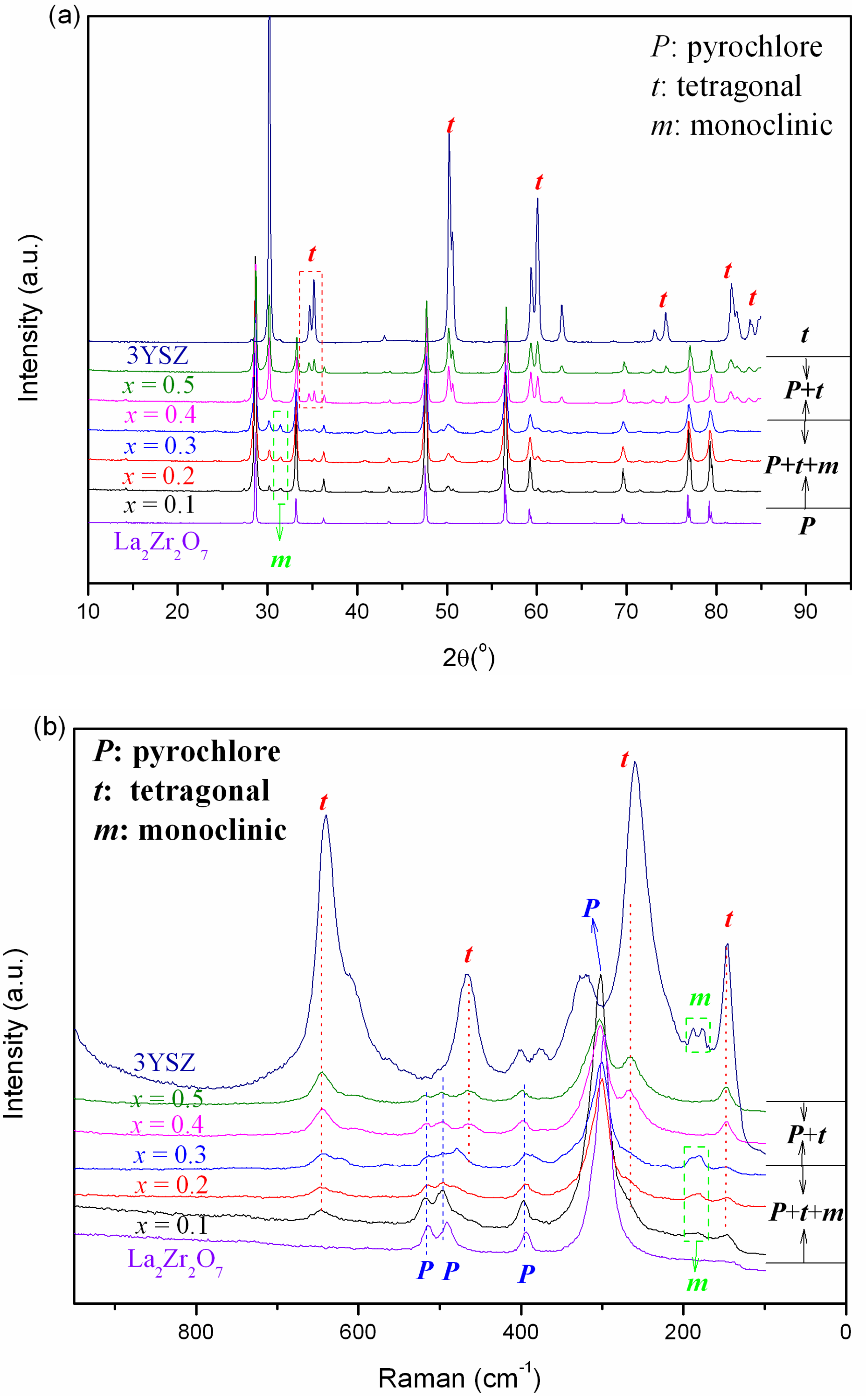

Fig.6.1 XRD patterns (a) and Raman spectra (b) of 3YSZ and LZ powders and 3YSZ/LZ composite ceramics. Partial tetragonal phases of 3YSZ has transformed to monoclinic for a lower addition of 3YSZ ($x \leq 0.3$).

6.3.2 Density and microstructure

Fig.6.2 shows the theoretical and measured densities of 3YSZ/LZ ceramic composites. The densities of the ceramic composites with a high addition of 3YSZ ($x > 0.3$) are consistent with those predicted by the mixing law. By contrast, the densities of those composites with a relatively low addition of 3YSZ ($x \leq 0.3$) are steadily lower than the values predicted from the mixing law, attributed to the partial transformation of the heavier tetragonal phases to the lighter monoclinic phases, which further confirms the simultaneous phase transformation upon cooling for those composites with a lower inclusion of 3YSZ particulates.

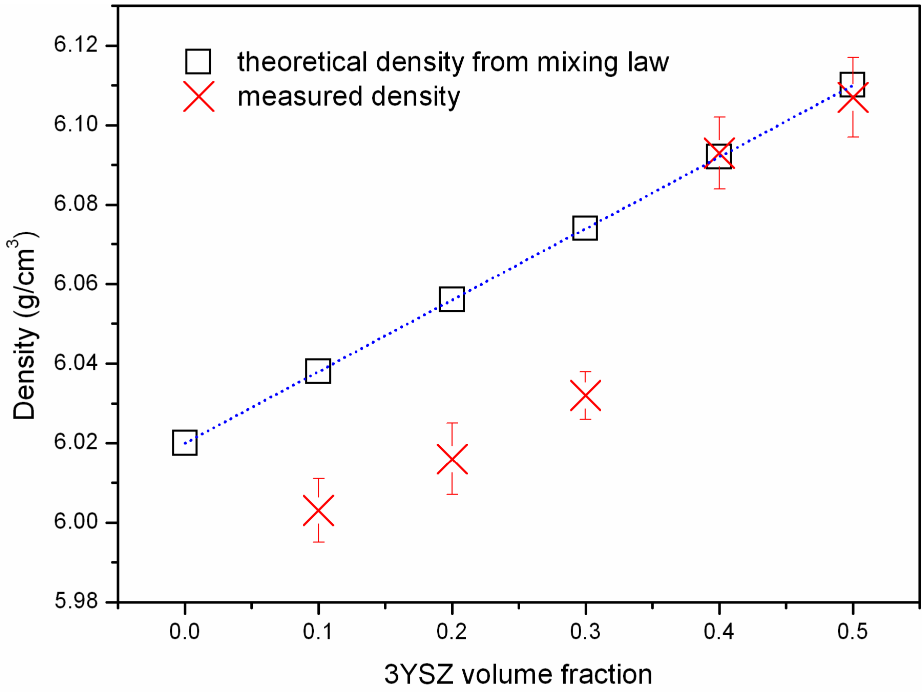

Fig.6.2 The theoretical and measured densities of 3YSZ/LZ composite ceramics. The theoretical density of the ceramic composite is calculated from the mixing law of its constituents (LZ: 6.02 g/cm^3; 3YSZ: 6.20 g/cm^3).

Fig.6.3 shows the microstructural evolution of 3YSZ/LZ ceramic composites with an increase of 3YSZ volume fraction x. As shown, for a low addition of 3YSZ, the second phases are rather homogeneously distributed in the LZ matrix; whereas, for a high inclusion of 3YSZ, the aggregations of 3YSZ sub-micron particulates are dispersed in the matrix. The grains of LZ matrix are around 1 to 2 μm, much bigger than those of the dispersing 3YSZ phases, which are 300 to 400 nm for the composites with a smaller x ($x \leq 0.3$) but slightly smaller (200 to 300 nm) for those with a higher x ($x = 0.4$ and 0.5).

6.3.3 Mechanical properties

Fig.6.4 (a) shows the measured elastic modulus E and hardness H from micro-indentation. Due to the higher E and H of the 3YSZ dispersive phases, the E and H of 3YSZ/LZ ceramic composites increase linearly with x, as shown the linear regressions of E and H versus x. Fig.6.4 (b) exhibits the fracture toughness K_{Ic} of 3YSZ toughened LZ composites. While the single cubic pyrochlore $La_2Zr_2O_7$ has a rather low fracture toughness (about 1.2 $MPa{\cdot}m^{0.5}$) [6], the additions of 3YSZ dramatically improve its fracture toughness. Depending on the amount introduced of the dispersive 3YSZ phases, the K_{Ic} improvement can be reached from about 32% for 10vol% 3YSZ/LZ to 135% for 50vol% 3YSZ/LZ ceramic composites.

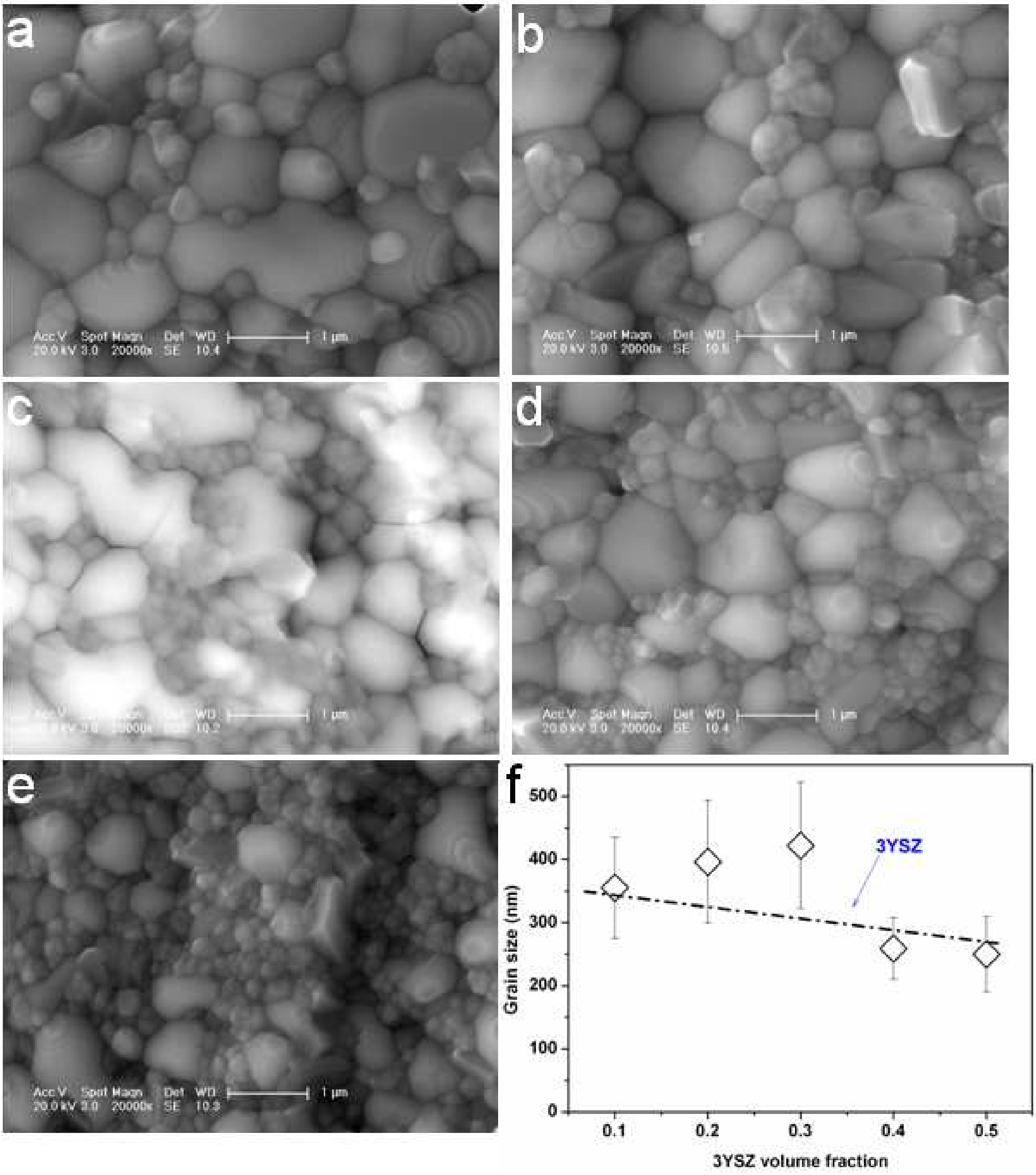

Fig.6.3 Scanning Electron Microscope (SEM) images of 3YSZ/LZ composite ceramics: (a) to (e) are corresponding to 3YSZ volume fraction x = 0.1, 0.2, 0.3, 0.4 and 0.5 respectively. (f) represents the average grain size of the dispersive 3YSZ second phases.

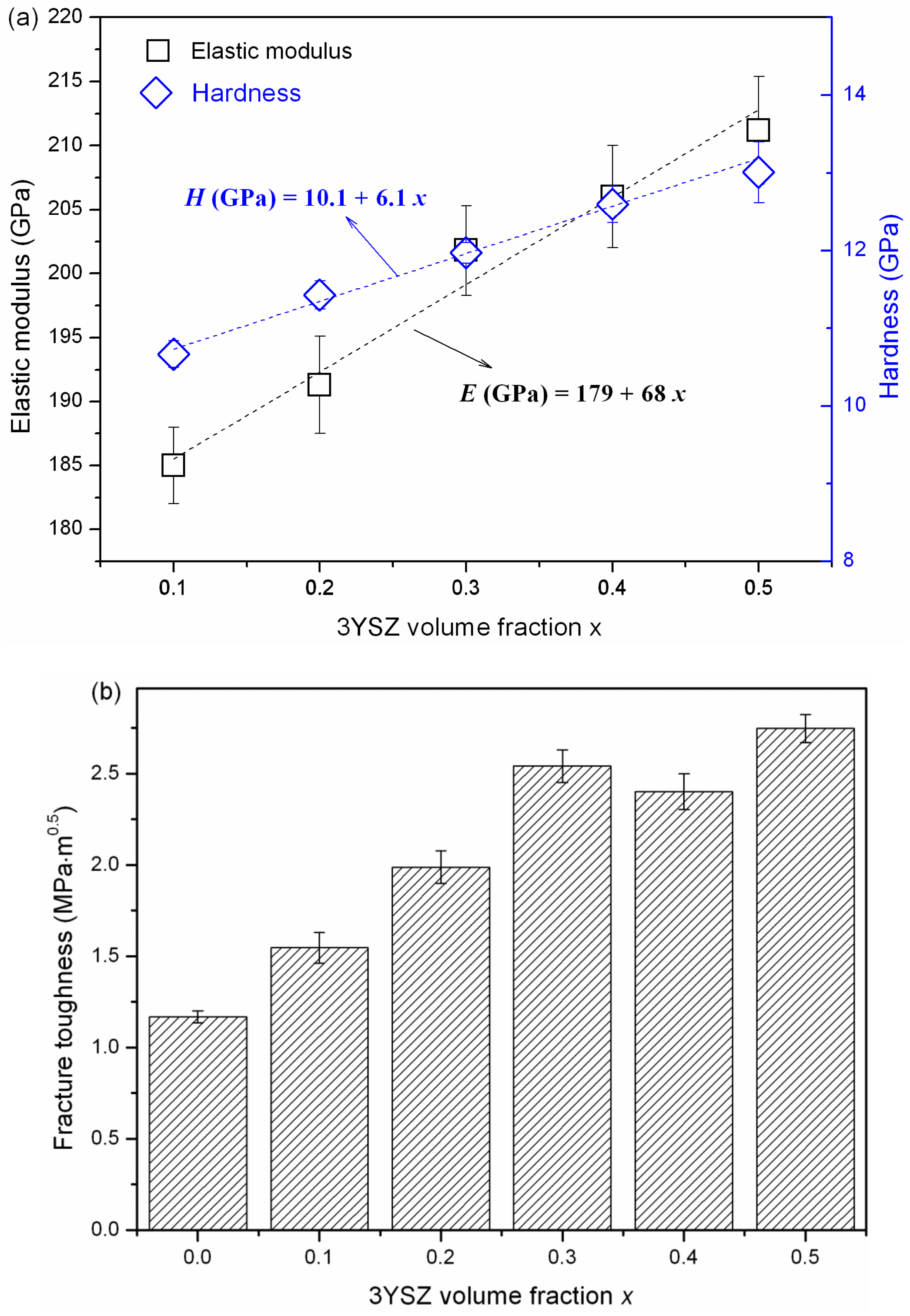

Fig.6.4 The elastic modulus *E* and hardness *H* (a) and the fracture toughness (b) of 3YSZ/LZ ceramic composites at different 3YSZ volume fraction *x*

6.4 Discussions

The findings of this study are twofold. Firstly, deviated from our initial expectation, the dispersive phases of tetragonal 3YSZ (*t*-3YSZ) tend to transform simultaneously to monoclinic phase upon cooling for the low inclusion of the 3YSZ second phase. By contrast, beyond a critical volume fraction of 3YSZ, the simultaneous phase transformation is absent and 3Y-TZP can maintain its tetragonal phase. Secondly, regardless of the presence or absence of simultaneous *t-m* transformation, the dispersive 3YSZ phases generally greatly improve the fracture toughness of LZ ceramics. In the following parts, we first identify the underlying reason(s) resulting in the different *t-m* transformation behaviours at different 3YSZ inclusion levels. Secondly, we investigate the primary toughening mechanism(s) in *t*-3YSZ/LZ ceramic composites.

6.4.1 The destabilizing effect of LZ matrix on dispersive 3Y-TZP

Several factors affect the martensitic *t-m* transformation of zirconia, including the composition (solute type and concentration), temperature, the grain size and the stress state, etc [15, 16]. The former two factors can be eliminated, because the type and amount of the stabilizer for the dispersive 3YSZ are fixed and the processing temperatures of all samples are kept constant. Furthermore, as shown in Fig.6.3 (f), no dramatic grain size differences of the 3YSZ dispersive second phases can be found among the different *t*-3YSZ/LZ ceramic composites. As a result, the destabilization of the dispersive 3Y-TZP second phases can only be ascribed to the variations of stress within the dispersive 3YSZ particulates.

Since the thermal expansion coefficient (TEC) of the dispersive 3YSZ (α_p = 10.8×10^{-6} K^{-1}) [17] is higher than that of the LZ matrix (α_m = 8.6×10^{-6} K^{-1}) [18, 19], upon cooling from the sintering temperature (1673 K) down to room temperature, a tensile and compressive stress has been respectively generated in the dispersive 3YSZ particulates and the LZ matrix. According to Ref.[20], the average residual stress $\langle\sigma\rangle_p$ in the dispersive 3YSZ particulates and the average compressive stress $\langle\sigma\rangle_m$ in the LZ matrix can be calculated by the following equations:

$$\frac{\langle\sigma\rangle_p}{E_m} = \frac{-2(1-x)\beta(\alpha_p-\alpha_m)(T_R-T_P)}{(1-x)(\beta+2)(1+\nu_m)+3\beta x(1-\nu_m)} \tag{6.2}$$

$$\frac{\langle\sigma\rangle_m}{E_m} = \frac{2x\beta(\alpha_p-\alpha_m)(T_R-T_P)}{(1-x)(\beta+2)(1+\nu_m)+3\beta x(1-\nu_m)} \tag{6.3}$$

$$\text{where} \quad \beta = \frac{1+\nu_m}{1-2\nu_p}\cdot\frac{E_p}{E_m} \tag{6.4}$$

In the above expressions, the subscripts p and m represent the dispersive 3YSZ particulates and LZ matrix respectively; ν is the Poisson's ratio; T_R is the room temperature whilst T_P is the processing (sintering) temperature. Employing $E_p = 220$ GPa [21, 22], $E_m = 180$ GPa (see Table 3.3 in Chapter 3), $\nu_p = 0.30$ [23, 24], $\nu_m = 0.34$ [25], $T_P = 1673$ K, $T_R = 298$ K, $\alpha_p = 10.8\times10^{-6}$ K^{-1} [17] and $\alpha_m = 8.6\times10^{-6}$ K^{-1} [18, 19], the average stress in the dispersive 3YSZ particulates and the LZ matrix can be estimated by Eq.(6.2) and (6.3), as plotted in Fig.6.5. As shown, with an increment of 3YSZ volume fraction, the residual tensile stress in the dispersive 3YSZ particulates decreases linearly, whereas, the residual compressive stress in the LZ matrix increases. Although the tensile stress is regarded as an impetus of the *t-m* transformation [26], there exists a critical tensile stress, only above which can the martensitic transformation be initiated [27].

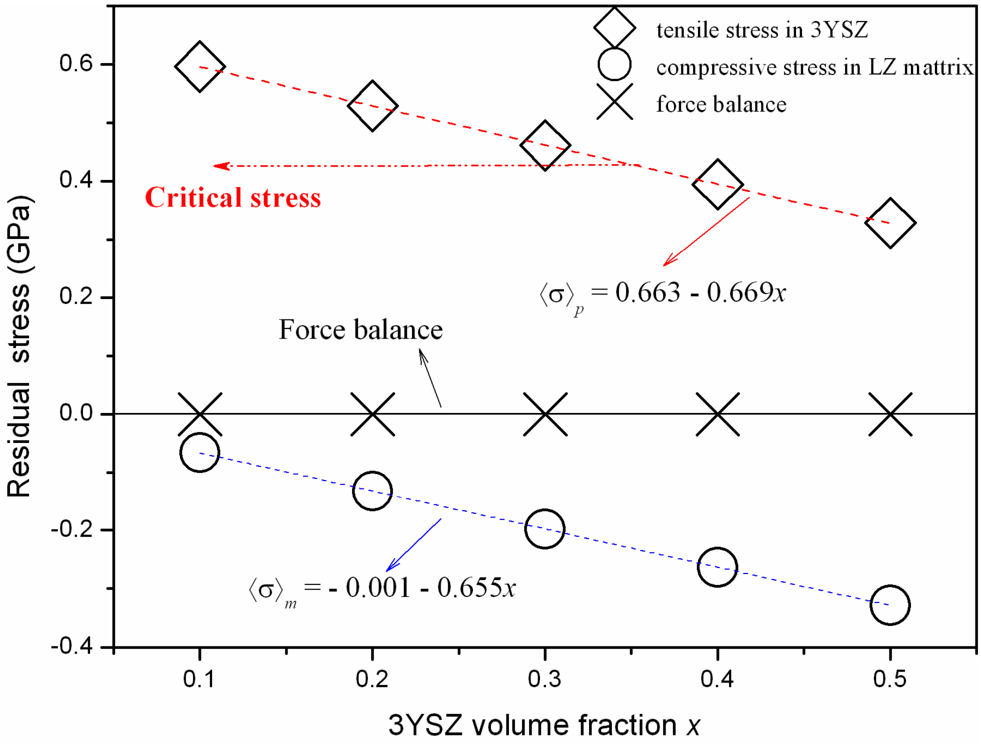

Fig.6.5 The residual tensile and compressive stress in the dispersive 3YSZ particulates and the LZ matrix estimated from Eq.(6.2) and (6.3). The 'force balance', $x\langle\sigma\rangle_p + (1-x)\langle\sigma\rangle_m$ is also included.

Obviously, this critical tensile stress relies on the type and concentration of the stabilizer as well as the grain size of tetragonal zirconia polycrystals. Rauchs et al [28]reported a value of 0.3 GPa for 9 mol % CeO_2 stabilized tetragonal zirconia polycrystals (9Ce-TZP), whereas, Pan et al [27] revealed the critical value of 0.7 GPa for the hot-isostatically pressed 3Y-TZP with rather fine grains. From the striking differences of the simultaneous *t-m* transformation for various 3YSZ inclusion levels: an appearance for ceramic composites with $x \leq 0.3$ whilst an absence for those with $x > 0.3$, we can accordingly infer that, the residual tensile stress within the dispersive 3YSZ particulates of a ceramic composite with x between 0.3 and 0.4 reaches the critical value for the *t-m* transformation of 3Y-TZP, which is about 0.4 GPa in this study, as illustrated in Fig.6.5.

6.4.2 Toughening mechanism(s) of 3YSZ/LZ ceramic composites

The most desirable toughening mechanism we aim to introduce is the ferroelastic toughening, a mechanism which uses grain reorientation as an energy dissipative channel and hence can operate at high temperatures. However, due to the limits of the equilibrium route of sample fabrication by sintering, we have not successfully prepared the metastable tetragonal-prime (*t*') phase full of anti-phase boundaries and twins as produced by the non-equilibrium route such as air plasma spray (APS) or electron-beam physical vapour deposition (EB-PVD); furthermore, as a result of the residual tensile stress within the dispersive 3Y-TZP particulates, the 3Y-TZP even undergoes the simultaneous *t-m* phase transformation upon cooling. Therefore, we can infer that the improvement of fracture toughness by dispersing the 3Y-TZP particulates originates primarily from the *t-m* phase transformation, which is still applicable to those composites with a high addition of 3YSZ particulates, despite of their capabilities of retaining the single tetragonal phase after cooling. As a typical example shown in Fig.6.6, the indentation crack wakes were examined by Raman to detect the trace of monoclinic zirconia on the 40 vol.% *t*-3YSZ toughened LZ ceramic composites. Interestingly, the *m* phase can only be detected immediately on or close to the indentation cracks. This suggests, some tetragonal phases down the wakes of indentation cracks, subjected to an intense tensile stress field at the tips of the propagating cracks, have transformed to the *m* phase. The volume expansion arisen from the *t-m* transformation results in a compressive strain field, which can oppose the crack propagation[15], and consequently, lead to the improvement of fracture toughness. However, because the *t-m* transformation (i) is thermodynamically prohibited at high temperatures; and (ii) involves volume changes which are detrimental to the integrity upon thermal cycling, this toughening mechanism is not favorable for the high temperature applications such as thermal barrier coatings[29]. If the *t*' phase is produced as inclusions in LZ matrix from non-equilibrium routes such as APS or EB-PVD, the toughening mechanisms include (1) the compressive residual stress in LZ matrix, which is applicable to both the current equilibrium *t*-3YSZ/LZ composites from sintering and the non-equilibrium *t*'-3YSZ/LZ composites from industrial routes; and (2) the ferroelastic toughening, despite of its less significance than the phase transformation. These two toughening mechanisms are discussed as follows.

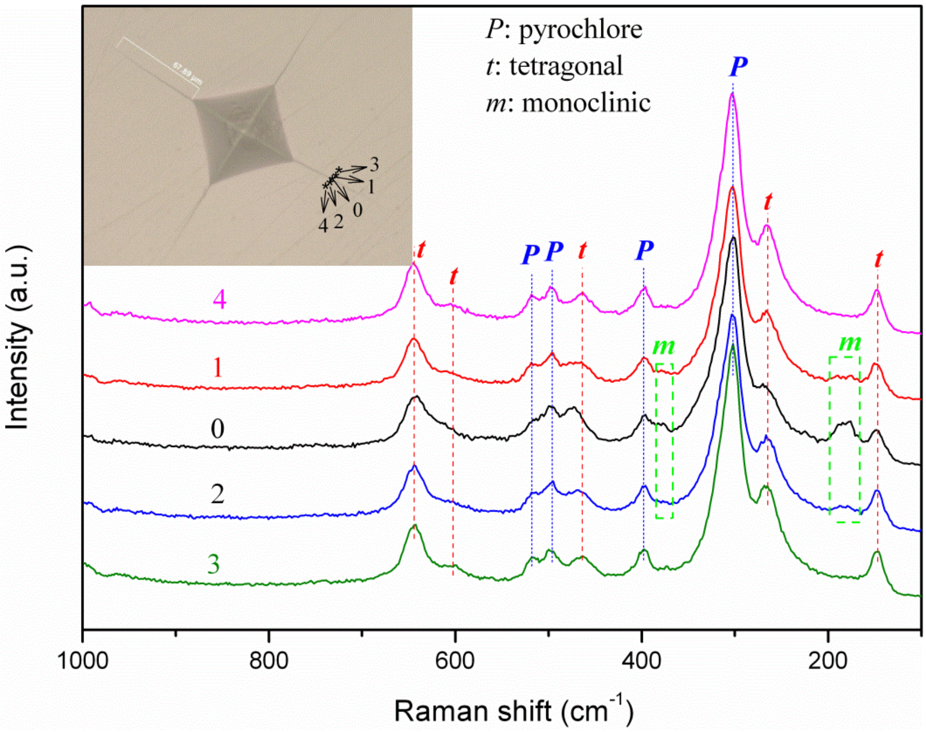

Fig.6.6 The Raman spectra detected immediately on the indentation crack (0), close to the crack (1, 2) and away from cracks (3, 4) after indenting on the 0.4 *t*-3YSZ/0.6 LZ ceramic composites at a load of 50 N. Inset shows the typical optical micrograph of the imprint.

Because the compressive stress can oppose crack propagations, the LZ ceramics can be toughened by the residual compressive stress generated in the LZ matrix by 3YSZ particulates with a higher TEC dispersed in the LZ matrix[20]. Evans et al [30]and Cutler et al[31] developed a model which depicts the improvement of fracture toughness from a periodic compressive residual stress in a particulate-toughened ceramic composite, which has the following form:

$$K_{Ic} = K_{Ic0} + 2\sigma_m\sqrt{\frac{2D}{\pi}} \qquad (6.5),$$

where K_{Ic0} is the intrinsic fracture toughness of the ceramic matrix whereas the latter term represents the improvement due to compressive stress; D is the average particulate spacing; and σ_m is the local residual compressive stress. Employing the calculated average residual stress $\langle\sigma\rangle_m$ from Fig.6.5 and the average spacing of 3YSZ particulates (or their assemblages) from SEM images (Fig.6.3), we can make an estimation of fracture toughness improvement (ΔK_{Ic}(II)) due to the residual compressive stress within the LZ matrix. As shown in Fig.6.7, ΔK_{Ic}(II) increases with an increment of 3YSZ volume fraction x, but it is much smaller than ΔK_{Ic}(I), the toughening contribution from the *t-m* phase transformation. From ΔK_{Ic}(I), based on the simple mixing law and the known K_{Ic} of one constituent LZ (1.2 MPa·$m^{0.5}$), the fracture toughness of the other constituent 3YSZ can be calculated as 4.1±0.4 MPa·$m^{0.5}$ for those composites with volume fraction x = 0.1- 0.3, which have the grain size of 3YSZ around 0.35 μm; and 3.4±0.1 MPa·$m^{0.5}$ for those with x = 0.4- 0.5, which have the grain size of 3YSZ close to 0.25 μm. These K_{Ic} values of 3YSZ agree very well with those reported in Ref.[32], in which a decreasing trend of K_{Ic} can be clearly found with a decline of grain size.

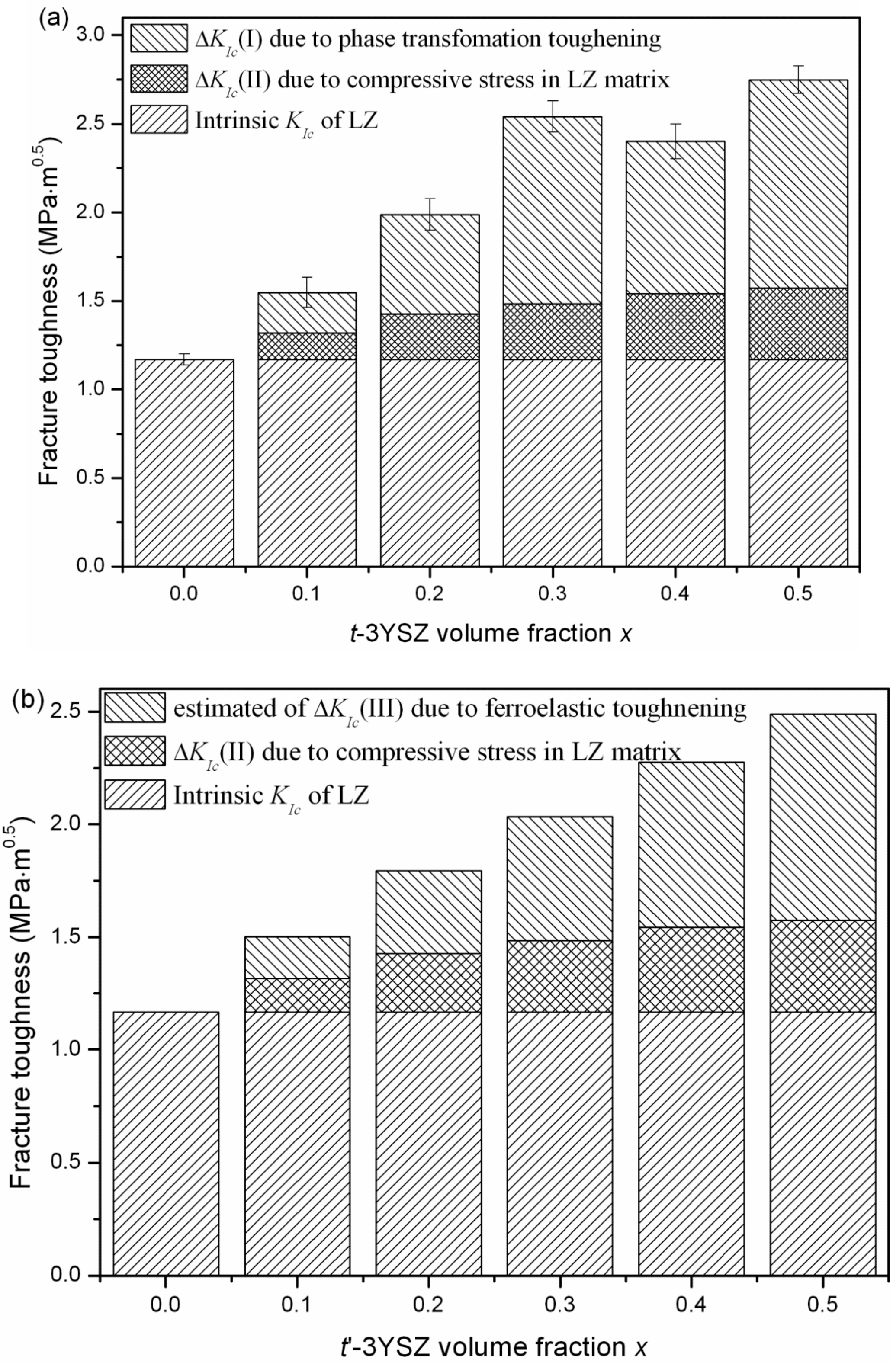

Fig.6.7 The different contributions to the improvement of fracture toughness (ΔK_{Ic}) of (a) *t*-3YSZ/LZ composites (measured in this study) and (b) *t*’-3YSZ/LZ composites (estimated). The ΔK_{Ic}(II), denoting the contribution from the compressive stress in LZ matrix, is calculated from Eq.(6.5); whereas, ΔK_{Ic}(III), representing the contribution from the ferroelastic toughening, is estimated from the mixing law.

Finally, let us evaluate the toughening effect from ferroelastic domain switching given the *t*' phase could be successfully incorporated by the non-equilibrium routes. In the light of the dramatic influence of residual tensile stress on the destabilization of the equilibrium *t* phase, we have to examine its possible destabilizing effect on the non-equilibrium *t*' phase. The *t*' phase as a phase which is thermodynamically instable, its stability (or decomposition) is essentially controlled by the diffusion process, which is determined by the temperature and time. Therefore, no direct connection can be established between residual tensile stress and the destabilization of *t*' phase, suggestive of its meaningfulness by depositing *t*'-YSZ/LZ composite coatings. Similar as the phase transformation toughening which relies on the amount of *t* phases and has demonstrated the applicability of the mixing law on estimating the fracture toughness of *t*-3YSZ/LZ composites, the ferroelastic toughening depends on the amount of ferroelastic phases. Therefore, ΔK_{Ic}(III), the contribution from the ferroelastic toughening for the *t*'-3YSZ/LZ ceramic composites, can be accordingly estimated from the simple mixing law, as shown in Fig.6.7(b), according to the fracture toughness of *t*'-3YSZ (about 3 $\mathrm{MPa \cdot m^{0.5}}$) which is toughened purely from the ferroelastic domain switch[4].

6.5 Conclusions

In order to address the poor fracture toughness of $La_2Zr_2O_7$ ceramics, a factor resulting in the short cyclic life and hence hindering its wide application as a high-temperature TBC topcoat material, the 3mol % Y_2O_3-tetragonal zirconia polycrystals (3Y-TZP) were added and homogeneously dispersed in the LZ matrix so as to improve the fracture toughness. Due to the residual tensile stress within the dispersive 3YSZ second phases as a result of the TEC misfit, the simultaneous *t-m* transformation can be found upon cooling, especially for those with a low inclusion of 3YSZ volume fraction *x*. The existence of a critical volume fraction of 3YSZ, below which the *t*-*m* transformation is detectable, is attributed not only to a declining tendency of tensile stress within the 3YSZ particulates with an increase of x but also to the presence of a critical tensile stress (about 0.4 GPa in this study), only above which can the *t*-*m* transformation be initiated. As a result, the primary toughening mechanisms of the *t*-3YSZ/LZ ceramic composites in this study arise from the phase transformations in the dispersive 3YSZ second phases as well as the residual compressive stress in the LZ matrix. By contrast, the estimated increase of K_{Ic} from both the residual compressive stress toughening and the ferroelastic toughening highlights the great potentials to improve the durability by depositing *t*'-3YSZ/LZ composite TBCs manufactured from high-rate non-equilibrium industrial routes such as APS or EB-PVD.

References

[1] R.Vassen, X.Q. Cao, F.Tietz, D.Basu and D.Stover. *Zirconates as new materials for thermal barrier coatings*. J Am Ceram Soc **83** (2000) 2023-2028.

[2] X.Q. Cao, R. Vassen and D.Stoever. *Ceramic materials for thermal barrier coatings.* J Eur Ceram Soc **24**(2004)1-10.

[3] R.M. Leckie, S. Kramer, M. Ruhle and C.G. Levi. *Thermochemical compatibility between alumina and* ZrO_2*-*$GdO_{3/2}$ *thermal barrier coatings*. Acta Mater **53** (2005) 3281-3292.

[4] A.G. Evans, D.R. Clarke and C.G. Levi. *The influence of oxides on the performance of advanced gas turbines*. J Eur Ceram Soc **28** (2008) 1405-1419.

[5] X.Q. Cao, R. Vassen, F. Tietz and D. Stoever. *New double-ceramic-layer thermal barrier coatings based on zirconia-rare earth composite oxides*. J Eur Ceram Soc **26** (2006) 247-251.

[6] H. Dai, X.H. Zhong, H.Y. Li, Y.F. Zhang, J. Meng and X.Q. Cao. *Thermal stability of double-ceramic-layer thermal barrier coatings with various coating thickness*. Mat Sci Eng A Struct **433** (2006) 1-7.

[7] R. Vassen, A. Stuke and D. Stover. *Recent developments in the field of thermal barrier coatings*. J Therm Spray Technol **18** (2009) 181-186.

[8] R. Vassen, E. Traeger and D. Stover. *New thermal barrier coatings based on pyrochlore/YSZ double-layer systems*. Int J Appl Ceram Tec **1** (2004) 351-361.

[9] J.Y. Li, H. Dai, X.H. Zhong, Y.F. Zhang, X.F. Ma, J. Meng and X.Q. Cao. *Lanthanum zirconate ceramic toughened by* $BaTiO_3$ *secondary phase*. J Alloy Compd **452** (2008) 406-409.

[10] J.Y. Li, H. Dai, X.H. Zhong, Y.F. Zhang, X.F. Ma, J. Meng and X.Q. Cao. *Effect of addition of YAG (*$Y_3Al_5O_{12}$*) nanopowder on the mechanical properties of lanthanum zirconate*. Mat Sci Eng A Struct **460** (2007) 504-508.

[11] J.A. Krogstad, M. Lepple, Y. Gao, D.M. Lipkin and C.G. Levi. *Effect of yttria content on the zirconia unit cell parameters*. J Am Ceram Soc **94** (2011) 4548-4555.

[12] R.D. Dukino and M.V. Swain. *Comparative measurements of indentation fracture toughness with Berkovich and Vickers indenters*. J Am Ceram Soc **75** (1992) 3299-3304.

[13] M.T. Laugier. *Palmqvist indentation toughness in WC-Co composites*. J Mater Sci Lett **6** (1987) 897-900.

[14] G.R. Anstis, P. Chantikul, B.R. Lawn and D.B. Marshall. *A critical evaluation of indentation techniques for measuring fracture toughness: 1. Direct crack measurement*. J Am Ceram Soc **64** (1981) 533-538.

[15] R.H.J. Hannink, P.M. Kelly and B.C. Muddle. *Transformation toughening in zirconia-containing ceramics*. J Am Ceram Soc **83** (2000) 461-487.

[16] B. Basu. *Toughening of yttria-stabilised tetragonal zirconia ceramics*. Int Mater Rev **50** (2005) 239-256.

[17] H. Hayashi, T. Saitou, N. Maruyama, H. Inaba, K. Kawamura and M. Mori. *Thermal expansion coefficient of yttria stabilized zirconia for various yttria contents*. Solid State Ionics **176** (2005) 613-619.

[18]D. Stover, G. Pracht, H. Lehmann, M. Dietrich, J.E. Doring and R. Vassen. *New material concepts for the next generation of plasma-sprayed thermal barrier coatings*. J Therm Spray Technol **13** (2004) 76-83.

[19] X.Q. Cao, R. Vassen, W. Fischer, F. Tietz, W. Jungen and D. Stover. *Lanthanum-cerium oxide as a thermal barrier coating material for high-temperature applications*. Adv Mater **15** (2003) 1438-1442.

[20] M. Taya, S. Hayashi, A.S. Kobayashi and H.S. Yoon. *Toughening of a particulate-reinforced ceramic-matrix composite by thermal residual stress*. J Am Ceram Soc **73** (1990) 1382-1391.

[21] J. Luo and R. Stevens. *Porosity-dependence of elastic moduli and hardness of 3Y-TZP ceramics*. Ceram Int **25** (1999) 281-286.

[22] M. Gust, G. Goo, J. Wolfenstine and M.L. Mecartney. *Influence of amorphous grain-boundary phases on the superplastic behavior of 3-mol-percent-yttria-stabilized tetragonal zirconia polycrystals (3Y-TZP)*. J Am Ceram Soc **76** (1993) 1681-1690.

[23] F. Wakai, S. Sakaguchi and Y. Matsuno. *Superplasticity of yttria-stabilized tetragonal* ZrO_2 *polycrystals*. J Am Ceram Soc **1** (1986) 259-263.

[24] M.L. Mecartney. *Influence of an amorphous 2nd phase on the properties of yttria-stabilized tetragonal zirconia polycrystals (Y-TZP).* J Am Ceram Soc **70** (1987) 54-58.

[25] J. Feng, B. Xiao, C.L. Wan, Z.X. Qu, Z.C. Huang, J.C. Chen, R. Zhou and W. Pan. *Electronic structure, mechanical properties and thermal conductivity of* $Ln_2Zr_2O_7$ *(Ln = La, Pr, Nd, Sm, Eu and Gd) pyrochlore*. Acta Mater **59** (2011) 1742-1760.

[26] J. Chevalier, L. Gremillard and S. Deville. *Low-temperature degradation of zirconia and implications for biomedical implant*. Annu Rev Mater Res **37** (2007) 1-32.

[27] L.S. Pan and S. Horibe. *An in-situ investigation on the critical phase transformation stress of tetragonal zirconia polycrystalline ceramics*. J Mater Sci **31** (1996) 6523-6527.

[28] G. Rauchs, T. Fett, D. Munz and R. Oberacker. *Tetragonal-to-monoclinic phase transformation in* CeO_2*-stabilized zirconia under multiaxial loading*. J Eur Ceram Soc **22** (2002) 841-849.

[29] T.A. Schaedler, R.M. Leckie, S. Kramer, A.G. Evans and C.G. Levi. *Toughening of nontransformable t'-YSZ by addition of titania*. J Am Ceram Soc **90** (2007) 3896-3901.

[30] A.G. Evans, A.H. Heuer and D.L. Porter. *The fracture toughness of ceramics*, in: D.M.R. Taplin (Ed.). *Proceedings of the 4th International Conference on Fracture* (Vol.1). Waterloo: University of Waterloo Press, 1977.

[31] R.A. Cutler and A.V. Virkar. *The effect of binder thickness and residual stresses on the fracture-toughness of cemented carbides*. J Mater Sci **20** (1985) 3557-3573.

[32] B.A. Cottom and M.J. Mayo. *Fracture toughness of nanocrystalline* ZrO_2*-3 mol%*Y_2O_3 *determined by Vickers indentation*. Scripta Mater **34** (1996) 809-814.

Chapter 7 Conclusions and future work

7.1 Conclusions

The improvements of thermally insulating and mechanical properties of $La_2Zr_2O_7$-based pyrochlores as a high-temperature TBC topcoat have been studied in this thesis. The main conclusions are:

(1) There exists a strong phonon scattering source (rattlers) in Y^{3+}-doped $La_2Zr_2O_7$ pyrochlore solid solution, which can be confirmed by the anomalously large ε values obtained from the fitting of k-T curves. The effect of rattlers on k is to dramatically flatten k-T curves, or even make k glass-like when adequate rattlers present.

(2) The rattlers are those smaller Y^{3+} cations residing in the oversized oxygen AO_8 cages formed by the six O1 outward movements in pyrochlore structure. Their presence is strongly dependent on: (i) the formation of oversized atomic cages provided by the specific crystalline structure of pyrochlores; and (ii) the occupation of those oversized lattice voids by smaller guest ions.

(3) $La_2Zr_2O_7$ doped with smaller In^{3+}/Sc^{3+} guest ions expectedly exhibits an enhanced rattling effect and In/Sc-$La_2Zr_2O_7$ pyrochlores show a glass-like k at an amazingly low doping content ($x = 0.05$), which is much lower than that required to induce a glass-like k

for Y- $La_2Zr_2O_7$ pyrochlores (x = 0.20). However, the smaller rattlers with a stronger rattling effect still appear to be ineffective in reducing the high temperature plateau $k_{\min}$.

(4) The plateau $k_{\min}$ decreases steadily with an increase of oxygen vacancy concentration [V_O] in the lattice, whereas, $k_{\min}$ is almost identical at a give [V_O], with any structure details irrelevant. This suggests that oxygen vacancies are very powerful in reducing $k_{\min}$, because the electrostatic repulsive force of cations surrounding oxygen vacancies leads to stronger lattice anharmonicity as well as weaker atomic bonds.

(5) The effects of a normal substitutional defect on k have been studied by introducing a 96% heavier Hf^{4+} and a 21% larger Ce^{4+} to the B-sites of $La_2Zr_2O_7$ pyrochlore lattice. It is found that, the size difference, overtaken the mass variation of substitutional atoms, dominates the phonon scattering by point defects and therefore, controls the flatness of k-T curves.

(6) Besides oxygen vacancies, it is revealed for the first time that the plateau $k_{\min}$ can be effectively reduced by introducing substitutional atoms with a larger size, in addition to a heavier mass as suggested by Winter and Clarke [1]. This is attributed to that $k_{\min}$ is proportional to $\sqrt{E/a\overline{M}\gamma}$ and that a larger impurity ion produces a weaker ionic bond (i.e. lower E). In addition, interstitial atoms, similar as oxygen vacancies, can not only flatten k-T curves but also lower the high temperature plateau $k_{\min}$ as a result of the increased lattice anharmonicity as well as the reduced atomic bonds.

(7) To make a summary on the k reduction, the high temperature plateau $k_{\min}$ can be effectively reduced by introducing vacancies, interstitials and large and heavy ions to a

lattice, because the former two lattice imperfection forms (vacancies and interstitials) raise the lattice anharmonicity and soften the atomic bonds whist large and heavy ions tend to produce a large $\overline{M}$ and a weak atomic bond. By contrast, the strong phonon scatterers, such as vacancies, interstitials, rattlers, etc. can dramatically flatten k-T curves or even make k glass-like. They surely reduce k at the low and intermediate temperature but do not necessarily lower $k_{\min}$.

(8) The dispersion of 3 mol % Y_2O_3-tetragonal zirconia polycrystals (t-3YSZ) in the $La_2Zr_2O_7$ (LZ) matrix has increased the fracture toughness of LZ ceramics. The primary toughening mechanisms of the t-3YSZ/LZ ceramic composites made from the equilibrium route such as sintering are the phase transformations of the 3YSZ as the dispersive second phases as well as the generation of the residual compressive stress in the LZ matrix. The expected increase of K_{Ic} from both the residual compressive stress toughening and the ferroelastic toughening highlights the great potentials to improve the durability by depositing t'-3YSZ/LZ composite TBCs manufactured from the industrial non-equilibrium routes such as APS or EB-PVD.

7.2 Future work

(1) Measuring the grüneisen parameter of In/Sc-$La_2Zr_2O_7$ pyrochlores by the high-temperature Raman spectroscopy technique.

It is suggested that rattlers contribute to the anharmonic component of oscillation [2]. In this perspective, rattlers can raise the lattice anharmonicity, and therefore, can reduce the high-temperature plateau $k_{\min}$. However, the findings in Chapter 4 suggest rattlers are incompetent in reducing k_{min}. Therefore, it would be the direct evidence if the grüneisen parameter, a reflection of lattice anharmonicity, of In/Sc-$La_2Zr_2O_7$ pyrochlores can be measured. The high-temperature Raman spectroscopy makes this measurement feasible. The mode grüneisen parameter can be calculated by the following equation:

$$\gamma_i^P = \frac{1}{\beta\omega_i(0)}\left(\frac{\partial\omega_i}{\partial T}\right)_P \quad (7.1),$$

in which β is the volume thermal expansion coefficient; $\omega_i(0)$ is the frequency at 0 K of mode i; the subscript and superscript P denote all measurements conducting under constant pressure.

(2) Measuring the thermal expansion coefficient (TEC) of $La_2Zr_2O_7$ solid solutions doped with various guest ions.

In order to reduce the TEC misfit stress, TBC topcoat materials usually require a high TEC to match the underlying metallic layer. According to the Grüneisen law [3]:

$$\beta = \frac{\gamma C_V}{3KV_m} \quad (7.2),$$

where β is the volume thermal expansion coefficient; K is the isothermal bulk modulus; C_V is the isochoric specific heat per mole; V_m is the molar volume, a softened lattice (i.e. smaller K) usually gives an increased TEC. This suggests that Ce^{4+} doped $La_2Zr_2O_7$ solid solutions probably have a larger TEC than the undoped counterpart. A systematic study on the doping of A-sites or B-sites in $A_2B_2O_7$ pyrochlores is still required in order to better tailor the pyrochlore-based TBC topcoat materials.

(3) Employing the guideline proposed in this thesis to develop superiorly low-*k* materials, not only for TBC applications, but also for other applications such as thermoelectric materials.

To reduce the high temperature plateau $k_{\min}$, it is very effective to introduce as many as possible vacancies, interstitials, heavy and large ions to the lattice; whereas, to make *k* temperature-independent, it is suggested to introduce strong phonon scatterers, such as vacancies, interstitials, rattlers, or substitutional ions with a great size difference in comparison with the host ions. Depending on the specific temperature range in use, different strategies can be applied accordingly to reduce *k*.

(4) Introducing the $LaAlO_3$ ferroelastics as a second phase to toughen LZ ceramics

Like 3YSZ, $LaAlO_3$ is another ferroelastic material [4] and is thermochemically compatible with LZ ceramics. Therefore, it is another ideal second phase inclusion to toughen LZ ceramics. The fracture toughness of $LaAlO_3$ is about 3.2 $MPa \cdot m^{0.5}$ [5], which is very similar as that of 3YSZ [6]. However, the thermal conductivity of $LaAlO_3$ (about 12 W/m·K at 300 K) [7] is much higher than that of 3YSZ.

(5) Preparing TBCs of the compositions discussed in this thesis and studying their thermal and mechanical properties as well as their cyclic life and degradation mechanisms.

The thermal and mechanical properties discussed are based on the bulk samples. New issues will emerge when depositing those compositions as TBCs by the industrial routes such as APS or EB-PVD. Besides, the thermal and mechanical properties, the cyclic life and degradation mechanisms of TBCs require further investigation.

References

[1] M.R. Winter and D.R. Clarke. *Thermal conductivity of yttria-stabilized zirconia-hafnia solid solutions*. Acta Mater **54** (2006) 5051-5059.

[2] Z. Hiroi, J. Yamaura and K. Hattori. *Rattling good superconductor: β-pyrochlore Oxides AOs_2O_6*. J Phys Soc Jpn **81** (2012) 011012 1-24.

[3] D. T. Morelli, V. Jovovic and J. P. Heremans. *Intrinsically minimal thermal conductivity in cubic I-V-VI_2 semiconductors*. Phys Rev Lett **101** (2008) 035901 1-4.

[4] E.K.H. Salje. *Ferroelastic materials*. Annu Rev Mater Res **42** (2012) 265-283.

[5] X.Q. Liu and X.M. Chen. *Dielectric and mechanical characteristics of lanthanum aluminate ceramics with strontium niobate addition*. J Eur Ceram Soc **24** (2004) 1999-2004.

[6] A.G. Evans, D.R. Clarke and C.G. Levi. *The influence of oxides on the performance of advanced gas turbines*. J Eur Ceram Soc **28** (2008) 1405-1419.

[7] P.C. Michael, J.U. Trefny and B. Yarar. *Thermal transport-properties of single-crystal lanthanum aluminate*. J Appl Phys **72** (1992) 107-109.